Master Thesis in Geosciences

The Impact of Earthquakes on Tunnels in different Rock Mass Quality Q:

A numerical analysis

Tashi Tshering

UNIVERSITY OF OSLO

FACULTY OF MATHEMATICS AND NATURAL SCIENCES

The Impact of Earthquakes on Tunnels in different Rock Mass Quality Q:

A numerical analysis

Tashi Tshering

Master Thesis in Geosciences

Discipline: Geophysics

Department of Geosciences

Faculty of Mathematics and Natural Sciences

UNIVERSITY OF OSLO

1 June 2011

© Tashi Tshering, 2011

Tutor(s): Dr. Rajinder Bhasin (NGI) and Professor Valerie Maupin (UiO)

This work is published digitally through DUO – Digitale Utgivelser ved UiO

http://www.duo.uio.no

It is also catalogued in BIBSYS (http://www.bibsys.no/english)

All rights reserved. No part of this publication may be reproduced or transmitted, in any form or by any means, without permission.

Coverpage photo credit Wang et al. (2009) – Dankanliangzi tunnel during 2008 Wenchuan, China earthquake.

Summary

The impact of earthquakes, due to *ground shaking*, which affects the whole tunnel length from ovaling of the tunnel cross section, is investigated in this thesis. The influence of rock mass quality Q and the tunnel dimension is also studied. Finally, an approach to determine the new seismic support system using existing Q-system design chart and expected peak ground acceleration at the tunnel site is presented.

The earthquake loading is modeled through quasi-static seismic loading in Phase^2, a finite element modeling program by Rocscience, Inc. for design of underground structures and slopes. The quasi-static assumption is valid in rocks, as due to their higher velocity, the wavelength of shear waves is $> 20D$, where D is tunnel diameter. At this scale, the dynamic interaction between the tunnel and the passing seismic waves is minimal and thus validates the quasi-static assumption. The seismic coefficient, a unitless vector dependent on the peak ground acceleration (PGA), serves as a representative parameter for the expected critical earthquake.

Four rock mass classes with Q = 1 - 40, to represent "very poor" to "very good" rock masses are modeled by varying the deformation modulus and Mohr-Coulomb parameters, determined from empirical relations. The increase in support pressure (represented by *axial force*) is investigated as function of rock mass quality Q and tunnel dimension.

A model comprising of a 10 m diameter tunnel at 60 m depth surrounded by rock masses with Q ranging from 1 - 40 is used to investigate the influence of rock mass quality Q. While the seismic loading is unchanged, the magnitude of the axial force on the lining and the net increase due to seismic loading, referred to as *seismic axial force*, increases as the rock mass quality decreases.

To check the influence of tunnel diameter, the diameter of a circular tunnel at 60 m depth and under fixed seismic loading is increased from 5 m to 20 m at 5 m interval. The magnitude of the axial force and the seismic axial force increases with tunnel diameter for rock mass with Q = 1 ("very poor" rock mass). Conversely, the increase in magnitude of axial force and *seismic axial force* on the lining is relatively insignificant for rock mass with Q = 40 ("very good" rock mass).

Inferred from the above findings, an approach to determine the *seismic* support pressure by using the concept of $Q_{seismic}$, first introduced by Barton (1984), is presented. During earthquakes, the required support pressure is expected to increase due to additional seismic load. However, this increase in support pressure can be visualized as a decrease in rock mass quality Q around the tunnel and thus a new Q for seismic condition, called $Q_{seismic} = \alpha_k Q_{static}$, can be employed. The constant α_k mainly depends on the seismic coefficient used to represent the PGA or intensity of the expected critical earthquake, and rock mass quality. The relationship

$$\alpha_k = e^{-\beta K_h}$$

was determined for a 10 m diameter tunnel at 60 m depth for different rock masses. K_h is the horizontal seismic coefficient and the constant β depends on the rock mass quality, i.e. 4.3 for Q = 1, 3.1 for Q = 4 - 40, and 2.5 for elastic models. As K_h is increased from 0.05 to 0.70, α_k decreases from 0.81 to 0.06 for very poor rock masses with Q = 1.

The new *seismic* support system can be obtained using $Q_{seismic}$ from the existing Q-system tunnel design chart. As a general trend, the increases in support pressure correspond to *decrease* in bolt spacing and *increase* in the thickness of the fiber-reinforced shotcrete (Sfr). Unfortunately, the increase in thickness, which decreases the flexibility ratio, adversely affects the performance of the liner during earthquakes and therefore other measures to increase the support pressure are recommended. Nonetheless, this approach results in a refined rule-of-thumb that incorporates rock mass quality Q and seismic coefficient (= PGA) into the seismic design of tunnel support using Q-system.

Acknowledgements

This thesis is a fruit of contributions from many people who have shown to me the "light at the end of the tunnel" and then guided me toward it.

First of all, I am greatly indebted to Dr. Rajinder Bhasin, Norwegian Geotechnical Institute (NGI), for several reasons: (1) for arranging funds so that I can study at UiO, (2) for introducing to me this very interesting field of research, and (3) for guiding me throughout the thesis as my advisor. You have been both the "motor" and "lubricant" of this endeavor. Once again, thank you!

Then I would like to thank my academic advisor Professor Valerie Maupin, University of Oslo, for her help and guidance. I really enjoyed the topical discussions that we had throughout this thesis. You helped me understand the need for physical viability of anything – whether analytical or through numerical modeling.

My sincere thanks to Norwegian Geotechnical Institute (NGI) for providing office space and other necessary practical support, especially the Engineering Geology and Rock Engineering Division, with which I have had the privilege to interact. Also, I would like to thank Dr. Amir Kaynia, NGI, for his wonderful explanation about earthquake-tunnel interaction in rock masses and soils.

In addition, Mr. Pawel Jankowski, NGI, and Dr. F.N. Kong have always been very supportive since my first day in Oslo. Thank you Dr. Kong for the interesting discussions that we have had on EM and beyond. Thank you Pawel your continued assistance blended with high spirits, especially with field work here in Oslo.

I am also grateful to Dasho Sonam Yangley, Director General; Mr. Dorji Wangda, former Director General; Mr. Yeshi Dorji, former Specialist; and Mr. Ugyen Wangda, Head of Geology Division, from Department of Geology and Mines, Bhutan, for their continued support both in Bhutan and when I was away.

I also would like thank my family – Mom, Dad, and my siblings – and my in-laws for their support and prayers. I am grateful to my wife Sonam Choden and my son Tenzin Thinley for tolerating with my leave-of-absence from them for the past two years. Both of you have always been the source of inspiration for me to keep pushing higher.

The authors of programs and codes: *matrix2latex.m* (Moritz Koehler, 2009), *Roundoff.m* (Glen, 2009), *datalabel.m* (Mathworks, Inc., 2002 and Christophe COUVREUR, 1997), and *uiophd.cls* (Dag Langmyhr, 2008) are gratefully acknowledged. I am also grateful to Dr. Brent Corkum, Rocscience, Inc. for his prompt responses to my incessant emails about Phase^2.

Contents

List of Figures

List of Tables

Chapter 1

Introduction

1.1 Background

The use of underground space, in the form of caves, has been prevalent as early as the first civilization and it is becoming even more crucial at present due to the lack of space for new infrastructure at the surface. The typical underground structures include tunnels for water supply, hydro power, transportation, sewerage, and flood control and caverns for powerhouses, nuclear waste repositories, and storage of hydrocarbons. These phenomena necessitate more stringent design principles to increase the factor of safety, which includes designs considering soil-structure interaction (SSI) for both static and dynamic (seismic) loading.

Although it was a common notion among engineers that underground structures such as tunnels are invulnerable to earthquakes (Hashash et al., 2001), some underground structures, although affected less than surface structures, have undergone severe damages during recent large earthquakes such as 1995 Kobe, Japan; the 1999 Chi-Chi, Taiwan; the 1999 Kocaeli, Turkey; the 2004 Niigata, Japan , and the 2008 Wenchuan, China (Wang et al., 2001; Aydan et al., 2010; Li, 2011). Photos of damage to tunnels from 2004 Niigata and 2008 Wenchuan earthquakes are shown in Figs. 1.1 on the following page and 1.2 on the next page, respectively. During the 2004 Niigata earthquake, 49 out of 138 tunnels investigated suffered various degrees of damage (Jiang et al., 2010) and of the 18 tunnels investigated after the 2008 Wenchuan earthquake, 1 is classified as "slightly damaged", 4 as "moderately damaged" and 13 as "severely damaged" (Wang et al., 2009).

The common types of earthquake-induced damages include: (1) Slope failure at portals and ground failure induced tunnel failure, (2) Cracks on the lining – longitudinal, transverse, and inclined cracks, (3) Shear failure of lining due to fault displacement, (4) Pavement cracks, (5) Lining spalling, (6) Wall deformation, (7) Ground water rush and etc.

In the earlier days, for example before the 1971 San Fernando earthquake, the damage data was available only after strong earthquakes and therefore it was difficult to distinguish the cracks induced by the earthquake and those that existed before the earthquake. Nonetheless, the collection of data on damage induced by earthquakes on underground structures such as tunnels for transportation and hydropower increased after the 1971 San Fernando earthquake and several reports on the damage due to earthquakes have been published (Lanzano et al., 2008).

FIGURE 1.1: Fallen tunnel liner from crown due to ground shaking during 2004 Niigata, Japan earthquake. After FHWA (2009).

FIGURE 1.2: Tunnel collapse in weak carbonaceous mudstones during the 2008 Wenchuan earthquake. After Li (2011).

The most notable reports are: (1) American Society for Civil Engineers (ASCE) 1974 report on damages caused by the 1971 San Fernando earthquake to underground structures in Los Angeles area, (2) Dowding and Rozen (1978) with 71 cases, (3) Owen & Scholl (1981) with 127 cases, (4) Sharma and Judd (1991) with 191 cases, (5) Power et al. (1998) updated the previous reports with 192 cases from ten moderate to large earthquakes and by including only damages from ground shaking in bored or mined tunnels; damages attributed to ground failure due to landslides at portals or fault displacement were not included, and (6) Wang et al. (2001) on the damage encountered in mountain tunnels after the 1999 Chi-Chi, Taiwan earthquake. Among these, most of the documented damage cases are located in Japan, California (USA), China and Taiwan. Recently, Jiang et al. (2010) and Li (2011) analyzed the 2004 Niigata Japan and 2008 Wenchuan, China earthquakes, respectively.

As described in detail in the aforementioned reports, the following are the parameters that

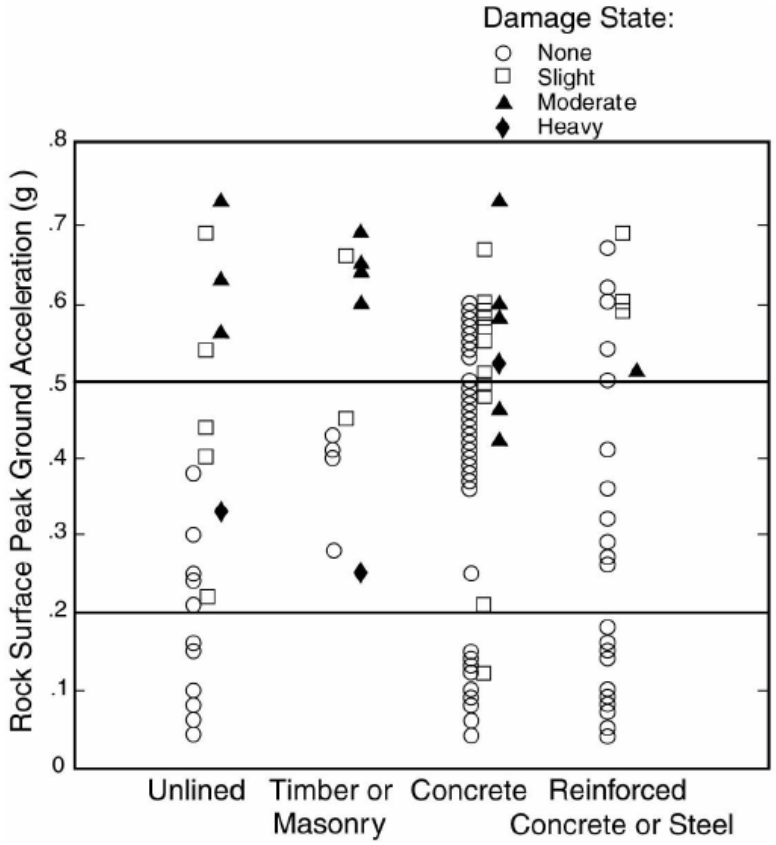

FIGURE 1.3: Summary of damage due to shaking for bored/mined tunnels with different support systems experiencing different PGA. After Power et al. (1998).

influence the damage to tunnels due to ground shaking:

1. *Magnitude of earthquake:* Sharma and Judd (1991) reported that severe damage occurred when the magnitude is > 6 on Richter scale.

2. *Distance to epicenter:* This is an important factor as the intensity of the earthquake at the tunnel site is determined by this distance. Sharma and Judd (1991) also reported severe damages when the epicentral distance is < 25 km. Jiang et al. (2010) and Li (2011) also noted the effect of the epicentral distance on the damage suffered by tunnels during earthquakes.

3. *Peak Ground Acceleration (PGA):* The Peak Ground Acceleration (PGA) at surface also affects the severity of the damage due to earthquakes. In fact, PGA represents the intensity of the earthquake felt at the site of interest and therefore incorporates both magnitude of the earthquake and epicentral distance, which were discussed above. Severe damages were reported when the PGA > 0.55g (Sharma and Judd, 1991) and > 0.5g (Dowding and Rozen, 1978). The g here stands for the acceleration due to gravity, which is roughly equal to 9.8 m/s. Both reports stated that the transition between *slight* and *moderate* damage occurs when PGA ≈ 0.2g. Thus, 0.2g appears to be the critical PGA at surface to undergoing moderate damage due to earthquakes. It may be noted that the PGA at depth,

where the tunnels are located, will be lower than at surface as the amplitude of the seismic waves will have decreased due exponential decay with depth of predominant Rayleigh waves and interference of incident and reflected waves below the surface (Barton, 1984). Power et al. (1998) updated the previous report by including only damages due to ground shaking in bored/mined tunnels and the summary is shown in Figure 1.3. Even after updates by Power et al. (1998), the critical PGA of 0.2g, below which only little damage was observed, remained unchanged.

4. *Geological conditions:* Li (2011) reported more severe damages during 2008 Wenchuan earthquake when the tunnel is located near the seismogenic fault. Jiang et al. (2010) used geological conditions –whether soft bedrock or hard bedrock – as one of the four parameters in their analysis using Hayashis quantification theory type II.

5. *Rock Mass Quality:* During the 2008 Wenchuan earthquake, slopes with poor rock mass quality failed and obstructed the tunnel portal. Even in the tunnel, seismic damages were mainly confined to zones with poor rock mass quality and abrupt lithological changes. Conversely, zones with homogeneous rock masses with high rock quality, for e.g. in granite, were only "slightly" to "moderately" damaged (Li, 2011).

6. *Overburden:* Li (2011) stated that during the 2008 Wenchuan earthquake, ring fracture zones or ring cracks were formed at the bedrock-overburden interface, which is due to contrast in seismic properties at this interface. Overburden thickness was also considered as one of the parameters in the analysis conducted by Jiang et al. (2010).

7. *Completion time (age of the tunnel):* Jiang et al. (2010) used construction year as one of the four parameters in the Hayashi's quantification theory type II analysis and this parameter is ranked second by contributing weight, behind distance to epicenter.

8. *Depth of the tunnel:* Sharma and Judd (1991) asserted from their case studies that severe damages were restricted to less than 50 m depth, with no serious damage below 300 m depth. Li (2011) noted during the 2008 Wenchuan earthquake that damage in hard rocks was slight to moderate for depth $>$ 50 m, with no damage $>$ 100 m depth. However, for weaker rocks, the transition depth to no-damage zone increases. In a weak zone in Longxi tunnel, the secondary concrete lining collapsed even at 500 m depth. This shows that the depth dependence gets complicated when rock mass quality is included into the analysis and it can be inferred that the depth at which the rock mass "yields", instead of the absolute depth, might be a better parameter to relate the impact on earthquakes.

9. *Angle between earthquake fault alignment and axis of the tunnel (angle of incidence?):* Jiang et al. (2010) reported the angle between the fault axis and the tunnel axes, related to angle of incidence of the seismic waves perturbing the tunnel, to be an important factor. Within the same distance to epicenter, the damage to tunnels are greater when the angle is $60° - 90°$. Li (2011) reported that when the general wave propagation direction was approximately parallel or oblique to the tunnel, mainly transverse and diagonal cracks were observed, indicating axial tension, axial compression, and local bending deformation.

10. *Influence of geo-stress:* The high in-situ geo-stress also results in greater damage during earthquakes. Li (2011) noted in damaged zones in Longxi tunnel, during the 2008 Wenchuan earthquake, evidences of fractures which bear characteristics of stress-release, including some bulges at the tunnel base and upheaval fractures in the invert. The in situ stress measurement after the earthquake confirmed that in-situ stress after the earthquake dropped by about 46% compared with pre-earthquake stress.

11. *Type of support:* Analysis by Sharma and Judd (1991) showed that a majority of damage occurred in "unlined" tunnels. Dowding (1979) also stressed the importance of lining details in assessing the potential earthquake damage on a tunnel.

12. *Use of the tunnel:* The use of the tunnel also determines the level of damage it can tolerate ("damage threshold") before being completely crippled. For instance, larger peak motions might be necessary to render a water tunnel functionless than it is for the road tunnel as a small rockfall could be washed away in a water tunnel. On the other hand, the same rock fall could severely disrupt the rail or road tunnel.

1.2 Objectives

Although underground structures such as tunnels are more resistant to earthquakes than surface structures, severe damages have been reported in recent major earthquakes. The main failure mechanism leading to the damages are: (1) ground failures such as landslides at portals, liquefaction and displacement of tunnels due to fault-slip, when the tunnel intercepts an active fault and (2) damage due to ground shaking resulting in lining cracks and spalling. It is apparent from previous studies that damages due to earthquakes are imminent when certain conditions, such as poor rock mass quality, shallow depth, high earthquake intensity, short epicentral distance, intercepting an active fault, among others, are unfortunately and unwittingly fulfilled.

From the two groups of damages, the first one due to ground failure, which is often site-specific, can be avoided (at least reduced or be prepared) if the siting of the underground facility is judiciously done (Dowding and Rozen, 1978). When it comes to the second type of damage due to ground shaking, this can be affected by earthquake from anywhere within the vicinity of the tunnel and is therefore difficult to predict with high confidence. Besides, this phenomenon, if happens, could affect the whole length of the tunnel and has higher probability of multiple occurrence (Dowding, 1979).

The main aim of this thesis is to conduct parametric numerical studies to analyze the impact of earthquakes on tunnel lining as a function of rock mass quality, tunnel dimension, and magnitude and direction of seismic loading using quasi-static approach. The effect of depth on the rock mass behavior is complicated in nature as with increasing depth more sophisticated phenomena such as *squeezing*[1] in weak rock masses or *rock bursts*[2] in good quality rock masses can also occur. Besides, since most of the earthquake damages occur at shallower depth, the depth of the tunnels in this study is fixed at 60 m. In addition, with lack of more reliable attenuation

[1] A type of high-stress ground condition in poor quality rocks. The rock mass squeezes plastically into the tunnel from both roof and the walls and the phenomenon is time-dependent (Singh and Goel, 2006).

[2] A violent failure in hard (brittle) and massive rock masses under high stress (Singh and Goel, 2006).

or reduction in ground motion model, it will not be possible to model the decrease in ground motion with depth. The modeling approach, without considering the decay in ground motion with depth, is unrealistic and it does not capture the physical phenomenon present as function of depth. Thus, the influence of depth is not considered in this thesis.

The eventual goal is to quantify additional support required to compensate for various seismic loading for different tunnel span and rock mass quality Q. For practical applications, a method to calculate the seismic rock mass quality $Q_{seismic}$ is presented. The $Q_{seismic}$ depends on the rock mass quality and seismic coefficient, which is related to the expected ground motion. For a particular rock mass quality, a range of $Q_{seismic}$ is expected depending on the range of the specified seismic coefficients. The new support system for seismic conditions can then be obtained from the usual Q-system tunnel design chart using the $Q_{seismic}$ instead of the usual Q.

1.3 Phase^2 from Rocscience, Inc.

The objectives presented in the previous section will be achieved through numerical analysis in Phase^2 7.0, a finite element modeling program by Rocscience, Inc. (http://www.rocscience.com). Phase^2 is a 2D finite-element stress analysis program that can be used for both underground and surface excavation rock or soil models. A range of applications are support design, finite element slope stability analysis, groundwater seepage (Rocscience, Inc., 2011).

Phase^2 assumes plane-strain assumption, where the out-of-plane displacement is taken as zero. This approach assumes that the excavations are of infinite length normal to the 2D plane under analysis. In plane strain analysis, the parameters calculated in Phase^2 are: (1) the major and minor in-plane stresses σ_1 and σ_3, respectively, (2) the out-of-plane principal stress σ_Z, and in-plane displacement and strains. In practice, however, as the out-of-plane excavation dimension becomes larger than five times the largest cross-sectional dimension, the stresses calculated using plane strain conditions show some exaggeration (Rocscience Inc., 2001). Such situations warrant the need for full 3D analysis instead of plane strain analysis.

Phase^2 consists of two modules – *Modeler* and *Interpret*. The model of a tunnel, or slope under investigation is constructed and "run" in the Modeler module. After computation of the model, the output is viewed and analyzed in the Interpret module. The procedures followed in Phase^2 to model the problem under study – a circular tunnel surrounded by different rock mass quality Q under both static and seismic conditions – are discussed in detail in Chapter 5.

1.4 Structure of the Thesis

The following is a brief outline of the thesis.

- **Chapter 2 - Static Design of Tunnels:** Before analyzing the impact of earthquakes on tunnels through seismic loading, it is imperative to understand the principle associated with designing tunnel support for static conditions. This chapter provides a glimpse of the state-of-the-art approaches, especially using rock mass classification in the view of the Norwegian Q-system.

- **Chapter 3 - Seismic Design of Tunnels:** After determining the static conditions as described in the previous chapter, seismic loading is applied to the tunnel to simulate an earthquake that occurs at a later stage. This chapter covers the philosophy and challenges associated with modeling earthquake loading on tunnels, especially in Phase^2.

- **Chapter 4 - Theoretical Background: Modeling Parameters:** This chapter consists of the procedures followed to select different geomechanical parameters – strength and deformation modulus – to model rock masses with different Q-values. In addition, the choice of different post-failure characteristics while assigning the properties of the materials used in the elastic-plastic models are also discussed.

- **Chapter 5 - Numerical Modeling in Phase^2:** After choosing the methodology for seismic loading and the properties of different rock masses, the steps followed in Phase^2 to capture the nature in which earthquake loading occurs are discussed in this chapter. The method to compute *seismic axial force*, a parameter used to compare different experiments, is also presented.

- **Chapter 6 - Results:** This chapter consists of two main parts: (1) the analysis of results using Bolu Tunnel in Turkey as a case study to compare different seismic loading approaches with actual observed damage and (2) the result of the experiments to investigate the influence of rock mass quality Q and tunnel dimension during earthquake loading.

- **Chapter 7 Seismic Rock Mass Quality $Q_{seismic}$:** The concept of $Q_{seismic}$, which is used to obtain the seismic support system, from existing Q-system design chart, is elaborated in this chapter. Methods to compute the $Q_{seismic}$ from Q_{static} for different earthquake scenarios, represented by expected peak ground acceleration, are also included.

- **Chapter 8 and 9 - Conclusions and Recommendations:** These two chapters include a synopsis of the findings from this study and recommendations for future research in this field.

Chapter 2

Static Design of Tunnels

There are three different approaches to tunnel design: the Rational, Observational, and Empirical. All three approaches have their own advantages and limitations and thus are not considered as alternatives, but rather as being complementary to one another as each approach adds useful information to the design (Oreste, 2009).

The rational approach uses analytical solutions, when available, and numerical studies to predict the state of the stress and interaction between the rock mass and the support system. The Convergence Confinement Method (CCM), which is described in Carranza-Torres and Fairhurst (2000) and AFTES (2001), is one rational approach that uses analytical solutions. Three plots, namely Longitudinal Deformation Profile (LDP), Ground Response Curve (GRC), and Support Characteristic Curve (SCC) are the main components of this method. A schematic diagram, describing this method using the LDP, GRC, and SCC plots, is shown in Figure 2.1.

The Longitudinal Deformation Profile (LDP) is the plot that shows the wall convergence of the tunnel vs. the distance from the tunnel face. This accounts for the 3D nature of the tunnel excavation, where as the support offered by the unexcavated rock face decreases as the rock face moves away due to the advancement of excavation. Thus, as the distance from the tunnel face increases, the wall convergence u_r also increases until it stabilizes at an equilibrium point (see top figure in Fig. 2.1 on the following page). After knowing the distance L at which the support is installed, the initial convergence u_r^0 that has occurred before installation of the support can be determined.

The Ground Response Curve (GRC), which is a plot of the internal stress of a circular tunnel vs. radial convergence, describes the characteristics of the rock mass in which the tunnel is excavated. The reduction in internal stress in this plot is mainly due to the reduction in the support from the unexcavated tunnel face, which moves away from the point of interest as the excavation advances.

The Support Characteristic Curve (SCC), which is the plot of support pressure or the pressure borne by the support vs. the resulting convergence, indicates the nature and behavior of the installed support system. When the GRC and SCC are overlain (see bottom figure in Fig. 2.1 on the next page), their intersection point denotes the equilibrium point and its coordinates show the support pressure P_s^D and the expected convergence u_r^D for that rock mass-support system. The SCC starts at u_r^0 (determined from LDP) along the convergence axis. Thus, this method determines the *design* support pressure on the support system and the maximum displacement

experienced, using which the factor of safety and viability of the installed support system can be determined. The main limitation of this method is that the analytical solutions assume circular tunnel cross-section under uniform or hydrostatic stress (Carranza-Torres and Fairhurst, 2000).

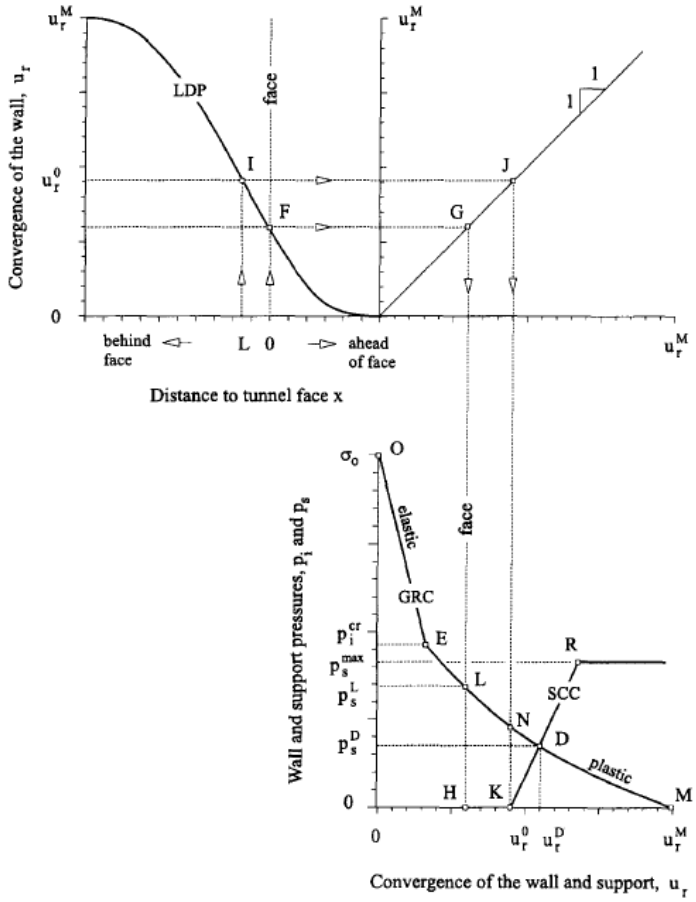

FIGURE 2.1: Schematic representation of Longitudinal Deformation Profile (LDP), Ground Reaction Curve (GRC), and Support Characteristic Curve (SCC). After Carranza-Torres and Fairhurst (2000).

The observational approach uses monitoring of deformation and stresses during the construction as its integral part and the rock support requirement is modified, based on interpretation of the monitoring data, as the construction of the tunnel proceeds. This is the basis of the New Austrian Tunneling Method, commonly known as NATM. In addition, the use of mathematical back-analysis techniques using the monitoring data to obtain other rock mass parameters, such as deformation modulus, has increased the use and organization of measurement data obtained from this method (Oreste, 2009).

The empirical approach utilizes previous case studies and experiences to determine a set of support design recommendations and is often in terms of rock mass classification parameters such as Rock Mass Rating (RMR) by Bieniawski (1974), NGI Q-system (Barton et al., 1974; Grimstad et al., 2003), Geological Strength Index (GSI) by Hoek and Marinos (2007), and Rock Mass Index (RMi) by Palmstrom (1995).

All of these classification schemes involve collection of various geological and geotechnical data in field during preliminary studies, or in tunnels during construction, which are then combined to obtain a rock mass classification rating. Then, the support recommendations are achieved using this final rating and design charts or schemes, which were created using past

experiences and case studies. Since this study is geared toward studying the impact of earthquakes on tunnel lining as for different rock mass quality in terms of Q, the NGI Q system will be discussed in detail in the next section.

2.1 The NGI Q-system

The Q-system is a system for classification of rock masses in the view of designing *preliminary* support system for stability of underground structures such as tunnels and caverns. This system was first introduced in 1974 (Barton et al., 1974), but it was updated later – the latest being Grimstad et al. (2003), which is based on *1260* case records. The Q value is calculated using the six parameters as shown in Equation 2.1.

$$Q = \frac{RQD}{J_n} \times \frac{J_r}{J_a} \times \frac{J_w}{SRF} \tag{2.1}$$

The six parameters are as follows:

RQD	=	Rock Quality Designation
J_n	=	Number of joint sets
J_r	=	Joint roughness number
J_a	=	Joint alteration number
J_w	=	Joint water reduction factor
SRF	=	Stress Reduction Factor

These parameters will be described in detail later in this section, but it is noteworthy that when these six parameters are combined as pairs, the following quotients bear other physical meanings which are relevant to the stability of underground excavations. The information on NGI Q-system presented in this section are adapted from NGI (1997).

$\frac{RQD}{J_n}$	=	Degree of jointing or block size
$\frac{J_r}{J_a}$	=	Joint friction or inter-block shear strength
$\frac{J_w}{SRF}$	=	Active stress component

2.1.1 RQD (Rock Quality Designation)

First defined by Deere in 1963, the RQD was intended for simple classification system for rock masses and five rock classes defined from A to E (see Table 2.1). Originally, the RQD is the sum of the length (between natural joints) of all core pieces more than 10 cm long as percentage of the total core length. The size of the core should be at least NX (54.7 mm) and should be drilled with a double tube core barrel (Palmstrom, 2005). A schematic diagram depicting the measurement of RQD is shown in Figure 2.2.

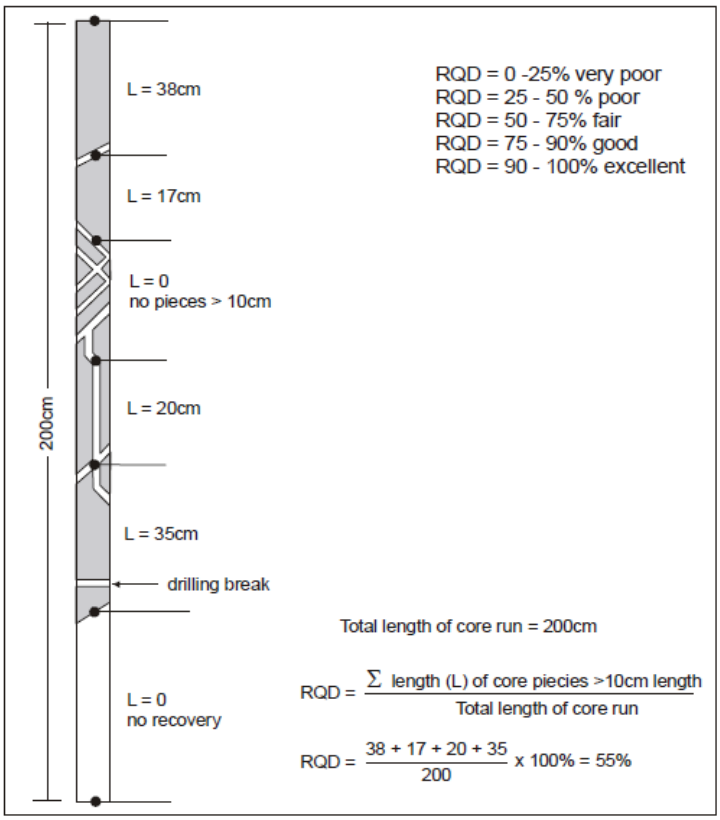

FIGURE 2.2: Procedure to measure RQD. After Palmstrom (2005).

Thus, the RQD will be a number between 0 and 100. While using the Q-system in tunnels, however, all types of fractures must be considered in the calculation of RQD and when the measured RQD $\leq$ 10 (including 0), a nominal value of 10 is used to calculate Q. When drill cores are not present, RQD can be calculated from number of joints per m^3, or joint volume J_v as per the Equation 2.2 from Palmstrom (1975). The range of RQD values assigned for computation of the Q value are shown in Table 2.1.

Rock quality designation		RQD (%)
A	Very poor	0–25
B	Poor	25–50
C	Fair	50–75
D	Good	75–90
E	Excellent	90–100

Notes: (i) Where RQD is reported or measured as $\leqslant$10 (including 0), a nominal value of 10 is used to evaluate Q. (ii) RQD intervals of 5, i.e., 100, 95, 90, etc., are sufficiently accurate.

TABLE 2.1: Range of RQD values and their descriptions. After Barton (2002).

$$RQD = 115 - 3.3J_v \tag{2.2}$$

2.1.2 Joint Set Number J_n

The joint set number, when combined with RQD, determines the block size or degree of jointing. In a particular location, sets of joints will be systematically orientated in particular direction

and most of the joints will be parallel to these main directions. Such parallel joints are called joint sets. The values of J_n for different number of joint sets are shown in Table 2.2. In general, the greater the number of joint sets, the smaller the block size becomes, and therefore generates a lower Q-value. Thus, J_n has an inverse relationship with Q and, therefore, appear in the denominator of Equation 2.1.

Joint set number		J_n
A	Massive, no or few joints	0.5–1
B	One joint set	2
C	One joint set plus random joints	3
D	Two joint sets	4
E	Two joint sets plus random joints	6
F	Three joint sets	9
G	Three joint sets plus random joints	12
H	Four or more joint sets, random, heavily jointed, 'sugar-cube', etc.	15
J	Crushed rock, earthlike	20

Notes: (i) For tunnel intersections, use $(3.0 \times J_n)$. (ii) For portals use $(2.0 \times J_n)$.

TABLE 2.2: Range of J_n values and their descriptions. After Barton (2002).

2.1.3 Joint Roughness Number J_r

The nature of the rock joints, if they are undulating, planar, rough or smooth, affects the joint friction or the inter-block shear strength. The higher the J_r, higher the joint friction, and therefore higher the Q value. It was also asserted in Barton (2002) that the ratio $\frac{J_r}{J_a}$ "closely resembles the dilatant or contractile coefficient of joints or filled discontinuities". The range of J_r values and their geotechnical and geological descriptions are shown in Table 2.3.

Joint roughness number		J_r
(a) *Rock-wall contact, and (b) rock-wall contact before 10 cm sear*		
A	Discontinuous joints	4
B	Rough or irregular, undulating	3
C	Smooth, undulating	2
D	Slickensided, undulating	1.5
E	Rough or irregular, planar	1.5
F	Smooth, planar	1.0
G	Slickensided, planar	0.5
(b) *No rock-wall contact when sheared*		
H	Zone containing clay minerals thick enough to prevent rock-wall contact.	1.0
J	Sandy, gravely or crushed zone thick enough to prevent rock-wall contact	1.0

Notes: (i) Descriptions refer to small-scale features and intermediate scale features, in that order. (ii) Add 1.0 if the mean spacing of the relevant joint set is greater than 3 m. (iii) $J_r = 0.5$ can be used for planar, slickensided joints having lineations, provided the lineations are oriented for minimum strength. (iv) J_r and J_a classification is applied to the joint set or discontinuity that is least favourable for stability both from the point of view of orientation and shear resistance, τ(where $\tau \approx \sigma_n \tan^{-1}(J_r/J_a)$.

TABLE 2.3: Range of J_r values and their descriptions. After Barton (2002).

2.1.4 Joint Alteration Number J_a

As described above, J_a, when combined with J_r, influences the frictional strength of the joints. The thickness and mineral composition of the infill within the joints determine the J_a. The values of J_a for different types of infills and joint thicknesses are shown in Table 2.4. The rock mass quality Q bears an inverse relationship with J_a. As a general trend, rock walls that remain in contact when sheared (i.e. thin infills) have lower J_a than rock walls with large spacing. Similarly, joints that are filled with clay minerals have higher J_a than those filled with hard materials like quartz and epidote.

Joint alteration number		ϕ_r approx. (deg)	J_a
(a) *Rock-wall contact (no mineral fillings, only coatings)*			
A	Tightly healed, hard, non-softening, impermeable filling, i.e., quartz or epidote	—	0.75
B	Unaltered joint walls, surface staining only	25–35	1.0
C	Slightly altered joint walls, non-softening mineral coatings, sandy particles, clay-free disintegrated rock, etc.	25–30	2.0
D	Silty- or sandy-clay coatings, small clay fraction (non-softening)	20–25	3.0
E	Softening or low friction clay mineral coatings, i.e., kaolinite or mica. Also chlorite, talc, gypsum, graphite, etc., and small quantities of swelling clays	8–16	4.0
(b) *Rock-wall contact before 10 cm shear (thin mineral fillings)*			
F	Sandy particles, clay-free disintegrated rock, etc.	25–30	4.0
G	Strongly over-consolidated non-softening clay mineral fillings (continuous, but <5 mm thickness)	16–24	6.0
H	Medium or low over-consolidation, softening, clay mineral fillings (continuous, but <5 mm thickness)	12–16	8.0
J	Swelling-clay fillings, i.e., montmorillonite (continuous, but <5 mm thickness). Value of J_a depends on per cent of swelling clay-size particles, and access to water, etc.	6–12	8–12
(c) *No rock-wall contact when sheared (thick mineral fillings)*			
KLM	Zones or bands of disintegrated or crushed rock and clay (see G, H, J for description of clay condition)	6–24	6, 8, or 8–12
N	Zones or bands of silty- or sandy-clay, small clay fraction (non-softening)	—	5.0
OPR	Thick, continuous zones or bands of clay (see G, H, J for description of clay condition)	6–24	10, 13, or 13–20

TABLE 2.4: Range of J_a values and their descriptions. After Barton (2002).

2.1.5 Joint Reduction Water Factor J_w

The joint water affects the rock mass quality in at least two ways: (1) water softens the mineral infill and may eventually be washed away, thereby reducing the joint friction and (2) water pressure reduces the normal force on the joint walls, thereby facilitating the shearing of the joint walls. Thus, J_w, which is determined from the leakage of water into the underground cavity, bears a direct proportionality to the rock mass quality Q. The values of J_w for different water-related situations in the underground cavity are shown in Table 2.5.

2.1.6 Stress Reduction Factor SRF

The stress factor SRF accounts for the relation between stress and rock strength around the underground cavity. Since both stress and strength can be calculated, the SRF can then be acquired, using Table 2.6, from the ratios $\frac{\sigma_c}{\sigma_1}$ or $\frac{\sigma_\theta}{\sigma_c}$. σ_c is the uniaxial strength of the rock, σ_1 is the major principal stress, and σ_θ is the major tangential stress.

	Joint water reduction factor	Approx. water pres. (kg/cm^2)	J_w
A	Dry excavations or minor inflow, i.e., <5 l/min locally	<1	1.0
B	Medium inflow or pressure, occasional outwash of joint fillings	1–2.5	0.66
C	Large inflow or high pressure in competent rock with unfilled joints	2.5–10	0.5
D	Large inflow or high pressure, considerable outwash of joint fillings	2.5–10	0.33
E	Exceptionally high inflow or water pressure at blasting, decaying with time	>10	0.2–0.1
F	Exceptionally high inflow or water pressure continuing without noticeable decay	>10	0.1–0.05

Notes: (i) Factors C to F are crude estimates. Increase J_w if drainage measures are installed. (ii) Special problems caused by ice formation are not considered. (iii) For general characterisation of rock masses distant from excavation influences, the use of $J_w = 1.0, 0.66, 0.5, 0.33$, etc. as depth increases from say 0–5, 5–25, 25–250 to >250 m is recommended, assuming that RQD/J_n is low enough (e.g. 0.5–25) for good hydraulic connectivity. This will help to adjust Q for some of the effective stress and water softening effects, in combination with appropriate characterisation values of SRF. Correlations with depth-dependent static deformation modulus and seismic velocity will then follow the practice used when these were developed.

TABLE 2.5: Range of J_w values and their descriptions. After Barton (2002).

	Stress reduction factor	SRF		
	(a) *Weakness zones intersecting excavation, which may cause loosening of rock mass when tunnel is excavated*			
A	Multiple occurrences of weakness zones containing clay or chemically disintegrated rock, very loose surrounding rock (any depth)	10		
B	Single weakness zones containing clay or chemically disintegrated rock (depth of excavation ⩽50 m)	5		
C	Single weakness zones containing clay or chemically disintegrated rock (depth of excavation >50 m)	2.5		
D	Multiple shear zones in competent rock (clay-free), loose surrounding rock (any depth)	7.5		
E	Single shear zones in competent rock (clay-free), (depth of excavation ⩽50 m)	5.0		
F	Single shear zones in competent rock (clay-free), (depth of excavation >50 m)	2.5		
G	Loose, open joints, heavily jointed or 'sugar cube', etc. (any depth)	5.0		
		σ_c/σ_1	σ_θ/σ_c	SRF
	(b) *Competent rock, rock stress problems*			
H	Low stress, near surface, open joints	> 200	<0.01	2.5
J	Medium stress, favourable stress condition	200–10	0.01–0.3	1
K	High stress, very tight structure. Usually favourable to stability, may be unfavourable for wall stability	10–5	0.3–0.4	0.5–2
L	Moderate slabbing after >1 h in massive rock	5–3	0.5–0.65	5–50
M	Slabbing and rock burst after a few minutes in massive rock	3–2	0.65–1	50–200
N	Heavy rock burst (strain-burst) and immediate dynamic deformations in massive rock	<2	>1	200–400
		σ_θ/σ_c	SRF	
	(c) *Squeezing rock: plastic flow of incompetent rock under the influence of high rock pressure*			
O	Mild squeezing rock pressure	1–5	5–10	
P	Heavy squeezing rock pressure	>5	10–20	
		SRF		
	(d) *Swelling rock: chemical swelling activity depending on presence of water*			
R	Mild swelling rock pressure	5–10		
S	Heavy swelling rock pressure	10–15		

Notes: (i) Reduce these values of SRF by 25–50% if the relevant shear zones only influence but do not intersect the excavation. This will also be relevant for characterisation. (ii) For strongly anisotropic virgin stress field (if measured): When $5 \leqslant \sigma_1/\sigma_3 \leqslant 10$, reduce σ_c to $0.75\sigma_c$. When $\sigma_1/\sigma_3 > 10$, reduce σ_c to $0.5\sigma_c$, where σ_c is the unconfined compression strength, σ_1 and σ_3 are the major and minor principal stresses, and σ_θ the maximum tangential stress (estimated from elastic theory). (iii) Few case records available where depth of crown below surface is less than span width, suggest an SRF increase from 2.5 to 5 for such cases (see H). (iv) Cases L, M, and N are usually most relevant for support design of deep tunnel excavations in hard massive rock masses, with RQD/J_n ratios from about 50–200. (v) For general characterisation of rock masses distant from excavation influences, the use of SRF = 5, 2.5, 1.0, and 0.5 is recommended as depth increases from say 0–5, 5–25, 25–250 to >250 m. This will help to adjust Q for some of the effective stress effects, in combination with appropriate characterisation values of J_w. Correlations with depth-dependent static deformation modulus and seismic velocity will then follow the practice used when these were developed. (vi) Cases of squeezing rock may occur for depth $H > 350Q^{1/3}$ according to Singh [34]. Rock mass compression strength can be estimated from $\mathrm{SIGMA_{cm}} \approx 5\gamma Q_c^{1/3}$ (MPa) where γ is the rock density in t/m^3, and $Q_c = Q \times \sigma_c/100$, Barton [29].

TABLE 2.6: Range of SRF values and their descriptions. After Barton (2002).

Once the above six parameters are determined, they are combined together using Equation 2.1 on page 11 to obtain a Q-value that represents the rock mass quality of the "zone under

study" along the tunnel, or at an outcrop. As there are always uncertainties associated to choosing a value for any parameter, a range of Q values can be calculated from a range of parameters, instead of restraining to a single value.

For a particular Q value, based on dimension of the tunnel and the Excavation Support Ratio (ESR), the recommended support and reinforcement can be determined from the chart shown in Figure 2.3 on the next page. The recommended support will, for most cases, be rock bolts with specified length and spacing, and fiber-reinforced shotcrete (Sfr) or plain shotcrete (S) with specified thickness. For good quality rock masses, the rock bolts alone will suffice to stabilize the excavation, whereas for very poor quality rock reinforced ribs of concrete (RRS) or cast concrete lining (CCA) is recommended. The ESR is a parameter that depends on the type and purpose of the excavation as shown in Table 2.7.

	Type of Excavation	**ESR**
A	Temporary mine openings, etc	ca. 3-5
B	Vertical shafts: i. circular sections Vertical shafts: ii. Rectangular/square section	ca. 2.5 ca. 2.0
C	Permanent mine openings, water tunnels for hydropower (excluding penstocks), pilot tunnels, drifts and headings for large openings	1.6
D	Storage rooms, water treatment plants, minor road and railway tunnels, surge chambers, access tunnels, etc.	1.3
E	Power stations, major road and railway tunnels, civil defense chambers, portals, intersections, etc.	1.0
F	Underground nuclear power stations, railways stations, sports and public facilities, factories, etc.	0.8
G	Very important caverns and tunnels with long lifetime, tunnels for gas pipe lines	0.5

TABLE 2.7: ESR for different facilities. After NGI (1997)

2.1.7 Support Pressure

For an excavation, the support pressure exerted on the installed support by the surrounding rock mass can be expressed in terms of the rock mass quality Q. An empirical equation showing the relationship, obtained by fitting the data from original case records, between the support pressure and rock mass quality Q (Barton et al., 1974) is as follows:

$$P_{roof}(kPa) = \frac{200}{J_r}\, Q^{-1/3} \tag{2.3}$$

where P_{roof} is the support pressure and J_r is the joint roughness number.

It may be noted here that the support pressure is independent of the tunnel dimension. However, Barton et al. (1974) stated that when the excavation dimension in a particular rock mass quality is increased, as per the Q-system chart shown in Fig. 2.3 on the next page, the thickness of the shotcrete and the bolt length must be increased; the bolt spacing, however, remains the same. Thus, the *load capacity* of the support system is increased although the support pressure remains unchanged.

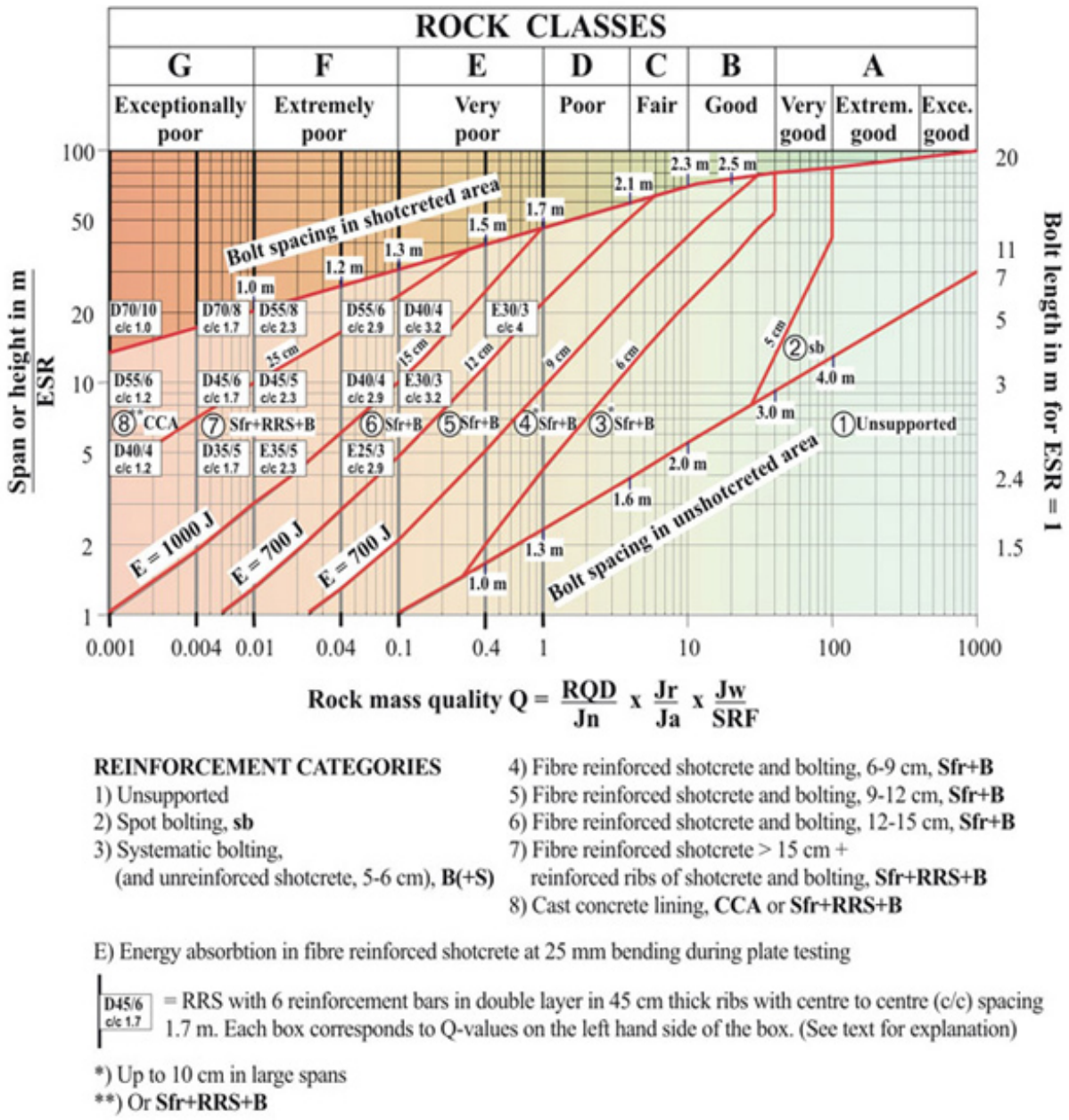

FIGURE 2.3: Support chart for Norwegian Q-system (Grimstad et al., 2003)

By considering the effect of the dimension of the tunnel D, for poor quality rock masses, Bhasin and Grimstad (1996) proposed a modified version of Equation 2.3 on the facing page as shown below:

$$P_{roof}(kPa) = \frac{40D}{J_r} Q^{-1/3} \tag{2.4}$$

The underlying rationale behind the application of the six parameter Q-value in tunnel design is the selection of a "suitable combination of shotcrete and rock bolts for rock mass reinforcement and support". The support of the rock mass externally using shotcrete and internal reinforcement of the rock mass using rock bolts strengthen the overall rock mass around the tunnel to overcome both immediate and future failures. This tunnel design approach, al-

though empirically derived, was later substantiated when it was realized (Barton, 2002) that the $Q_c = Q \times \frac{\sigma_c}{100}$ is the product of a cohesive component "CC" and a frictional component "FC". Thus, the application of Q-value to determine the support and reinforcement of the rock mass is founded on the principle that aims to compensate for low cohesive and low frictional strength of the rock mass around the tunnel as it is stated in Barton (2004):

> "Shotcrete, in different thicknesses, is broadly speaking a practical surface 'fix' for lack of cohesive strength, while rock bolts, with different spacings, are compensating for lack of (internal) frictional strength."

The frictional and the cohesive components can be defined as follows:

$$CC = \frac{RQD}{J_r} \times \frac{1}{SRF} \times \frac{\sigma_c}{100} \tag{2.5}$$

$$FC = tan^{-1}(\frac{J_r}{J_a} \times J_w) \tag{2.6}$$

Chapter 3

Seismic Design of Tunnels

The damage mechanism of a tunnel during earthquakes can be classified into two groups: (1) ground failure such as landslides at portals, liquefaction, and fault slip at the intersection with faults, and (2) damage from ground shaking (Dowding and Rozen, 1978; Sharma and Judd, 1991; Power et al., 1998; Hashash et al., 2001); the earlier studies, such as Dowding and Rozen (1978) and Sharma and Judd (1991), classified the first group stated here into two subgroups as ground failure and displacement due to fault slip.

Landslides and liquefaction[1] triggered by ground motion occur near the portal or at shallow depth and thus may be treated as surface or surface-related structures rather than underground structures. Damage due to displacement related to fault slip happens when the underground structure intersects a fault line that is displaced during an earthquake; appropriate siting during planning could avoid this problem (Dowding and Rozen, 1978).

As expected, displacement due to fault slip and its damages on tunnels cannot be prevented. If a tunnel crosses a potentially active fault, special design should be implemented where either the underground structure should be designed to withstand displacement without major damage or proper post-earthquake repair strategies should be planned in advance and it is "impractical to design a tunnel to withstand a potential offset of an active fault" (St John and Zahrah, 1987). However, these two damage mechanisms – ground failure at portals and displacement due to fault-slip, which require site-specific studies, are not included under the purview of this thesis.

The failure mechanism addressed in this study is the damage from ground shaking that is caused by the interaction of the tunnel with the propagating elastic waves that has emanated from the *hypocenter* of the earthquake. This is because the damage from ground shaking is site-independent and can be caused by an earthquake anywhere as long as the intensity of the shaking at the tunnel is above the damage-threshold. This damage due to ground shaking also has higher probability of multiple occurrence. On the other hand, the other ground-failure related damage – due to landslides, liquefaction, and fault displacement, are site-specific and the potential damage could be minimized if favorable sites are selected during site assessment of the tunnel (Dowding and Rozen, 1978; Dowding, 1979).

Although the ground failure-related mechanisms dominate the damage of tunnels during

[1] Soil liquefaction is a phenomenon where a saturated soil substantially loses strength and stiffness in response to an applied stress, usually earthquake shaking or other sudden change in stress condition, causing it to behave like a liquid (`http://en.wikipedia.org/wiki/Soil_liquefaction`. Accessed 30 May 2011.).

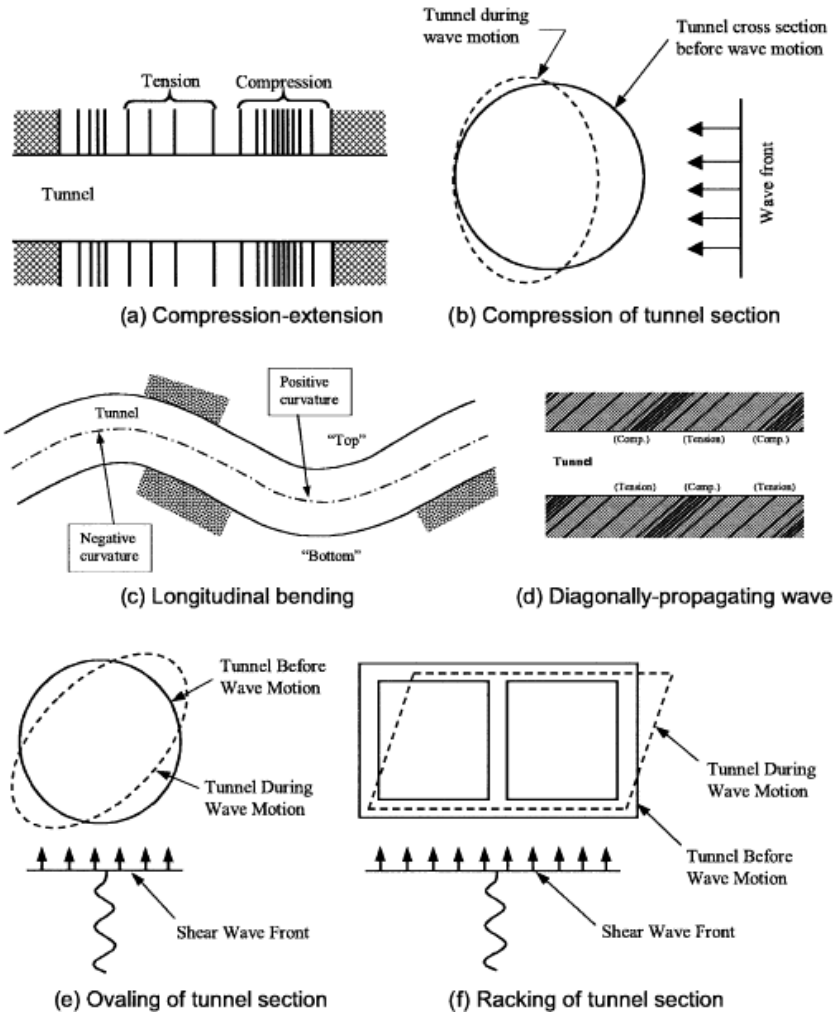

FIGURE 3.1: Deformation modes of tunnels due to seismic waves. After Owen and Scholl, 1981 cited in Hashash et al. (2001)

earthquakes, damage due to ground shaking has also been recorded; this mechanism, if prevalent, could affect the whole length of the tunnel. Some of the recent damages to tunnels attributed to the ground shaking effect during earthquakes include the damage and near-collapse at the Daikai and Nagata subway stations (Kobe Rapid Transit Railway) during the 1995 Kobe Earthquake in Japan (FHWA, 2009) and damage to tunnels during the 2008 Wenchuan, China earthquake (Li, 2011).

The design of earthquake resistant underground structures requires an understanding about the manner in which the propagating seismic waves, such as generated by earthquakes, interact with an underground structure such as tunnels in this case. Owing to their distinct features, namely (1) their complete closure in soil and (2) their significant length (Hashash et al., 2001), the behavior of tunnels under seismic loading is different from that of the surface structures. For most underground structures, the inertia of the surrounding rock is large relative to the inertia of the structure and therefore the seismic response of the tunnel is dominated by the response of the surrounding soil or rock mass. On the contrary, the seismic response of a surface structure is dominated by its inertial effects (Hashash et al., 2001).

When seismic waves, either body waves or surface waves, perturb a tunnel in the subsurface,

depending on the mode of particle motions caused by the passing waves, a tunnel can undergo three types of deformations (Hashash et al., 2001): (1) axial compression and extension, (2) longitudinal bending and (3) ovaling/racking (see Fig. 3.1). The axial deformation is produced by seismic waves that have particle motion parallel to the axis of the tunnel. Longitudinal bending can be attributed to components of seismic waves producing particle motions perpendicular to the longitudinal axis. Ovaling of circular tunnels and racking of rectangular openings, which results in distortion of the cross-section of the tunnel, are caused by shear waves propagating perpendicular to the tunnel axis (Hashash et al., 2001).

It is clear that a 3D model is required to analyze the mechanism of tunnel deformation due to all three modes described above (Kontoe et al., 2008). Thus, using 2D plane-strain method in Phase^2, the ovaling phenomenon in the transverse plane of the tunnel, which is exhibited by the tunnel under seismic loading when the particle motions due to passing seismic waves are perpendicular to the tunnel axis, is studied in this thesis. Among the three types of deformations, the ovaling of tunnel cross-sections caused by shear waves propagating normal to the tunnel axis is the most critical deformation when it comes to the impact of earthquakes on tunnels (Kontoe et al., 2008).

The main factors influencing the impact of earthquakes on tunnels are: (1) seismic hazard such as expected peak ground acceleration or intensity, (2) geologic conditions, and (3) tunnel design, construction, and condition (FHWA, 2009), as already discussed in Chapter 1.

Among other factors, the expected seismic motion component, which is one of the crucial factors to determining the effect of earthquakes on tunnels, will be discussed in the following sections. In addition to having the knowledge of the rock mass quality surrounding the tunnel, the principle of design of earthquake resistant underground structures should be founded on the understanding of the anticipated level of ground shaking during earthquakes and the tunnel response to earthquakes including rock mass-structure interaction. These can be achieved in the following steps:

- Seismic Hazard Analysis, where a *design* ground motion parameter representing the anticipated earthquake is obtained.
- Underground structure response to earthquakes, which determines the response of the underground structure to traveling seismic waves. Several design approaches exist on how a tunnel buried in the rock or soil interacts with the seismic waves.

3.1 Seismic Hazard Analysis

The principal step in the design of earthquake resistant underground structures is obtaining the level of ground motion of an anticipated earthquake that the underground structure must withstand without exceeding a pre-defined acceptable level (Hashash et al., 2001). Seismic hazard analysis is undertaken to know the expected level of ground motion at a study area. There are two methods of analysis: (1) the deterministic seismic hazard analysis (DHSA) and (2) the probabilistic seismic hazard analysis (PSHA).

The deterministic seismic hazard analysis identifies one or more earthquake motions for a site and the design of underground structures considers that the structure will be able to withstand this *design* earthquake. This is achieved following the steps shown in Fig. 3.2, where

from among several earthquake scenarios, a controlling earthquake is identified as the *design* earthquake. First the most likely seismic sources are identified followed by evaluation of the source to site distances. Then the motion parameter from all the identified sources are calculated and the controlling earthquake is then identified. Although a straightforward step for evaluation of the worse-case scenarios at a site, this method provides no information on the likelihood or frequency of occurrence of the identified design earthquake (Hashash et al., 2001).

The probabilistic seismic hazard analysis, on the other hand, incorporates the uncertainties associated with the size, location, and recurrence rate of earthquakes, thereby providing the designer with a complete description of the seismic hazard at a site. The framework of PSHA is shown in Fig. 3.3 on the next page.

The first step involves identification of the most likely sources, along with probability distribution of potential rupture location within the source zone. Then this probability distribution is combined with source geometry to obtain the distribution of source-to-site distances. The second step includes characterization of seismicity or temporal distribution of earthquake recurrence, mainly based on seismic catalogues, historical data, and paleoseismological studies. Then the ground motion produced at the site by any size earthquake occurring at any source zone is created using attenuation relationships. These output from the above three steps are combined to obtain the probability that a given ground motion parameter will be exceeded during a given time period (Hashash et al., 2001).

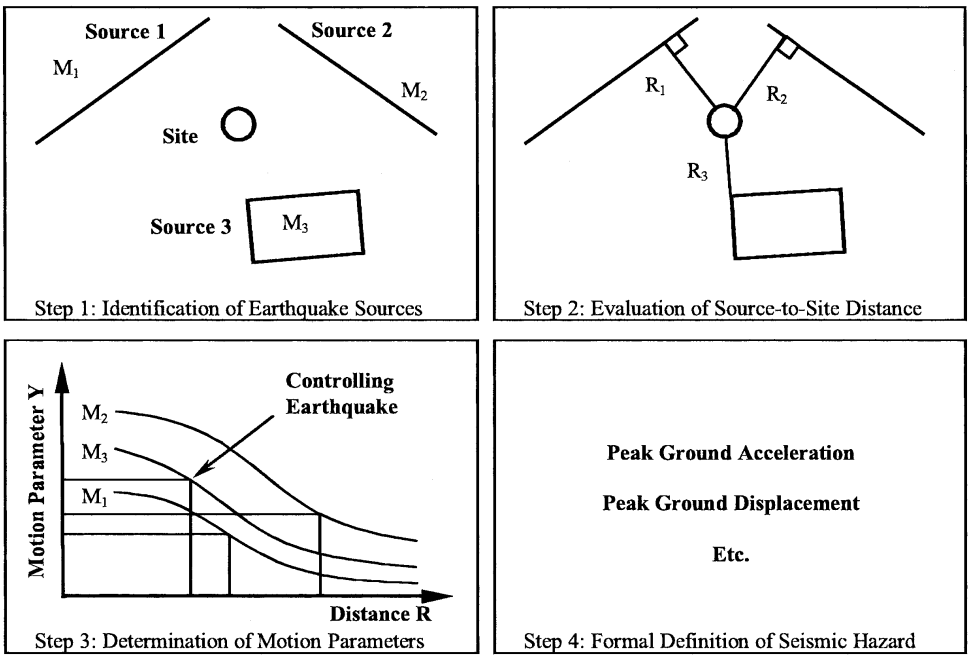

FIGURE 3.2: Deterministic seismic hazard analysis. After Reiter, 1990, cited in Hashash et al. (2001).

Based on the purpose of the ground structure, the level of design earthquake is defined. In current practice, dual level design criteria is followed where a higher level, commonly known as Maximum Design Earthquake (MDE), earthquake is aimed at life safety and the lower level, known as Operating Design Earthquake (ODE), is for economic risk exposure. In DSHA, the maximum design earthquake is defined by the maximum level of shaking that is expected at the site and in PSHA, MDE is defined as an event that has small likelihood of occurrence (3-5 %). The operating design earthquake, on the other hand, is an earthquake that can reasonably

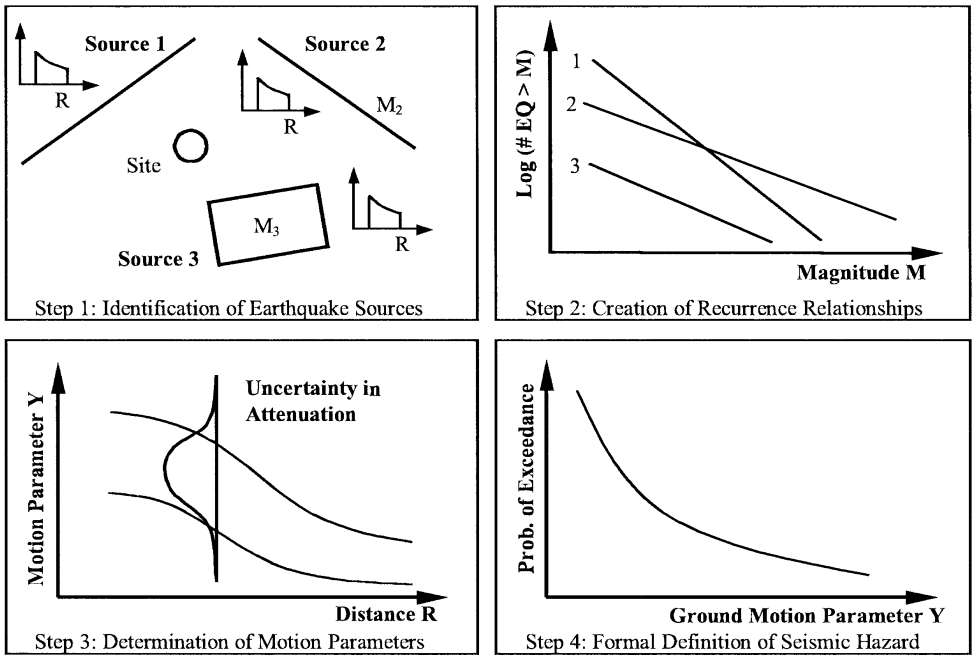

FIGURE 3.3: Probabilistic seismic hazard analysis. After Reiter, 1990, cited in Hashash et al. (2001).

be expected to occur at least once during the design life of the underground structure (an event with probability of exceedence from 40 - 50%) (Hashash et al., 2001).

3.1.1 Ground Motion Parameters

Once the seismic hazard zonation at the site is identified, seismic hazard are often represented in terms of values or probability distributions of accelerations, velocities, or displacements of the ground. Nonetheless, all these parameters are inter-related as integration or differentiation of one produces another. The descriptions and significance of the parameters that can be used to describe a seismic hazard are described in detail in Srbulov (2008) and are reproduced here as follows:

- The ground acceleration is important as the product of the mass of the element and the acceleration is the magnitude of the *inertial force*, which determines the impact from the ground shaking. However, peak ground acceleration, which occurs in high frequency pulses, contains only a portion of the emitted seismic energy and therefore is not appropriate as a single measure of ground motion.

- The ground velocity can be used to indicate the amount of *energy* from the seismic shaking as $KE = \frac{1}{2}mv^2$. The use of ground velocity results in representing the amount of energy emitted during a seismic event. For example, ground motions of smaller amplitude, but longer duration produces larger ground energy and therefore results in more severe destruction.

- The ground displacement of a structure are useful and the damage due to earthquakes can be measured in terms of deformations.

The selection of ground motion parameters, for e.g. peak values, time histories, or spectral response, is equally important and should be chosen appropriately. Single peak values, although easier to implement, are poor indicators of earthquake destructiveness as a single value does not account for the time history of the ground vibration and therefore ignores the accumulation of damage over time. Therefore, time histories of ground motions are used for high risk projects. The spectral response values, on the other hand, are a compromise between singular values and full time history analysis.

Furthermore, although maximum values of ground motion such as peak ground acceleration, velocity, and displacement are commonly used in defining a design earthquake, *effective*, rather than peak, ground motion parameters tend to be better indicators of seismic response (Hashash et al., 2001). Although peak ground acceleration may not be the best indicator of earthquake damage, it is still the most common and widely accepted parameter used to represent earthquake ground motions. Of course, accepting the peak ground acceleration as the damage indicator does not mean that the maximum acceleration is cause of damage, but that it can be employed to determine the level of damage for the expected earthquake (Dowding and Rozen, 1978; FHWA, 2009). Besides, most of the seismic hazard maps are shown using peak ground acceleration, for example the map for India and its adjoining regions as described in Bhatia et al. (1999) is shown in Fig. 3.4. The approximate relationship between peak ground acceleration and various earthquake intensity scales is shown in Fig. 3.5.

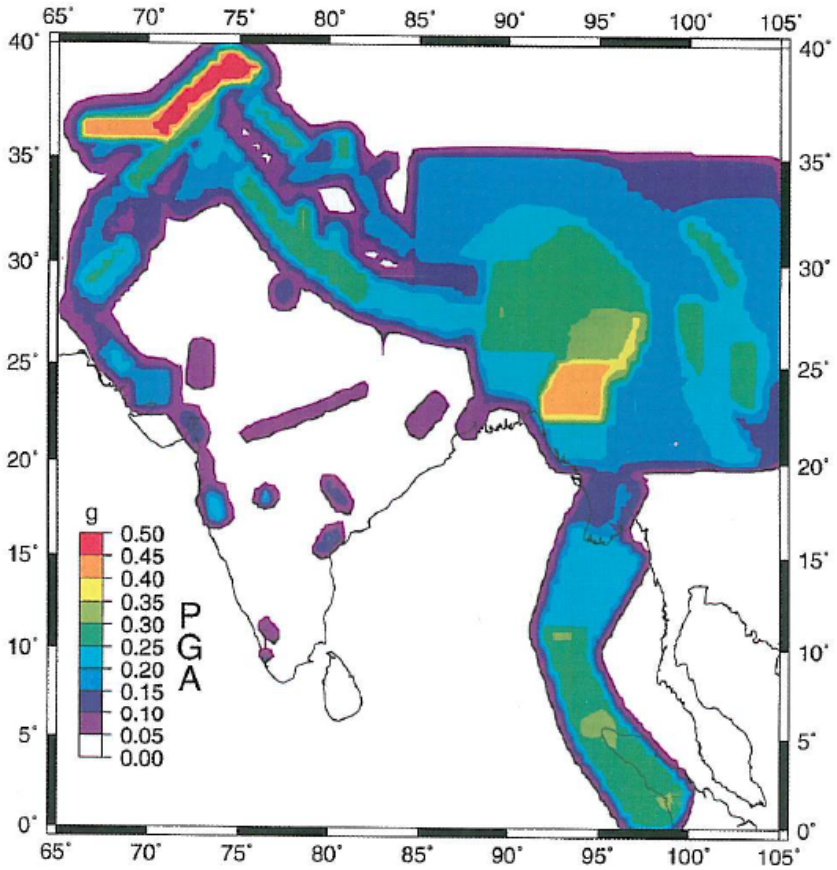

FIGURE 3.4: Seismic map of India and adjoining regions showing 10% probability of exceedance in 50 years. Contour interval = 0.05g. After Bhatia et al. (1999).

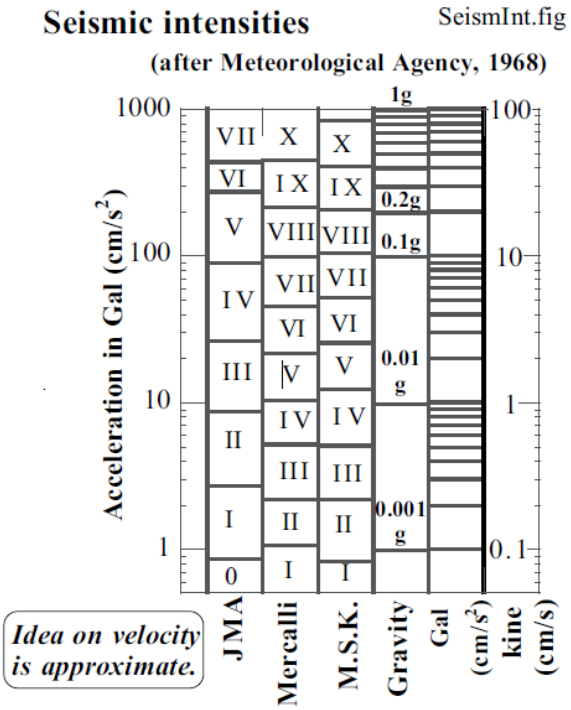

FIGURE 3.5: Comparison of seismic intensities. After Towhata (2008)

3.2 Ground and Structure Response

Once the design ground motion parameter, whether peak or time series of acceleration, velocity, or displacement of the design earthquake has been determined, either by conducting site-specific analysis or from existing seismic zonation maps, the tunnel response with reference to the ground response can be analyzed using any of the three approaches described in Bilotta et al. (2007) and are produced here as follows:

> Pseudo-static analysis, where the seismic input is reduced to equivalent inertia force or peak strain amplitude, computed through a free-field ground pseudo-static analysis, and then considered acting on the tunnel lining in static conditions as well.
>
> Simplified dynamic analysis, where the soil straining is computed through a dynamic free-field seismic response analysis, and then applied to the tunnel section or axis, again in pseudo-static conditions, eventually accounting for the kinematic tunnel-soil interaction in a simplified way.
>
> Full dynamic analysis, where the soil and tunnel responses are mechanically coupled and analysed via numerical modeling, such as dynamic finite element or finite difference methods.

Before determining the type of analysis to be used, it is worthwhile to revisit the problem at hand, where a 10-m diameter circular tunnel at 60-m depth, in rock masses with Q= 1 - 40, is a good representative model. Most of the tunnels are constructed at an average depth of 100 m (Bhasin, 2011). For the 41 cases studied in Dowding (1979), the average depth of the tunnels was 100 m, with median depth of 50 m. A typical road or water tunnels have diameters around 5 m to 10 m. Besides, as reported in Sharma and Judd (1991), shallow tunnels are more

susceptible to earthquakes and therefore modeling a tunnel at 60 m depth to study to effect of earthquakes on tunnels is of interest.

In this study, the plane strain 2D approximation is used to analyze the effect of earthquakes in view of the deformation due to ovaling effect in the plane perpendicular to the tunnel axis. The ovaling effect, which is the critical mode of deformation in tunnels (Kontoe et al., 2008), is mainly caused by shear waves propagating perpendicular to the tunnel axis (see Fig. 3.1).

Assuming that the tunnel is located in the far-field of the source of earthquake, the shear and surface (Rayleigh) waves, which are produced by reflections and wave conversions en route from the source to the tunnel location, dominate the ground motions (Dowding, 1984). In the same article, it was stated that the typical frequencies of the seismic waves in far-field ranges from 0.1 - 10 Hz.

Using the relationship between rock mass quality Q and its P-wave velocity V_p at 25 m depth from Barton (2002),

$$V_p(km/s) \approx 3.5 + \log Q_c \tag{3.1}$$

Assuming that $Q_c = Q$, as discussed in Chapter 4, the P-wave velocities for rock masses with Q = 1 - 40 are:

$$V_p = 3.5 - 5.1\ km/s$$

Considering the assumption for Poisson's solid[2], the shear wave velocity V_s and the Rayleigh wave velocity V_r can be determined as shown in Stein and Wysession (2003):

$$V_s = \frac{V_p}{\sqrt{3}} \tag{3.2}$$

$$V_r = 0.92V_s \tag{3.3}$$

Since the velocity of surface waves are nearly equal to the velocity of shear waves, only shear wave velocity shall be used for comparison from here. Thus, for Q ranging from 1 to 40, the shear wave velocities are:

$$V_s = 2.0 - 2.9\ km/s$$

Using the f = 10 Hz for seismic waves in far-field of the earthquake source and V_s = 2.0 km/s for the rock mass with Q = 1, it can be estimated that the wavelength λ of the seismic waves are on the order of

$$\lambda = V_s/f = 2.0/10.0 \times 1000 \approx 200m.$$

Considering a 10-m diameter tunnel in rock mass with Q = 1, the wavelength of the seismic waves perturbing the tunnel is on the order of 20 times the diameter of the tunnel; the wavelengths in rock masses with $Q > 1$ will be > 200 m. Under such scenario where the wavelength is many times larger than the opening diameter, there is "no dynamic interaction and the tunnel responds as if the peak pressure associated with the wave were loading the tunnel in static

[2]For simplification of seismological problems, it is often assumed that the Lame parameters λ and μ are equal. Such a material is called Poisson's solid. Its Poisson's ratio $\nu = 0.25$, Young's modulus $E = (5/2)\nu$, and Bulk Modulus K=$(5/3)\mu$ (Stein and Wysession, 2003)

manner" (Dowding, 1984). At this wavelength to tunnel dimension scale, the whole tunnel experiences the same loading due to passing seismic waves and thus responds to earthquakes as if it is statically loaded (Kaynia, 2011). A schematic diagram showing the relative size of the tunnel dimension D and wavelength λ is shown in Fig. 3.6.

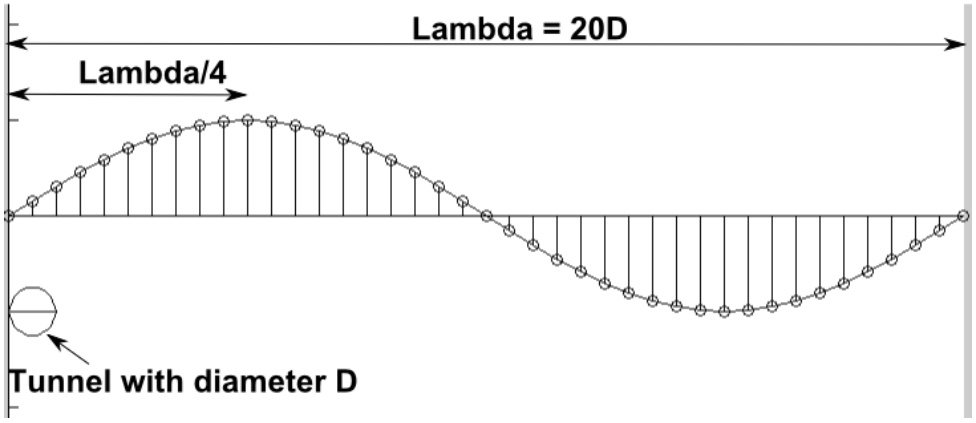

FIGURE 3.6: Comparison of wavelength $\lambda = 200D$ and tunnel diameter D. For rock mass with Q=1, λ is > 200 m and the diameter of the tunnel under study is taken as 10 m.

Owing to the above-mentioned large "wavelength to opening dimension" ratio in rock masses, the application of pseudo-static seismic loading, which is implemented in Phase^2, to simulate earthquake loading on tunnels surrounded by rock masses with Q = 1 or more is justified. On the other hand, the situation could be more complicated for tunnels in soils as, owing to its low shear wave velocity, the wavelength could become comparable to the opening dimension and therefore warrant the need to undertake more complicated dynamic analysis.

The implementation of tunnel response analysis using pseudo (or quasi) static approach can be grouped into two approaches: (1) Ground-Deformation-Based Method and (2) Inertia-Force-Based Method (Luo et al., 2002). The deformation based method, which is described in detail in Hashash et al. (2001), is based on the principle of calculating the shear strain due to earthquakes at the tunnel depth and then to imposing this strain onto the tunnel structure. On the other hand, the Inertia-based method adds an additional force to the model to simulate earthquake loading. The additional inertial force is equal to the product of the seismic coefficient, related to the peak ground acceleration, and the weight of the element in the model. The quasi-static seismic loading in Phase^2(Rocscience, Inc., 2002), as discussed in the following section, is an Inertia-based method.

3.3 Pseudo-static Seismic Loading in Phase^2

In Phase^2 finite element modeling program, seismic loading is based on pseudo-static approach, where the additional seismic force is calculated as product of the specified seismic coefficient, *a dimensionless vector*(see Section 3.3.1), and the *amplitude* of the body force, which is the self weight of a finite element. Then, to simulate seismic loading during earthquakes, the calculated seismic force is *vectorially* added to the downward acting body force as an additional load to *each finite element in the mesh* (Rocscience Inc., 2001). Thus, the effect of the seismic ground motion, which is as discussed earlier both time and space dependent, is reduced into a seismic

coefficient and is assumed to be constant in both time and space. The seismic coefficient in Phase^2 can have a horizontal component and a vertical component, whereby it is possible to specify both magnitude and direction of the seismic loading (see Fig. 3.7).

The seismic coefficient is usually assumed to decrease with depth as the ground motion during earthquakes also decreases with depth. In Phase^2, since same seismic coefficient is applied to each finite element in the model, the variation of the intensity of seismic ground motion as a function of depth is neglected in this study and the seismic coefficient relating to the expected ground motion at the tunnel depth is applied throughout the model. In absence of more accurate site-specific depth reduction factor models, the guideline in Hashash et al. (2001) as shown in Table. 3.1 can be used. For instance, a seismic coefficient of 0.30 used in a model in Phase^2, which is the seismic coefficient at tunnel depth of 60 m, corresponds to a seismic coefficient of $0.30/0.70 \approx 0.43$ at ground surface.

Tunnel depth (m)	**Ratio of ground motion at tunnel depth to ratio of surface ground motion**
≤ 6	1.0
6 - 15	0.9
15 - 30	0.8
> 30	0.7

TABLE 3.1: Ratios of ground motion at depth to motion at ground surface. After Power et al.(1996) cited in Hashash et al. (2001)

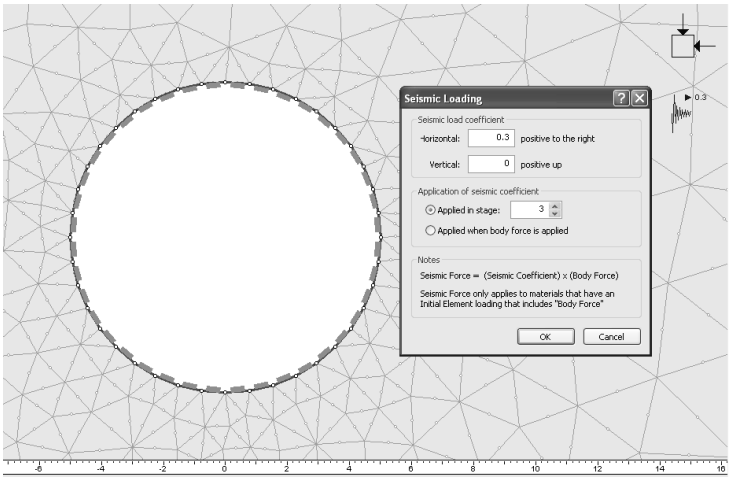

FIGURE 3.7: Dialog box in Phase2 for seismic loading. Seismic loading with horizontal seismic coefficient =0.3 and vertical coefficient =0 is applied to the model in Stage 3.

The main limitation of this method is the determination of a representative seismic coefficient that effectively captures the effect of the ground motion which is both time and space variant and transient in nature. Since a transient ground motion is represented by an additional force proportional to the seismic coefficient that is applied in a static manner, this method often "overestimates the risk of earthquakes" (Towhata, 2008). In principle the value of the seismic coefficient should depend on the ground motion parameters – such as peak ground acceleration, frequency content, and duration – and the nature of the tunnel structure and the surrounding

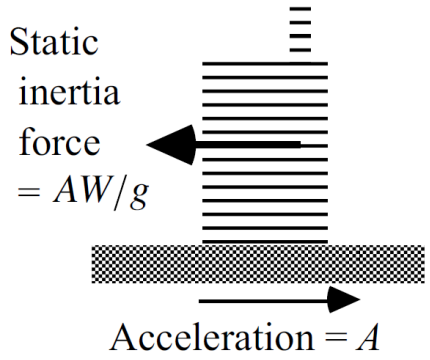

FIGURE 3.8: d'Alembert's principle of Mechanics. After Towhata (2008)

.

rock mass (Aversa et al., 2009). Therefore, the determination of the seismic coefficient and its relationship with other ground motion parameters, such as peak ground acceleration, will be discussed in detail in the next subsection.

3.3.1 Seismic Coefficient K

The *seismic coefficient* is the cornerstone parameter of earthquake loading analysis as this single parameter is used to simulate the passing seismic wave, a dynamic time- and space-dependent phenomenon. As discussed earlier, the seismic coefficient is a dimensionless vector, with a horizontal and a vertical component. The seismic coefficient discussed here is the horizontal seismic coefficient K_h and the effect of the vertical seismic coefficient K_v will be discussed in the latter part of this section.

The interaction of seismic waves with a tunnel depends on frequency content, amplitude, and duration of shaking, among others. Since implementing a methodology to account for all these parameters needs complex approaches that would require more resources both in terms of time and data, adopting a realistic pseudo-static method using an appropriate seismic coefficient is a satisfactory alternative. It appears that application of pseudo-static limit equilibrium analysis using *seismic coefficients* to model earthquake loading is widespread for above surface structures such as slopes and dams (Towhata, 2008; Baker et al., 2006). Thus, most of the literature on determination of seismic coefficient from ground motion parameters such as peak ground acceleration lay focus on surface structures, which behave in a strikingly different manner during earthquakes when compared to underground structures such as tunnels. For instance, for surface structures, the inertia of the structures dominates the response of the structure to earthquakes, but, on the contrary, the response of the confining rock mass has greater effect on the overall response of a tunnel (Hashash et al., 2001).

Three procedures to determine the seismic coefficient are presented here. The first two methods (Towhata, 2008; Baker et al., 2006) focus on near surface structures, primarily dams and slopes. The third method as suggested by Kaynia (2011) is suitable for tunnels in rock masses (i.e. high shear wave velocity) and is therefore used in this thesis.

According to Towhata (2008), the background of the seismic coefficient is based on the d'Alembert's principle of mechanics (see Fig. 3.8). This principle states that when an acceleration A is applied at the base of a structure, the overall structure experiences in opposite direction

a shaking equivalent to $(A/g)W$, where g is the acceleration due to gravity and W is the weight of the structure; thus the seismic coefficient K "appears to be equivalent to A/g". On the other hand, the value of K depends on the local seismic activity, the importance of the structure, and local geologic condition. The value of K now used in Japan is 0.15 - 0.20 or greater (Towhata, 2008).

It was observed that, during the 1994 Northridge earthquake, the hut shown in Figure 3.9 survived although the maximum horizontal acceleration of 1.9 g was recorded at Tarzana site, within tens of meters from the hut. Thus, the relationship between K and g is unclear for this particular hut could not have withstood a horizontal static force which could have been 1.9 times its weight (Towhata, 2008).

FIGURE 3.9: A small hut that survived the 1994 Northridge earthquake. After Towhata (2008)

Based on a study by Noda et al. (1975) on damage of quay wall near harbors, cited in Towhata (2008), Eqn. 3.4 showing the relationship between A^h_{max}, the maximum horizontal acceleration, and K was proposed. The correlation plot between K and A^h_{max} to obtain the above relationship is shown in Fig. 3.10. Through Limit-Equilibrium Analysis of the damaged quay walls, Noda et al. (1975) back-calculated the critical K required to induce the observed failure during earthquakes. These critical K values were plotted as "Equivalent K" along the y-axis in Fig. 3.10. The maximum horizontal acceleration at the site was obtained from records at nearby sites and plotted along x-axis. Although this approach is an "unique attempt" to correlate K and A^h_{max}, there are many uncertainties associated in the study including the determination of soil strength in the limit equilibrium analysis (Towhata, 2008). Nonetheless, the relationship shown in Equation 3.4 has a better fit to the data than $K = \frac{A_{max}}{g}$.

$$K_h \approx \frac{1}{3}\sqrt[3]{\frac{A^h_{max}}{g}} \tag{3.4}$$

A range of horizontal peak ground acceleration and their corresponding seismic coefficient K as per Eqn. 3.4 are shown in Table 3.2. It appears that the values of horizontal peak ground acceleration and seismic coefficients are almost equal for lower PGA ($\leq$ 0.2 g). For higher PGA, the value of the seismic coefficient is significantly lower than PGA. For example, at PGA = 1g, K is about one-third of the PGA.

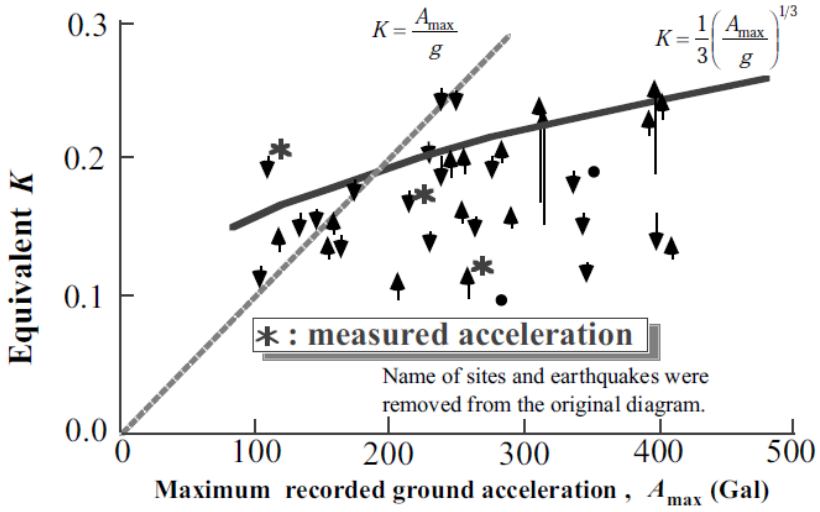

FIGURE 3.10: The correlation between maximum horizontal acceleration and seismic coefficient K_h. After Noda et al. 1975, cited in Towhata (2008).

PGA (g)	K	PGA(g)	K
0.1	0.15	1.1	0.34
0.2	0.19	1.2	0.35
0.3	0.22	1.3	0.36
0.4	0.25	1.4	0.37
0.5	0.26	1.5	0.38
0.6	0.28	1.6	0.39
0.7	0.30	1.7	0.40
0.8	0.31	1.8	0.41
0.9	0.32	1.9	0.41
1.0	0.33	2.0	0.42

TABLE 3.2: Horizontal Peak Ground Acceleration and their corresponding K values using the relationship in Eq. 3.4.

Baker et al. (2006) presented another procedure to determine the horizontal seismic coefficient, for slope stability analysis, as a function of the peak ground acceleration and magnitude of the earthquake. The charts presented in their paper are reproduced here in Fig. 3.11 on the next page. From chart (a), the ratio between horizontal seismic coefficient and peak ground acceleration is 0.5 for Magnitude > 8 earthquake, whereas the same ratio drops to 0.2 for a Magnitude < 6.5 earthquake.

The horizontal seismic coefficient discussed so far are for the impact of earthquakes on above surface structures such as slopes and dams. However, the response of underground structures like tunnels, especially in rocks, will be different from those of above-surface structures. As a general trend, the velocity of waves in near-surface materials are lower than those at depth. This phenomenon results in shorter wavelength waves near the surface than at depth. Coupled with larger structures constructed at the surface than at depth, these shorter-wavelength-waves result in more complex dynamic interaction with above-surface structures as the wavelength approaches the dimension of the structures.

In contrast, as shown in Fig. 3.6, the wavelength of the seismic waves in rock masses at

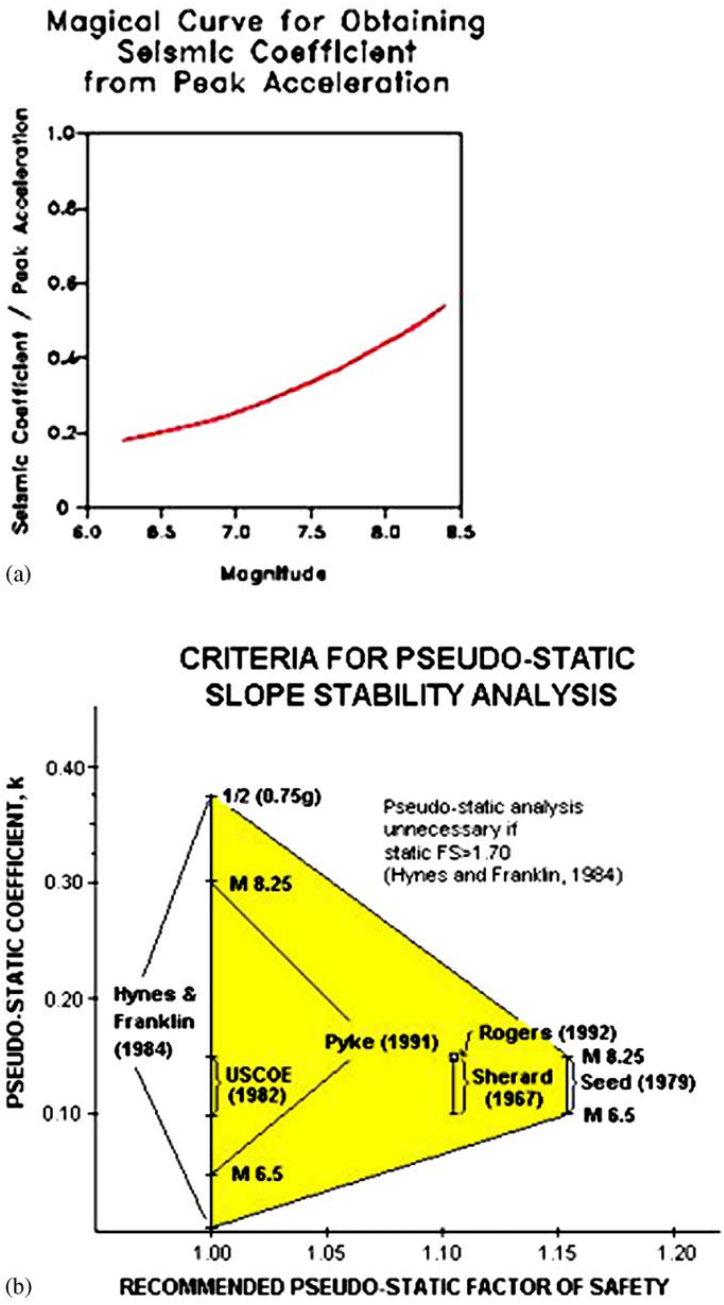

FIGURE 3.11: Design recommendations for pseudo-static analysis: (a) Pyke (1991) and (b) California Division of Mines and Geology (1997). Reproduced from Baker et al. (2006).

depth are much larger than the opening dimension and therefore dynamic interaction is small and the passing elastic waves result in a mere static application of an additional load on the tunnel (Dowding, 1984). At any instant, when the seismic wave passes through the tunnel, the whole tunnel experiences the same force and therefore move in the same direction. Owing to this phenomenon, Kaynia (2011) suggested using the ratio of peak ground acceleration to the acceleration due to gravity as the seismic coefficient. Thus, this expression for horizontal seismic coefficient K_h is used throughout this thesis:

$$K_h = \frac{A^h_{max}}{g}$$

For instance, if the expected peak horizontal acceleration A^h_{max} at the tunnel depth is 0.4g, the horizontal seismic coefficient K_h used to represent this seismic intensity is equal to 0.4. As discussed earlier, the surface PGA corresponding to this seismic coefficient at tunnel depth will then be $0.4/0.7 \approx 0.6$g using 0.7 as the reduction factor for 60-m depth as per Table 3.1.

Influence of Vertical Seismic Coefficient K_v

The seismic coefficient discussed thus far is the horizontal seismic coefficient, which is related to the horizontal peak ground acceleration. The magnitude of vertical acceleration is usually lower than the horizontal acceleration – ranging from a quarter to one-fifth of the horizontal acceleration (Barton, 1984) (recorded at a simulated depth of ca. 20 m during the joint Norwegian-Swedish study of underground siting for nuclear plants) to half of horizontal acceleration (Towhata, 2008) (from data recorded during the 1995 Kobe earthquake). But according to Kaynia (2011), the vertical peak ground acceleration can be anywhere from half or even equal to the horizontal peak ground acceleration.

As per Towhata (2008), the horizontal seismic coefficient gained more attention than vertical acceleration due to two reasons: (1) horizontal acceleration is larger than vertical acceleration and (2) any surface structure has resistance against vertical motion. Usually the increase in static force (20-50 %) due to vertical motion is still within the safety margin, and most failures in masonry structures are caused by horizontal inertial force.

On the other hand, for underground structures, the vertical motion is expected to have a higher impact on the structure than for surface structures as, at least the upper half portion, an underground structure does not have any structural resistance or support from underneath against vertical motion as the rock mass below it have been excavated. In other words, tunnels are susceptible to damage due to both horizontal and vertical loads, where the roof of the tunnel appear to be more susceptible to the vertical component. Therefore, for a conservative analysis, it is of utmost importance to consider the vertical seismic coefficient together with horizontal seismic coefficient during pseudo-static loading.

Although the vertical peak ground acceleration A^v_{max} can range from 0.5 A^h_{max} to A^h_{max}, Kaynia (2011) suggested using

$$K_v = 0.5K_h$$

It may be noted that there is some phase-lag between the horizontal peak ground acceleration and vertical peak ground acceleration. Taking $K_v = 0.5K_h$ partially accounts for this phenomenon as, due to the phase-lag, the actual effect will be lower than the net sum of the loads due to peak horizontal and peak vertical ground accelerations (Kaynia, 2011). When a horizontal seismic coefficient is specified, although not explicitly mentioned, there is always an intrinsic assumption in this study that a $K_v = -0.5\ K_h$ (in downward direction) is always coupled with the horizontal seismic coefficient K_h. The choice of the downward (negative) direction for the K_v will be explained using the findings from the numerical experiments conducted as follows.

A set of numerical analysis case studies were carried out to investigate the effect of vertical seismic coefficient using the pseudo-static seismic loading procedure in Phase^2. The four seismic loading scenarios, as shown below, are applied to the same tunnel model – 20 m diameter tunnel at 60 m depth in a rock mass with Q = 1.

1. K_h = *0.30 and* K_v = *0.* As is commonly followed for analysis of surface structures, this case ignores the effect of vertical seismic coefficient and sets it equal to zero.

2. K_h = *0.30 and* K_v = *0.24.* This seismic loading scenario considers a positive vertical seismic coefficient, while the horizontal seismic coefficient remains unchanged. The vertical seismic coefficient here is adding an inertial force in the opposite direction as the downward force due to gravity.

3. K_h = *0.30 and* K_v = *-0.24.* This loading case is equivalent to Case 2, except that the sign of the vertical seismic coefficient is negative. Thus, the inertial force, simulating seismic loading, is in the same direction as the downward gravitational force and therefore is added to the self weight.

4. K_h = *-0.30 and* K_v = *-0.24.* This case is same as Case 3, except that the direction of horizontal seismic coefficient is in negative direction. This case was established to investigate the influence of direction of horizontal seismic coefficient on the axial force on the tunnel liner.

The contour plots of the major principal stress σ_1 for the four loading cases described above are shown in Fig. 3.12. It can be clearly seen that the distribution of the major principal stress around the tunnel periphery generally resembles an ellipse, with the maximum stresses located along the long axis of the ellipse. When the direction of horizontal seismic coefficient is reversed, the long-axis of the ellipse is mirrored along the vertical axis. Altering the direction of the vertical seismic coefficient do not result in any drastic change in the location of the long-axis of the ellipse. The magnitude of the stresses around the tunnel is greater when the direction of the vertical seismic coefficient is downward (negative), in the same direction as the gravitational force.

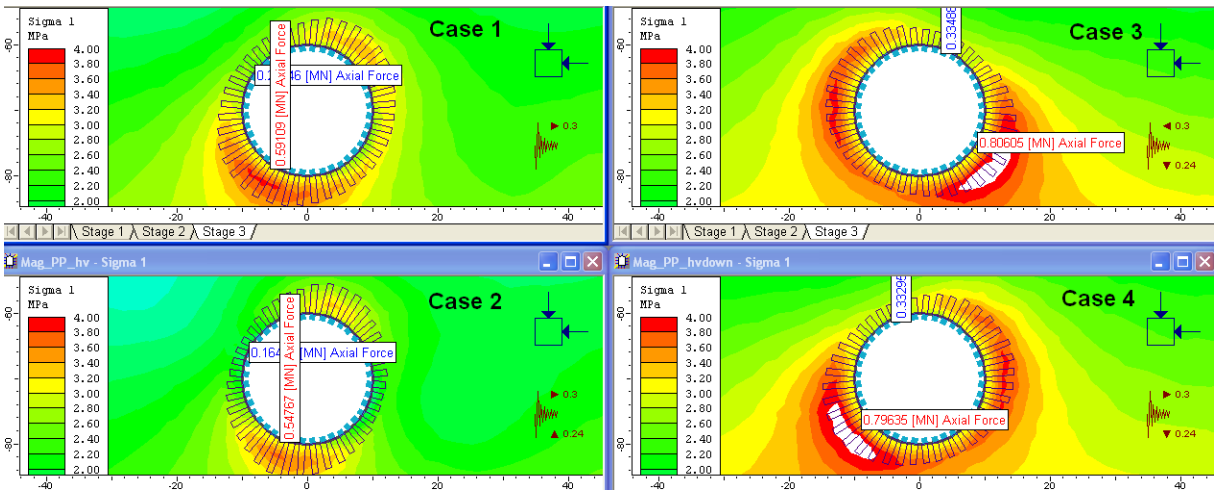

FIGURE 3.12: Contour plot of major principal stress σ_1 for four seismic loading cases; the red labels are Maximum axial force on the lining and the blue labels are the minimum axial force on the lining. The four seismic loading scenarios are as follows: Case 1 - K_h=0.3, K_v=0; Case 2 - K_h=0.3, K_v=0.24; Case 3 - K_h=0.30, K_v=-0.24; Case 4 - K_h=-0.30, K_v=-0.24

The magnitudes of the maximum axial force on the lining (MAFL) are plotted for the four seismic loading scenarios and the resulting MAFL vs. case number plot is shown in Fig. 3.13.

Since Case 1 is when K_h is 0.30 and the vertical seismic coefficient is ignored, the other cases are compared with Case No. 1 to see the effect of the vertical seismic coefficient.

The magnitude of MAFL decreases in Case 2 where the K_v is positive and acts in the opposite direction with respect to the gravitational force. For Case 3, there is a drastic increase in MAFL under seismic loading when K_v is negative, acting in the same direction as the gravitational force. The increase in MAFL for seismic loading as compared with static loading is 37% for Case 1 and 84% for Case 3. This shows that the inclusion of vertical seismic coefficient in the analysis results in a much higher MAFL during seismic loading and could lead to underestimation of the impact of earthquakes if K_v is ignored as for surface structures. Furthermore, a comparison between Case 3 and 4 shows that the effect of the direction of K_h on the magnitude of MAFL is insignificant. This is expected as the pseudo-static seismic approach followed here is mainly governed by the vector sum of additional seismic force and the downward acting body force. In both Cases 3 and 4, the direction of K_h, although opposite to each other, is perpendicular to the gravitational force.

Owing to the above findings, a vertical seismic coefficient $K_v = -0.5K_h$ is always applied in downward (negative) direction for all the experiments using pseudo-static seismic loading in this thesis. For instance, for K_h = 0.30, representing a horizontal PGA at tunnel depth of 0.30g, the $K_v = -0.50 \times 0.30 = -0.15$. Assuming 0.70 as the reduction factor from surface to 60 m depth, surface PGA is ca. $0.30/0.7 = 0.43$g.

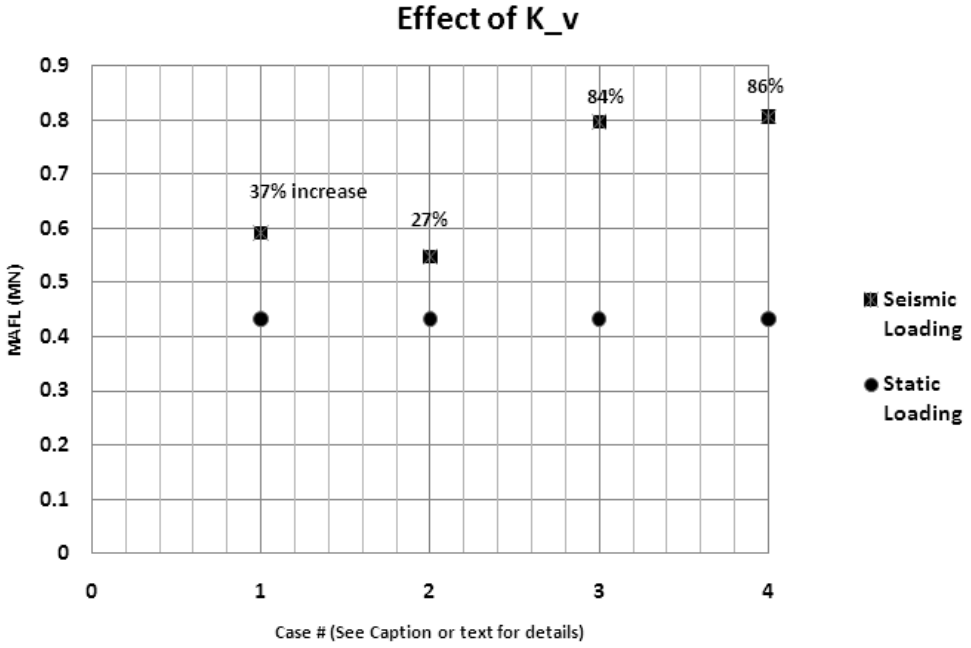

FIGURE 3.13: The effect of vertical seismic coefficient on the magnitude of Maximum Axial Force on the Lining. The four seismic loading scenarios are as follows: Case 1 - K_h=0.3, K_v=0; Case 2 - K_h=0.3, K_v=0.24; Case 3 - K_h=0.30, K_v=-0.24; Case 4 - K_h=-0.30, K_v=-0.24

Chapter 4

Theoretical Background: *Modeling Parameters*

The NGI Q-system (Barton et al., 1974) is a rock classification method used to determine the support for a tunnel placed in a particular rock mass quality. The Q-value of the rock mass under investigation is calculated from the six parameters determined in field using the standard tables (see Section 2.1 on page 11). An updated support chart (see Fig. 2.3 on page 17) is available to determine the support type for the calculated Q-value. Five rock mass classes, which can be classified using four different Q-values, are modeled for this study. Table 4.1 shows the five rock mass classes used for numerical studies and their corresponding Q-values. Furthermore, modeling parameters used to simulate these rock classes in Phase^2 finite element modeling program are discussed in the following sections.

Rock class	I	II	III	IV	V
Description	Very good rock	Good rock	Fair rock	Poor rock	Very poor rock
Q value	> 40	10-40	4-10	1-4	<1

TABLE 4.1: The description and range of Q values for the five rock classes modeled in this study. Adapted from Waltham (2009).

4.1 Deformation modulus

Deformation modulus E_{mass} is the ratio of the stress to the corresponding strain while loading a rock mass. In contrast with Young's Modulus, which is the same ratio in the elastic regime, the deformation modulus includes both elastic and inelastic behavior. The deformation modulus discussed here refers to the *static* deformation modulus. It is an important parameter that governs the behavior of rock mass that includes deformations, particularly for underground excavations. Detailed numerical analysis for tunnel design also requires an estimate of the rock mass deformation modulus and thus the deformation modulus is the "cornerstone of geomechanic analyses" (Palmstrom and Singh, 2001).

The deformation modulus can be measured in-situ using various tests, among which the most common are Plate Jacking Tests (PJT), Plate Loading Tests (PLT), and Radial Jacking Tests (Goodman Jack Test). The testing scheme for these three tests are shown in Figure 4.1. As shown in the figure, a load is applied against the rock mass and the displacement of the loading plates are measured. The measurement of displacement often results in significant inaccuracies resulting from deflection of plates, closure of gaps between the plate and the rock mass, closure of cracks in the blast-damaged or stress-relieved rock in the "influenced zone" (Hoek and Diederichs, 2006). Furthermore, all the deformation tests are expensive and often difficult to conduct and therefore are only conducted in special adits and drifts excavated for mapping the rock mass during the detailed feasibility study of the project.

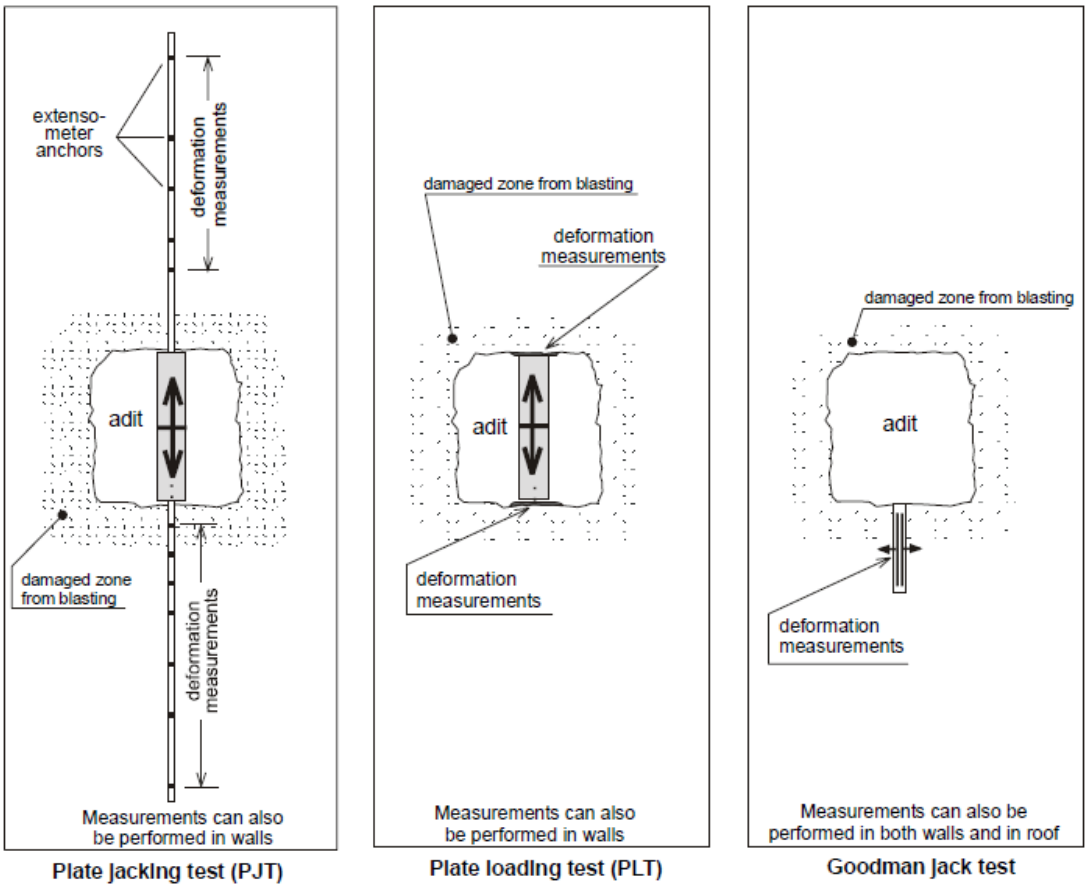

FIGURE 4.1: Set-up for Plate Jacking Test, Plate Loading Test, and Goodman Jack Test. After Palmstrom and Singh (2001)

In addition, there is an issue of scale effect, where different tests measure different portions of the rock mass. For instance, the PLT measures deformation in the rock mass that is in contact with the plate while the PJT measures displacement at multiple points away from the plate. Thus, these two tests always produce different deformation modulus, where the deformation modulus from PJT is higher than PLT as the PLT predominantly measures the deformation modulus of the blast-"damaged zone". Similarly, the deformation modulus obtained from back-analysis of tunnel convergence data will be different from both PJT and PLT as the "test volume" here is larger than for both PJT and PLT.

Fig. 4.2 shows schematic diagram of the result of a cycle of loading of the in-situ deformation modulus test. The slope of the first part of the curve (1), known as initial tangent modulus,

is probably related to mechanical components of the loading system and closing of cracks in the rock mass near the surface and therefore does not have any relation to the in-situ rock mass properties. The slope (3) represents the elastic tangent modulus, or modulus of elasticity, which covers only the elastic regime of the test and the slope of line (4) is the modulus of deformation, which is often used in modeling underground excavations, is the slope for both elastic and anelastic regimes.

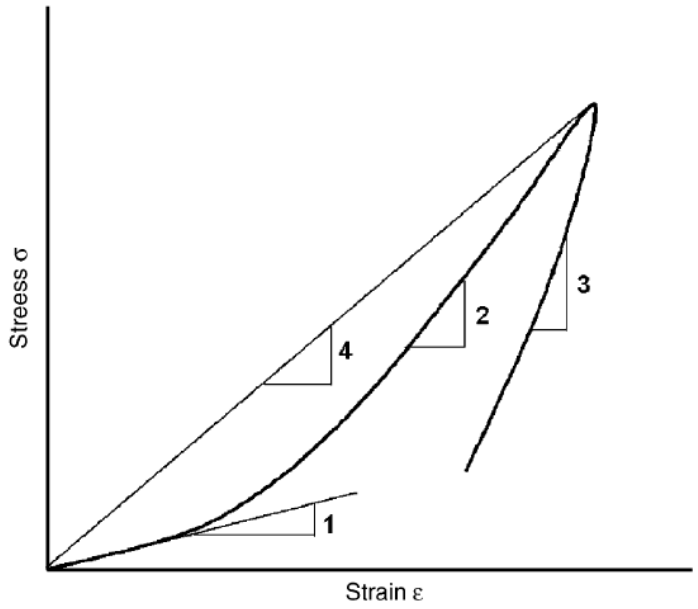

FIGURE 4.2: Alternative definitions for the deformability of rock mass. (1) Initial tangent modulus, (2) elastic tangent modulus, (3) recovery modulus, and (4) modulus of deformation. After Hoek and Diederichs (2006).

Owing to the cost implication and inconveniences associated with in-situ deformation modulus tests, in addition to inherent uncertainties and inaccuracies prevailing in the present in-situ test methods, many authors have established empirical relationships between static E_{mass} and different rock mass classification parameter, such as RMR, Q, GSI, and RMi. As discussed earlier, the rock mass classification parameters are obtained by combination of different geomechanical parameters that can easily be measured in tunnels or at outcrops.

In some instances, the relationship between E_{mass} and the rock mass quality parameter are scaled by other parameters such as unconfined compressive strength (UCS) of the intact rock (Barton, 2002), Young's modulus of the intact rock E_i (Hoek and Diederichs, 2006; Gokceoglu et al., 2003), rock quality designation RQD and weathering degree WD (Gokceoglu et al., 2003), and disturbance factor D, which accounts for the blast-induced disturbed zone around the tunnel periphery (Hoek and Diederichs, 2006).

Mohammadi and Rahmannejad (2010) deployed an artificial neural network (ANN) algorithm to link the six RMR parameters to E_{mass}. The relative error of empirically predicted values from the values determined from plate loading tests were lower for those predicted using ANN than those obtained using existing empirical relationships.

The list of empirical relationships between E_{mass} and rock mass quality parameters are shown in Table 4.2 and Fig. 4.3. Not listed here are the relationship between E_{mass} and GSI, D, and E_i (Hoek and Diederichs, 2006) and relationship between E_{mass} and RMi (Palmstrom,1995).

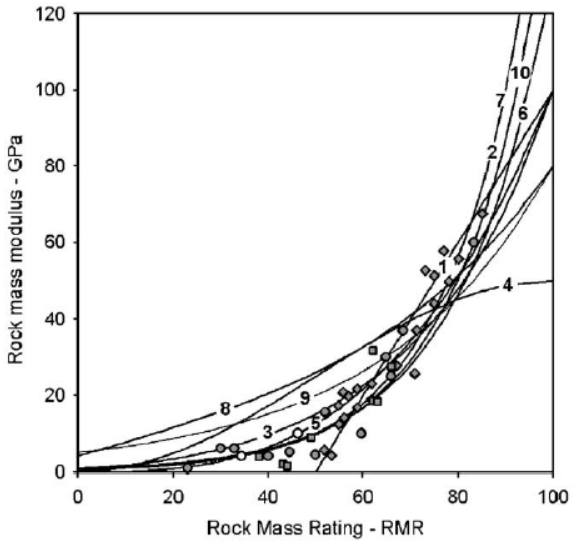

FIGURE 4.3: Empirical relationships compared with data from in situ measurements. After Hoek and Diederichs (2006).

●	Field data	Serafim and Pereira [4]
◆	Field data	Bieniawski [5]
■	Field data	Stephens and Banks [6]
1	$E_{rm} = 2\text{RMR} - 100$	Bieniawski [5]
2	$E_{rm} = 10^{((\text{RMR}-10)/40)}$	Serafim and Pereira [4]
3	$E_{rm} = E_i/100(0.0028\text{RMR}^2 + 0.9\exp(\text{RMR}/22.82)), E_i = 50\,\text{GPa}$	Nicholson and Bieniawski [12]
4	$E_{rm} = E_i(0.5(1 - \cos(\pi\text{RMR}/100))), \quad E_i = 50\,\text{GPa}$	Mitri et al [9]
5	$E_{rm} = 0.1(\text{RMR}/10)^3$	Read et al. [7]
6	$E_{rm} = 10Q_c^{1/3}$ where $Q_c = Q\sigma_{ci}/100$, $\sigma_{ci} = 100\,\text{MPa}$	Barton [8]
7	$E_{rm} = (1 - D/2)\sqrt{\sigma_{ci}/100} \times 10^{((\text{RMR}-10)/40)}, \quad D = 0, \sigma_{ci} = 100\,\text{MPa}$	Hoek et al. [13]
8	$E_{rm} = E_i(s^a)^{0.4}, \quad E_i = 50\,\text{GPa}, s = \exp((\text{GSI} - 100)/9),$ $a = 1/2 + 1/6(\exp(-\text{GSI}/15) - \exp(-20/3)), \quad \text{GSI} = \text{RMR}$	Sonmez et al. [10]
9	$E_{rm} = E_i s^{1/4}, \quad E_i = 50\,\text{GPa}, \quad s = \exp((\text{GSI} - 100)/9)$	Carvalho [11]
10	$E_{rm} = 7(\pm 3)\sqrt{Q'}, \quad Q' = 10((\text{RMR} - 44)/21)$	Diederichs and Kaiser [14]

TABLE 4.2: Empirical relationships referred to in Figure 4.3. After Hoek and Diederichs (2006).

However, as this study is geared toward investigating the effect of earthquakes as a function of rock mass quality Q , the empirical relationship in Eqn. 4.1 (Barton, 2002), is used to determine the E_{mass} for different Q-values. This relationship is shown as serial # 6 in Table 4.2. The graphical representation of the data that was used to obtain this relationship is shown in Figure 4.4.

$$E_{mass} = 10\, Q_c{}^{\frac{1}{3}} \tag{4.1}$$

where the normalized $Q_c = Q * \frac{\sigma_c}{100}$ and σ_c is the uniaxial compressive strength in MPa of the intact rock. For this study, σ_c is assumed to be 100 MPa for all experiments and, therefore, $Q = Q_c$. Physically, this means that this study assumes a continuum rock masses with identical intact rock properties (i.e. constant σ_c). The different Q-values of the rock masses are attributed to the different nature of background jointing, which exhibits as different E_{mass} for different Q-values.

As Phase^2 requires Young's modulus to model elastic and elastic-plastic materials, deformation modulus is consistently used in the place of Young's modulus. The deformation moduli

for the five rock classes investigated here is shown in Table 4.3.

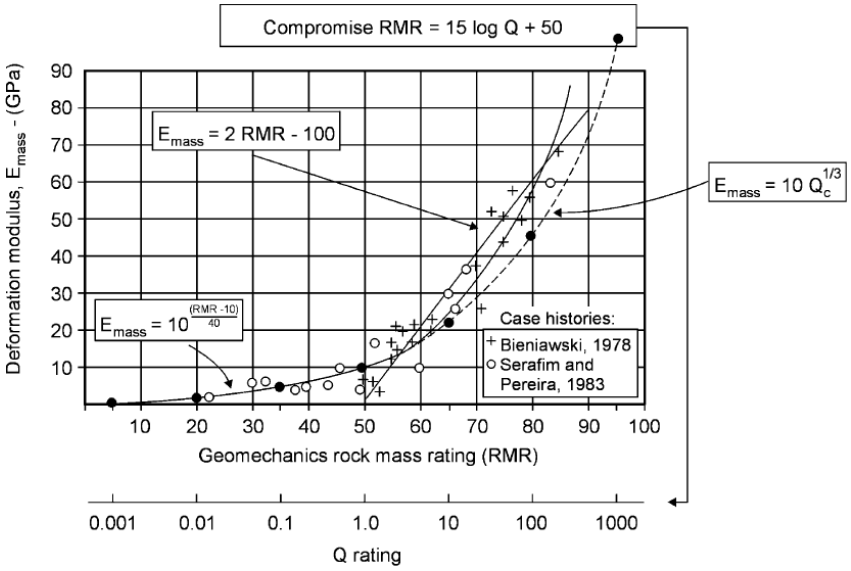

FIGURE 4.4: Static deformation modulus E_{mass} Vs. RMR and Q. After Barton (2002).

4.2 Shear Strength

It is assumed for this study that the rock material behaves as Coulomb material[1], therefore, Mohr-Coulomb criterion is used to determine the shear strength of the rock material. This assumption is valid as the model for this study is assumed to be homogeneous, isotropic material that has the properties of the rock of specified rock mass quality Q. Although the presence of background jointing could be reflected in lower E_{mass} and lower strength parameters, no dominant joints are modeled in this thesis.

4.2.1 Peak Strength Parameters

The peak shear strength of a material can be determined from the angle of internal friction ϕ and cohesion c using the Mohr-Coulomb failure criterion equation (Eq. 4.2).

$$\tau = c + \sigma \, tan\phi \tag{4.2}$$

where τ is the peak shear strength, c is the cohesion in MPa, σ is the normal stress perpendicular to the failure plane, and ϕ is the angle of internal friction.

The table of peak Mohr-Coulomb parameters for different RMR values is available in Bieniawski (1979). Waltham (2009) modified the same table by including the corresponding Q-values for the five rock mass classes shown in Table 4.1. Thus, the peak cohesion c_p and angle of internal friction θ_p for different Q-values are obtained from the above two sources.

[1] An ideal Coulomb material is one where there is a linear relationship between the shear stress τ along a slip plane and the normal stress σ acting on the plane. This represents a "special case of rigid-plastic materials in the same way as Hookean solids and Newtonian fluids are special cases of elastic solids and viscous fluids". Chap. 3 in (Nedderman, 1992). In other words, it is a material where Mohr-Coulomb strength criterion is applicable.

Nonetheless, the peak cohesions stated in the above two sources are applicable to rock slopes only in saturated and weathered rock mass. Singh and Goel (2006) suggested increasing the peak cohesion by an order of magnitude for underground structures (see Table 4.3). The magnitude of c_p obtained after increasing by an order of magnitude is in the same range as the values recorded for the few practical examples cited in Hoek and Brown (1997).

4.2.2 Residual Strength Parameters

Singh and Goel (2006) states that Mohr's theory will be applicable to determine the residual strength of a rock mass as it will be reduced into a non-dilatant soil-like material. They also suggested that the residual angle of internal friction ϕ_r is about 10° less than the peak angle of internal friction as long as ϕ_r is greater than 14° and the assumed residual cohesion c_r is approximately equal to 0.1 MPa.

For this study, the above suggestions have been followed and the peak values of angle of internal friction and cohesion discussed above have been reduced accordingly to obtain the corresponding residual parameters. The peak and residual Mohr-Coulomb parameters for the four Q-values used in this study are shown in Table 4.3.

Q value	E_{mass}	Peak Friction Angle ϕ_p	Peak Cohesion c_p	Residual Friction Angle ϕ_r	Residual Cohesion c_r
	GPa	Degree	MPa	Degree	MPa
1	10.00	15	1	15*	0.1
4	15.87	25	2	15	0.1
10	21.54	35	3	25	0.1
40	35.20	45	4	35	0.1

TABLE 4.3: Q-values for five rock classes and their corresponding static deformation modulus E_{mass}, and both peak and residual Mohr-Coulomb parameters. * $\phi_p = \phi_r$ as ϕ_r should be > 14°

4.2.3 Post-failure Characteristics

While using numerical modeling to study the failure of rock masses, especially for elastic-plastic models, after choosing the failure criterion, it is imperative to specify the post-failure characteristics. Depending on the rock mass quality and stress conditions, the common post-failure behaviors for elastic-plastic models are elastic-perfectly-plastic, strain-softening, and elastic-brittle-plastic. Although no fixed rule exists for the choice of the post-failure characteristics, Hoek and Brown (1997) suggested these as starting points: elastic-brittle-plastic for very good quality hard rock mass (> 75 GSI), strain-softening for average quality rock mass (between 25 and 75 GSI) and elastic-perfectly-plastic for very poor quality rock mass (< 25 GSI).

Using the these two relationships – Eq. 4.3 from Hoek and Brown (1997) and Eq. 4.4 from Barton (2002), the corresponding approximate Q values for these three regimes are: > 100 Q for good quality, between 100 Q and 0.1 Q for average quality, and < 0.1 Q for poor quality rock

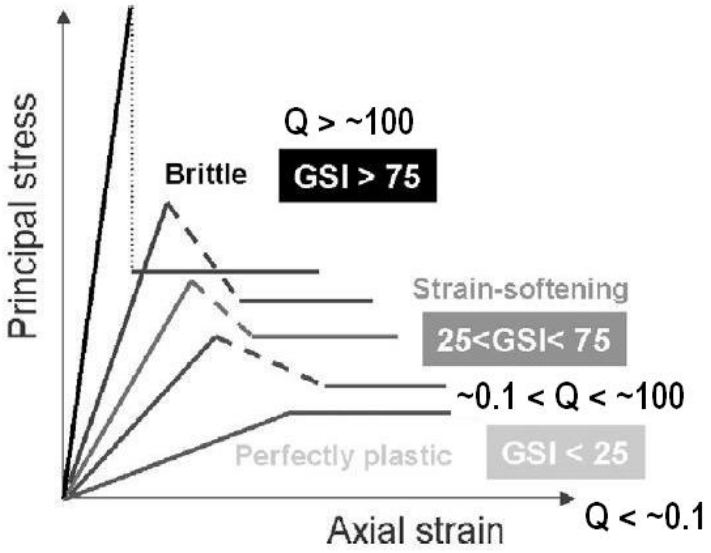

FIGURE 4.5: Schematic diagram showing three post-failure behaviors and their corresponding inferred range of rock mass qualities. Based on Alejano et al. (2009)

mass (see Fig. 4.5). From these three regimes, it can be inferred that strain-softening model should be used for all five rock mass classes used for this numerical experiment.

$$RMR_{89} = GSI + 5 \tag{4.3}$$

$$Q = 10^{\frac{RMR-50}{15}} \tag{4.4}$$

In case of elastic-perfectly-plastic materials, the peak strength is equal to the residual strength, whereas for elastic-brittle-plastic materials, the post failure strength drops instantaneously from peak to residual strength. On the other hand, the strength of the strain-softening model is progressively reduced after failure from peak strength to a generally low residual value (Egger, 2000; Alejano et al., 2009). The rate of reduction from peak to residual strength is governed by the drop modulus M, which is the slope of the downward linear plot, shown by dashed lines in Fig. 4.5.

The drop modulus M, or softening rate ω (Egger, 2000), has been shown to have great influence on the stability of the tunnel. Besides, the softening rate ω for a given rock type is not constant, but depends on the confining pressure (Egger, 2000). For instance, a sample of marble behaves as elastic-brittle at zero confining pressure, but becomes ductile with increasing confining pressure until it eventually becomes elastic-perfectly-plastic (see Fig. 4.6 on the following page). In addition, the strain-softening model is plastic-strain dependent and the post-failure behavior is governed by the strain-softening parameter η (Guan et al., 2007; Alejano et al., 2009).

It can be expected that modeling strain-softening behavior would require a few more parameters, such as strain-softening parameter η and drop modulus M, which is both stress- and strain-dependent. The relationships, either empirical or otherwise, to obtain these additional parameters are not readily available for all rock classes under study. Since assuming any generic value would include more uncertainty into the experiment, the rock masses used for this study

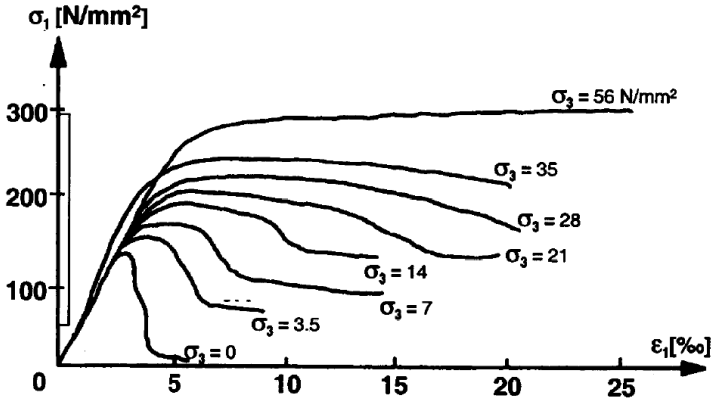

FIGURE 4.6: Results of triaxial compression tests on marble with various confinement pressures. After Egger (2000).

were assumed to behave as *elastic-perfectly-plastic* materials.

Assuming perfectly-plastic model, instead of brittle-plastic, is more appropriate as further studies will focus on weaker rock masses, where higher effects of earthquakes are expected (Abokhalil, 2007; Bhasin et al., 2010) and as weaker rock masses are known to behave as elastic-perfectly-plastic materials (Hoek and Brown, 1997; Basarir et al., 2010).

The stress-strain plots for the four Q-values modeled as elastic-perfectly-plastic materials are shown in Fig. 4.7. Since the value of the stress at failure point corresponds to the peak uniaxial compressive strength of the rock mass, the stress-strain plots shown in Figure 4.7 is for zero confining pressure. The unaxial compressive strength σ_{cm} was calculated from the Mohr-Coulomb parameters c and ϕ using Eqn. 4.5 from Hoek and Brown (1997). The σ_{cm} calculated for the four Q-values are shown in Table 4.4.

$$\sigma_{cm} = \frac{2c\cos\phi}{1-\sin\phi} \tag{4.5}$$

Rock Mass Class	Q value	Peak σ_{cm} (MPa)
Very Poor	1	2.6
Poor	4	6.3
Good	10	11.5
Very Good	40	19.3

TABLE 4.4: Uniaxial compressive strength for four rock classes calculated using Eqn. 4.5 and peak Mohr-Coulomb parameters from Table 4.3

In addition to elastic-perfectly-plastic model, the elastic models for all the rock classes are also investigated. For an elastic model of a particular rock mass type, the slope of the stress-strain curve is proportional to the specified deformation modulus, but the rock mass never reaches failure point, and continues to behave as elastic materials for all stress levels.

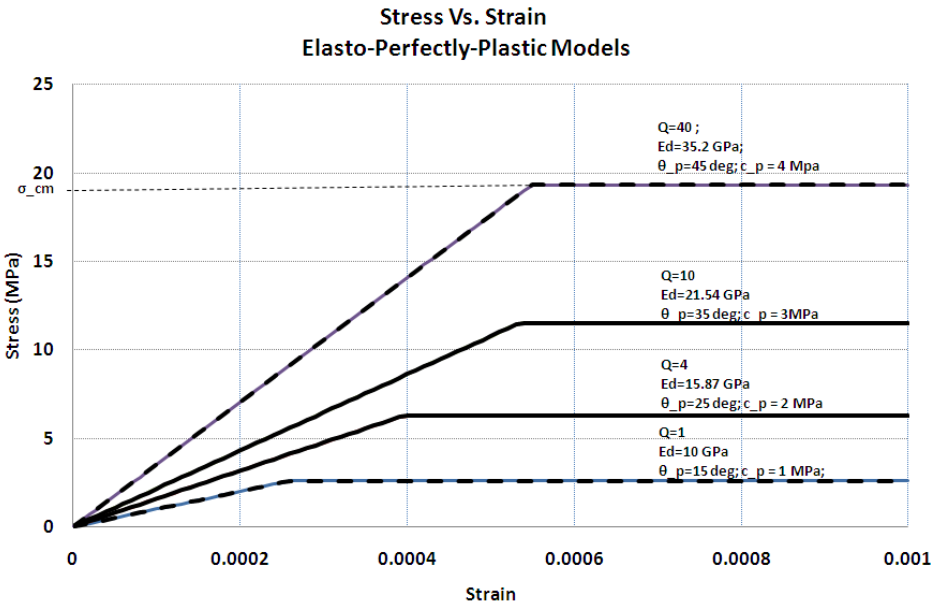

FIGURE 4.7: Stress-strain plot for four rock classes exhibiting elastic-perfectly-plastic behavior for confining stress equal to zero. The peak stress at failure point is equal to the uniaxial compressive strength of the rock mass (σ_{cm}).

Chapter 5

Numerical Modeling in Phase^2

The finite element modeling (FEM) program Phase^2 from Rocscience Inc. is commonly used to design underground excavation support and reinforcement, through modeling rock mass-support interaction. Similarly, the effect of earthquakes on underground structures can be investigated using the pseudo-static seismic analysis procedure incorporated in Phase^2.

Numerical analysis in Phase^2 comprises three main sequential steps: (1) generating a model that represents the problem under study, (2) computing of the model, and (3) interpreting the output from the computation. Following this procedure, first a model of the problem at hand is created and then computation of the model is conducted. Finally, the output of the computation is analyzed using Interpret, a post-processing module for data visualization and interpretation in Phase^2. These procedures are discussed in detail in the following sections.

5.1 Model Generation in *Model Program*

The plane-strain two-dimensional model of a circular tunnel excavated within a rock mass with certain Q is considered. The deformation and strength parameters used to simulate different rock mass quality Q are shown in Table 4.3. The main assumption in a plane-strain model is that the tunnel under investigation is infinitely long and displacement is restricted to the 2D plane, which is perpendicular to the tunnel axis (Rocscience Inc., 2001). Thus, in this study, only the deformation of the tunnel in the transverse plane, resulting in ovaling of the circular tunnel, due to earthquake loading is investigated. Such deformations are caused by waves that produce particle motion perpendicular to the tunnel axis, such as by shear waves traveling perpendicular to the tunnel axis (see Fig. 3.1).

The construction of a geomechanical model in Phase^2 starts with specifying the shape and dimension of the tunnel. In all the experiments, the model of a circular tunnel with specified diameter is considered. Since this study is aimed toward understanding the impact of earthquakes on tunnels as a function of rock mass quality Q, dimension of tunnel, and different seismic parameters such as peak ground acceleration, a simple geometry, such as a circular tunnel, is chosen. This minimizes, or if possible eliminates, the geometric effects on the redistribution of stresses. Such geometric effects, if present, could shroud the variation in stress distribution attributed to seismic loading. The effect of geometry on redistribution of stress around the periphery of a tunnel is demonstrated, in Fig. 5.1, using a circular and a rectangular tunnel with

equal cross-section area as an example. For static loading, the mean stress around a circular tunnel is approximately uniform whereas high stress zones develop around the corners of a rectangular tunnel.

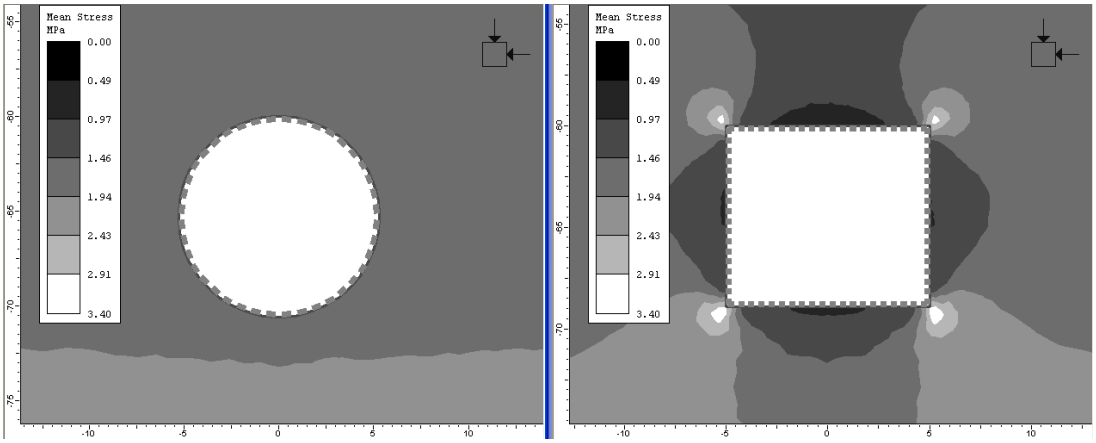

FIGURE 5.1: Difference in stress distribution around a circular and a rectangular tunnel for static loading. It can be seen that zones with higher stress develop around the corners of the rectangular tunnel. Similarly, the total displacement is least around these corners. This example demonstrates the effect of geometry of the tunnel on stress redistribution after excavation of the tunnel.

After the shape and the dimension of the tunnel are specified, the depth of the tunnel is selected based on the purpose of the study. For all the experiments to investigate the influence of rock mass quality, tunnel dimension, and magnitude and direction of seismic coefficient, the depth of the tunnel is fixed at 60-m. This depth was chosen as most of the tunnel lie at an average depth of around 100 m (Dowding, 1979; Bhasin, 2011). Besides, it was found from previous studies (for e.g. Sharma and Judd (1991)) that the effect of earthquakes are larger at shallower depth and therefore placing the tunnel at 60 m could conservatively capture the effect of earthquakes on tunnels.

Then, the external boundary is specified to enclose the tunnel to complete the construction of the model. The choice of external boundary – both in terms of extent and boundary conditions adopted – plays a significant role in numerical modeling and therefore should be selected judiciously. It is a common practice in Phase^2 to specify the external boundary condition using "displacement"; the other option being specifying the "stress" as the boundary conditions.

For this project, the ground level is specified as free surface (stress-free boundary that is free to move in both X and Y directions) , the bottom boundary is fixed (Restrain X and Y), shown by "pin" symbols and the two sides were treated as "rollers" (Restrain X and Free Y). Regarding the extent of the external boundary, it is placed at $\geq 8D$, where D is the maximum dimension of the tunnel. The detailed description about how the boundary conditions and the extent of the external boundary were chosen is included in Appendix A. The distance between the ground surface and the top of the tunnel, however, is equal to the specified depth of the tunnel, which is usually 60 m. An example of the model constructed to represent a circular tunnel is shown in Fig. 5.2; the extent and boundary conditions adopted in the model are also shown.

The parameters specified during meshing and discretization of the model determines the size of the *finite element*, which in turn controls the sensitivity of the model. As a rule of thumb, the finer the mesh, the more accurate the model could become. It must be noted that finer mesh requires larger number of computations while running the model and therefore uses more

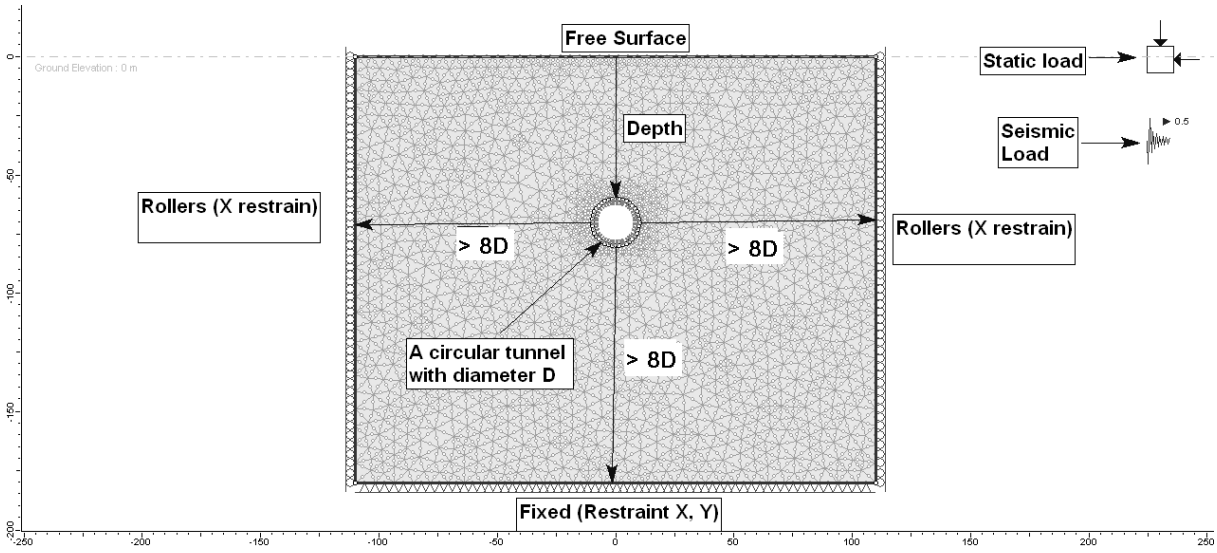

FIGURE 5.2: An example of the model of a circular tunnel, showing the extent and boundary conditions adopted for the external boundary. *D* is the diameter of the tunnel.

computer resources. The mesh and discretization parameters used for this project are shown in Table 5.1.

Mesh type	Graded
Element type	6 Noded triangles
Gradation Factor	0.1
Default number of Nodes on all excavations	75

TABLE 5.1: The parameters used for Mesh and Discretization setup

The options available in Phase^2 for *Mesh Type* are Graded, Uniform, and Radial. *Graded* mesh type is used for this study as it is the commonly used mesh type in numerical modeling (Rocscience Inc., 2001). Similarly, the options in Phase^2 for the element type are 3-Noded Triangle, 6-Noded Triangle, 4-Noded Quadrilateral, and 8-Noded Quadrilateral. From these options, *6-noded triangle* is used as the element type. A 6-noded triangle is a triangular finite element where the stresses and strains are calculated at six points on the triangle – three vertices and the midpoints of the three sides.

The *Gradation Factor* is also an important parameter in numerical modeling as it, together with the Number of excavation nodes, determines the discretization of all the boundaries in the model. The Gradation factor is the ratio of the average length of discretization on excavation boundaries to the length of discretization on the external boundary. For Gradation factor =0.1, the average length of the element on the external boundary is 10 times the length of the element on the excavation boundary (Rocscience Inc., 2001). Figure 5.3 shows the effect of the gradation factor on the mesh in the model of a 3-m diameter circular tunnel with an external boundary that was automatically generated using an expansion factor = 1. The number of finite element increases with increasing gradation factor and the size of the finite element decreases with increasing gradation factor, thereby producing a finer model.

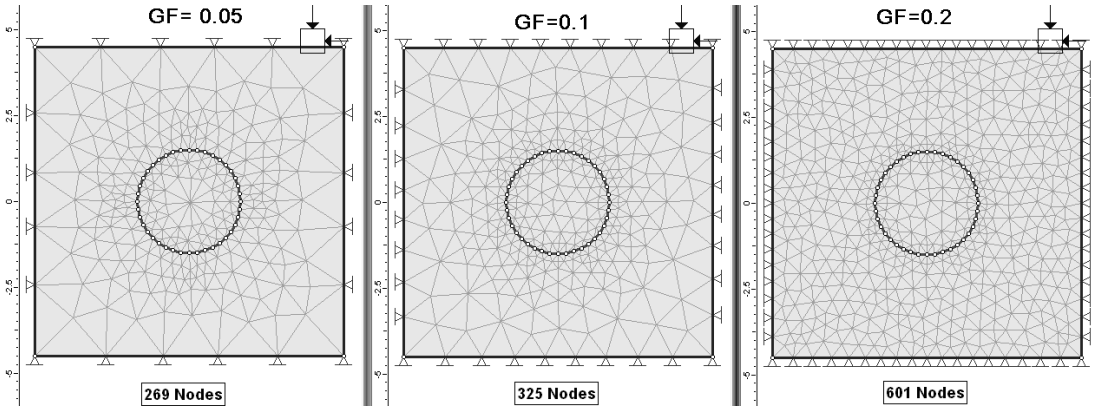

FIGURE 5.3: The effect of Gradation Factor (GF) on the mesh quality is determined by number of nodes in the model. With increasing Gradation Factor, the number of nodes increases and the size of the finite elements decreases, thereby producing a finer model.

Material Properties

After "meshing" the model into finite elements, the material properties are assigned by using the E_{mass} and Mohr-Coulomb parameters, shown in Table 4.3. An example of the material properties dialog is shown in Figure 5.4; the parameters in the three ellipses in the dialog box are varied while assigning different materials to the model. By varying the elastic and strength parameters in the *Material Properties* dialog box, the rock mass modeled can be used to represent different Q values.

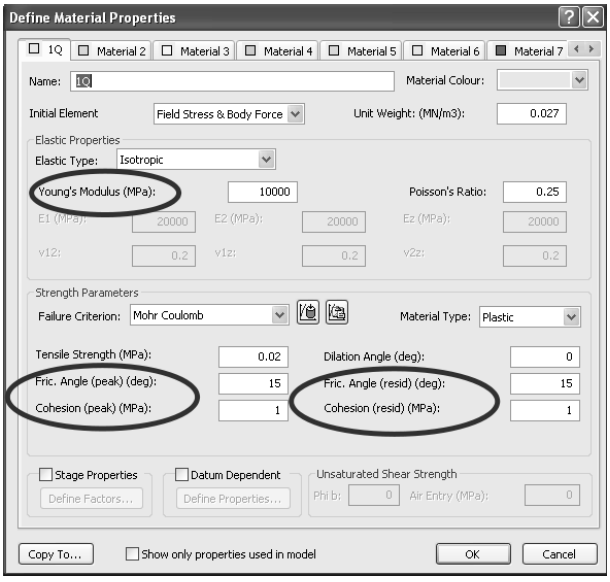

FIGURE 5.4: Material Properties dialog box showing parameters that are varied (shown by red ellipses) to simulate rock masses with different Q-values. The values of rock mass with Q=1 is shown here as an example. Other parameters such as unit weight, Poisson's ratio, tensile strength, and dilation angle are kept constant as the value shown here.

Staging

The main objective of this numerical study is to investigate the effect of earthquakes, or seismic loading, on the installed rock mass-support system. It is assumed in this study that the

support requirement for static loading, mainly to account for the redistribution of stresses after excavation of the tunnel, can be determined as per existing support charts, in this case using Norwegian Q-system chart (Fig. 2.3). The simulated earthquake loading is modeled to occur at a later time after the equilibrium due to static loading has been attained. The primary objective is to determine the increase in axial force on the lining, or the increase in support pressure, due to seismic loading. These phenomena are modeled using a three-stage-model (see Fig. 5.5) in Phase[2] and the description of the three stages are as follows:

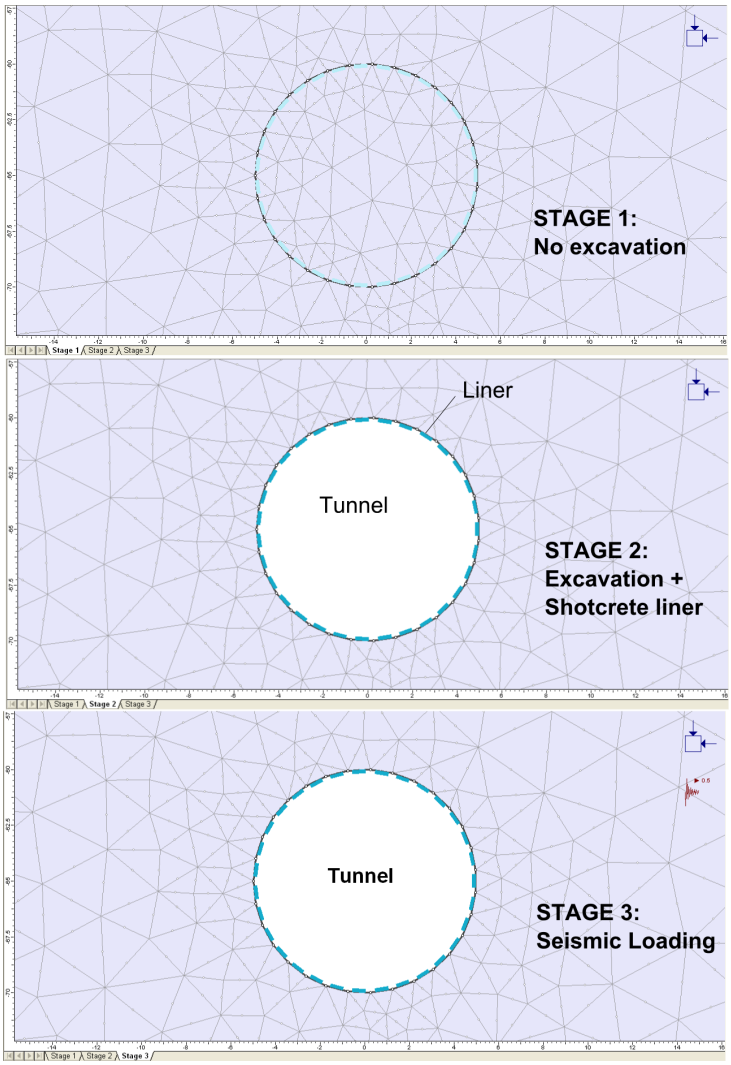

FIGURE 5.5: Three-stage model of a 10-m diameter tunnel. Stage 1 shows the boundary of the unexcavated tunnel, stage 2 represents the tunnel after installation of shotcrete liner, and stage 3 shows seismic loading with horizontal coefficient h=0.5 and v=0.

- *Stage 1:* The model created in this stage shows a subsurface that is at hydrostatic stress, where the vertical stress gradually increases as a function of depth z and unit weight γ = 0.027 MN/m3 such as:

$$\sigma_1 = \gamma\, z$$

For sake of simplicity, hydrostatic condition where the $\sigma_1 = \sigma_3 = \sigma_z$ is assumed, where σ_1 and σ_3 are major and minor principal stress in the 2D plane of the model, and σ_z is

the intermediate out-of-plane stress. The boundary of the tunnel is shown here, but the material within the tunnel boundary is still not excavated yet.

- *Stage 2:* This stage shows the tunnel with the installed support system, in this case a 10-cm thick shotcrete liner. An Equilibrium at this stage represents the redistribution of stresses after the in-situ stress at that depth has been disturbed by the excavation of the tunnel (static loading).

  During tunnel construction, there is always some delay between excavation of the tunnel and installation of the support. Some amount of stress is released before the support is installed such that this portion of the load does not have to borne by the installed support. Therefore, determining the actual magnitude of the load borne by the support system necessitates calculating the amount of stress released during relaxation, or deformation, before the support is installed. The Convergence-Confinement Method (CCM), discussed in Chapter 2, which is an analytical design method for circular tunnels under hydrostatic condition, considers this pre-support relaxation while designing the static support design using CCM. However, as the objective of this study is to investigate the increase in support pressure due to seismic loading (and not necessarily the absolute value of the support pressure), for sake of simplicity of the model, it is assumed that the support system is installed *immediately* after excavation.

  In order to investigate the rock mass-support interaction, a 10-cm thick standard beam liner is placed along the tunnel periphery at this stage; this beam liner simulates a 10-cm thick shotcrete that is applied to support the excavated tunnel. The properties of shotcrete which is modeled during finite element analysis is shown in Table 5.2. The shotcrete liner is formulated as an elastic Timoshenko beam. In addition, the properties of the liner are assumed to remain same throughout all stages, although it is known that the properties of shotcrete change due to hardening of shotcrete at least within the first month after construction (Kontoe et al., 2008).

  The shear force, axial force, and bending moment experienced by the different elements of the liner are analyzed to investigate the effect of seismicity on tunnel support system. The sign convention and the direction of the forces and moment acting on the liner is shown in Fig. 5.6. Note that "axial force" means force along the axis of the liner and not in the axis of the tunnel.

- *Stage 3:* This stage consists of the addition of seismic loading to Stage 2 and simulates the application of seismic loading due to an earthquake at a later time, after the completion of the tunnel. The nature of earthquake loading can be specified using seismic coefficients (described in detail in Chapter 3), which has both horizontal and vertical components. Thus, the magnitude and direction of the seismic coefficient, which in turn depends on the direction of propagation of seismic waves around the tunnel, can be specified to model different earthquake scenarios.

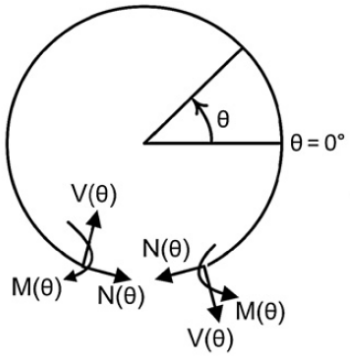

FIGURE 5.6: Cross-section of the tunnel showing the sign convention for the lining forces on the bottom element of the liner. M(θ) - Bending moment; N(θ) - Axial force; V(θ) - Shear force. After Cilingir and Madabhushi (2011a)

Parameters	Value or description
E Modulus (MPa)	15,000
Poisson's ratio	0.2
Thickness (m)	0.10
Material type	Elastic
Liner Type	Beam and formulated as Timoshenko beam

TABLE 5.2: Parameters and descriptions of tunnel liner used

5.2 "Running" the model using *Compute Module*

After building the model, the model is computed to equilibrium using the *Compute* module in Phase^2. During the computation process, the Phase^2 program calculates, among other parameters, the axial force, shear force, bending moment, and displacement for every element in the model, including the liner, which is also modeled by a number of elements of specified length.

The two-dimensional (2D) models are solved using plane strain analysis and Gaussian elimination solver type in Phase2. A maximum iteration of 500, with maximum tolerance of 0.001 using absolute energy as convergence type, was adopted for all the experiments. The model can be "run" directly from the *Modeler Module* or by opening the *Compute* program for processing many files in sequence.

5.3 Data Analysis in *Interpret Module*

After computing the model to equilibrium, the result is analyzed in *Interpreter Module*. This module has numerous built-in parameters that can be displayed by specifying a particular parameter. These parameters, among others, are major principal stress σ_1, intermediate principal stress σ_z, minor principal stress σ_3, and total displacement. There is also an option to create any "user-defined" parameter using the existing parameters by entering a formula to combine different parameters. An example of the result depicting the mean stress, for the three stages, around a 20-m tunnel at 60 m depth is shown in Figure 5.7.

In addition to the above parameters, when a shotcrete liner is modeled, the axial force, shear force, and bending moment on every element of the liner can be extracted in this module. In this

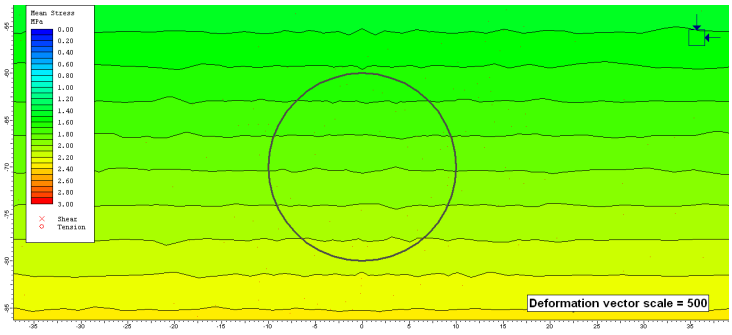

(a) Stage 1: Consolidation under self weight.

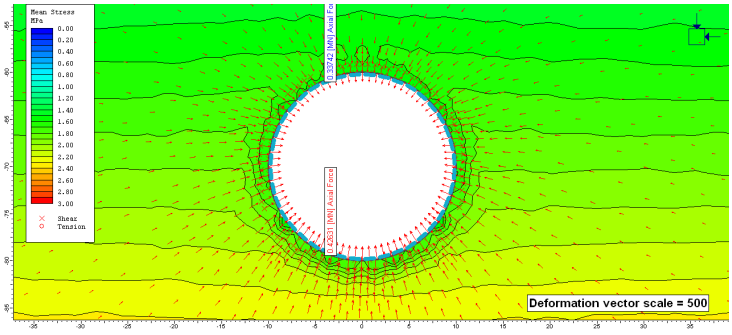

(b) Stage 2: Static condition.

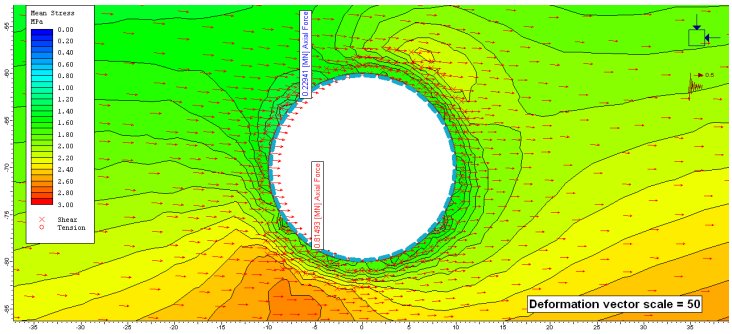

(c) Stage 3: Static condtion + Seismic loading

FIGURE 5.7: Mean stress contour plots for stages 1 to 3. Stage 1 shows the hydrostatic condition before excavation of the tunnel; Stage 2 shows redistribution of stress after excavation of the tunnel; and Stage 3 is after seismic loading (K_h=0.5; K_v=0.0). The red arrows show deformation vectors; the scale of the deformation vectors are different for stages 2 and 3 and, in general, the total displacement in stage 3 is about 10 times larger than in stage 2. Similarly, the mean stress increases in stage 3 at the 2'O clock and 8'O clock mark on tunnel.

study, the values for these three parameters are extracted for all three stages in the model and the difference in the magnitude of any parameter – axial force, bending moment, or shear force – at stage 2 and stage 3 is attributed to the additional load due to the applied seismic loading. In Figure 5.7, the maximum axial force on the lining (MAFL) increases from 0.4 MN during static loading in Stage 2 to 0.8 MN in Stage 3. The difference between the magnitude of the parameters, for example axial force, at Stage 2 and Stage 3 is called the *Seismic Axial Force*, which is described in detail in the following section.

5.4 Seismic Axial Force on the Lining

The data analysis to investigate the impact of seismic loading on a liner – in terms of change in axial force, bending moment, or shear force – is conducted by following the procedures described below. Only the axial force is described here as an example although the same procedure can be followed to obtain the *seismic bending moment* and *seismic shear force*.

The effect of earthquake loading on the tunnel can be analyzed by taking the difference between the axial force during seismic loading (Stage 3) and the axial force at the same location during static loading (Stage 2). This difference in axial force on the lining, referred to as *Seismic Axial Force*, can be attributed to the effect of seismic loading during earthquakes and can be used as a parameter to represent the effect of earthquakes.

As the magnitude of the axial force has a periodic nature around the tunnel for both static and seismic loading, their difference – the seismic axial force – also turns out to be periodic. The seismic axial force can be either negative or positive. When it is positive, it shows that the axial force on the lining has increased during earthquake loading indicating compression. On the other hand, when the seismic axial force is negative, it shows that the earthquake caused tension around the liner and therefore the axial force has been reduced. The maximum value of the seismic axial force, which shows the maximum increase in axial force due to that particular seismic loading, is used as a parameter to compare different tests. The maximum value in both positive (compression) and negative (tension) are used for comparison. The maximum value of the seismic axial force is called the *Maximum Seismic Axial Force*.

As an example, the steps to calculate the *Maximum Seismic Axial Force* for a 10-m diameter tunnel at 60 m depth in rock mass with Q = 1 are shown below. Quasi-static seismic loading with seismic coefficients $K_h = 0.2; K_v = 0$ are applied to simulate earthquake loading.

- Fig.5.9(a) shows the axial force on lining for both static and seismic loading for elastic model. Similarly, the axial force on lining for elastic-perfectly-plastic model for the same tunnel geometry and rock mass quality is shown in Fig.5.9(b). The convention used to assign the angle of a particular point on the tunnel periphery is shown in Figure 5.8. It can be observed that the variation of axial force along the tunnel circumference is periodic with two peaks, located opposite to each other, and two troughs with the same characteristics. This results in an *elliptical* stress distribution around the tunnel periphery, which is more pronounced for seismic loading, around the tunnel, where the location of maximum and minimum stress are approximately perpendicular to each other (for e.g. Stage 3 in Fig. 5.7).

- The seismic axial force is obtained by subtracting the axial force for static loading from the axial force for seismic loading. Fig. 5.9(a) shows the axial force on the lining for static and seismic loading for elastic model and the equivalent plot for elastic-perfectly-plastic model is shown in Fig. 5.9(b). The seismic axial force for both elastic and elastic-perfectly-plastic models are shown in Fig. 5.9(c).

- The maximum value of the seismic axial force is designated as the *maximum seismic axial force* and is the parameter that is used to compare different seismic loading scenarios. The location at which the maximum seismic axial force occurs, which shows the point where

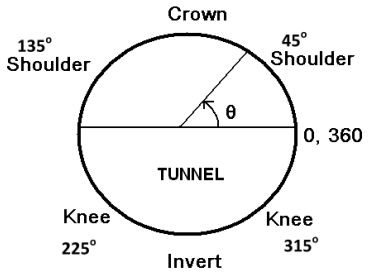

FIGURE 5.8: Sketch showing the convention of the angle used describe a particular location along the tunnel periphery.

the failure due to seismic loading is likely to occur, can be obtained from the same plot. In the example shown in Fig. 5.9(c), the maximum seismic axial force occurs at around 40° - 50°. Fig. 5.9(d) shows the seismic axial force, expressed in terms of % of the static axial force at the same location.

It is assumed in this study that tunnel support required for static loading, which is primarily to due to redistribution of stresses around the tunnel after excavation, is already determined from the existing static support chart. This support design chart, shown in Fig. 2.3 is one of the main components of the Norwegian Method of Tunneling and Q-system. Thus, the increase in axial force, bending moment, and shear force due to seismic loading, which indicates the increase in rock support pressure is calculated in this study. The knowledge of the dependence of increase in axial force, bending moment, and shear force on the lining on other parameters such as rock mass quality Q, dimension of the tunnel, and other earthquake parameters, will help in establishing an additional chart that will complement, for seismic areas, the existing support chart for Q-system. A method to determine a new support pressure for seismic regions that accounts for the increase in support pressure, visualized as decrease in Q-value, in presented in Chapter 7.

A case study for Bolu tunnel in Turkey that was damaged during the 1999 Duzce earthquake was analyzed using data and some results from Kontoe et al. (2008). The authors carried out numerical analysis of the Bolu tunnel – using finite element dynamic analysis and displacement-based quasi-static seismic loading– and compared it with observed damage. The photo of the damaged shotcrete liner in one of the tunnels is included in the paper. Using the model used in Kontoe et al. (2008) along with material and liner properties, and peak ground acceleration, numerical modeling was conducted in Phase^2 using the methodology presented in this chapter. The result of this analysis is also included in Chapter 6.1 on page 59.

In addition, two sets of experiments were conducted to determine the influence of rock mass quality and tunnel dimension on the required support pressure under seismic loading. Except for the experiments designed to investigate the influence of tunnel dimension, a 10-m diameter tunnel at 60-m depth was used as a representative model. The results of these experiments are discussed in Chapter 6.

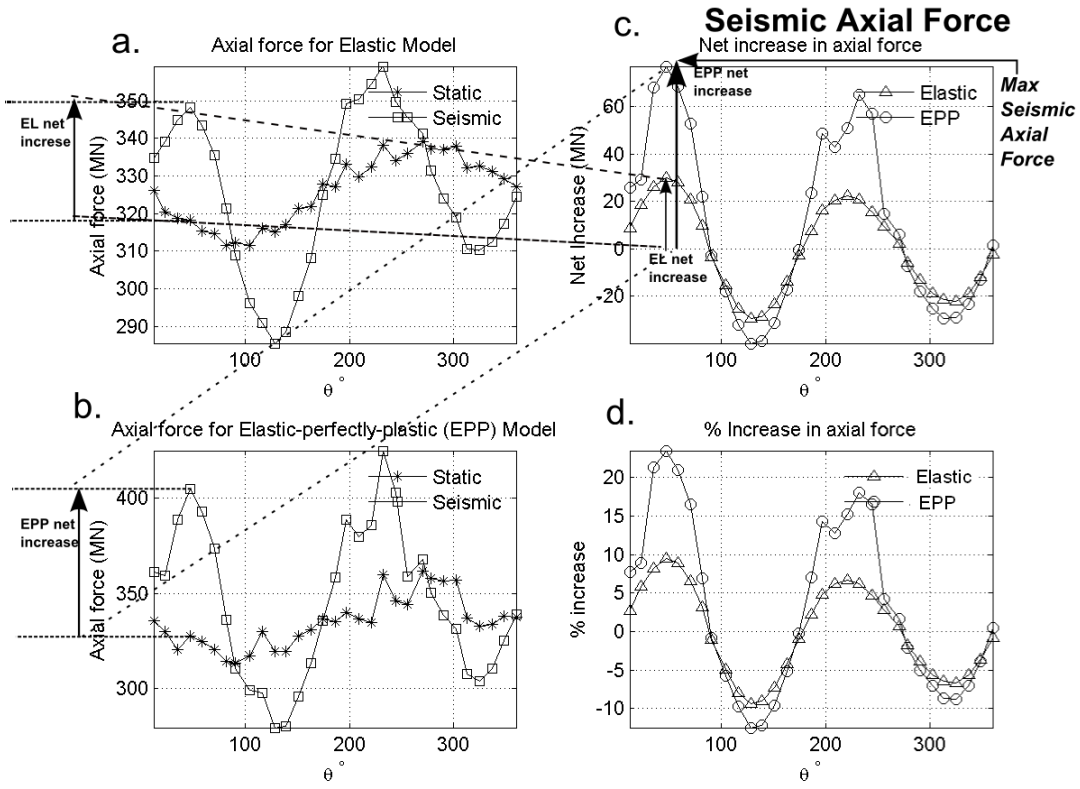

FIGURE 5.9: Variation of axial force on the lining around the circumference of a 10-m diameter tunnel at 60m depth in rock mass with Q=1. Subfigure *a* is the axial force vs. location on tunnel in degrees for elastic model for both static and seismic loading ($K_h = 0.2; K_v = 0$); subfigure *b* shows the axial force for EPP model; subfigure *c* shows the net difference between axial force for seismic and static loading. The maximum seismic axial force occurs at around 40° - 50°; subfigure *d* is same as *c* expressed in % of the axial force for static loading.

Chapter 6

Results

The analyses of the result from the tests, described in Chapter 5, are stated sequentially in the following sections.

6.1 Bolu Tunnel Case Study

In order to perform a *qualitative* comparison between the results from different seismic loading approaches – dynamic, deformation-based pseudo-static, and inertia-based pseudo-static – and observed earthquake damage to tunnels, the damage of Bolu tunnels during the 1999 Duzce Turkey earthquake (Kontoe et al., 2008) is discussed in detail.

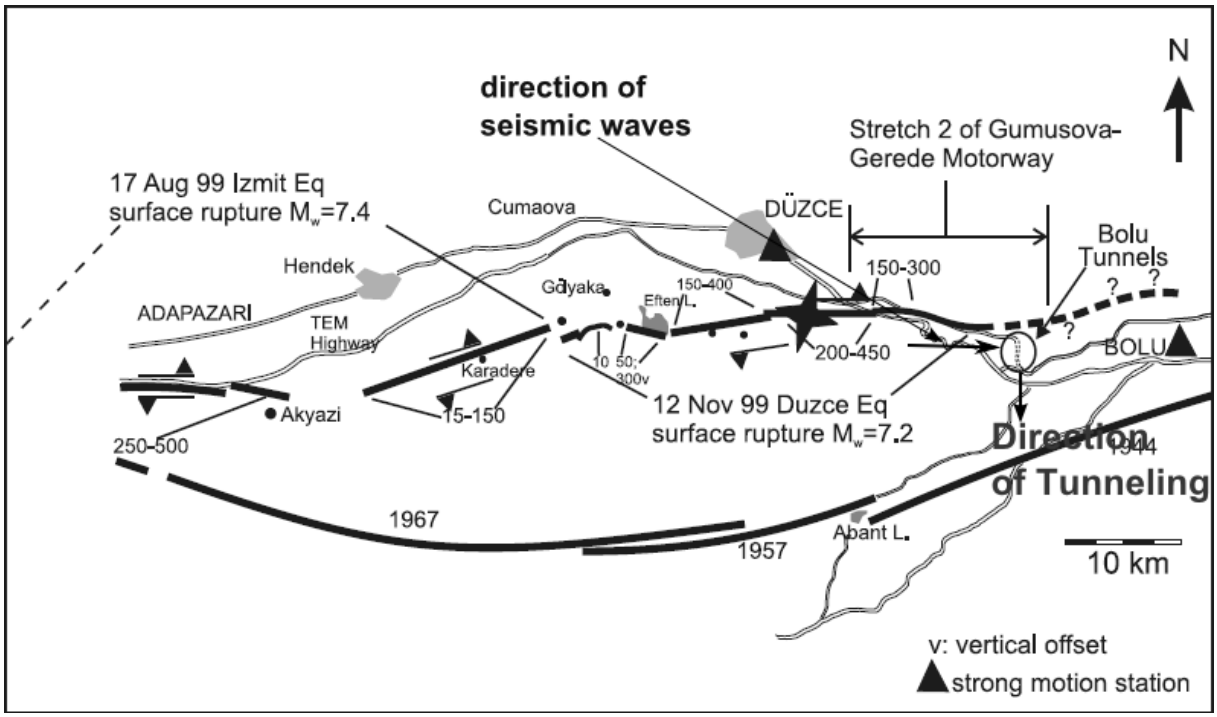

FIGURE 6.1: Map showing the orientation of Bolu Tunnels with respect to expected direction of seismic waves. The direction of tunneling is southward. After Kontoe et al. (2008).

The authors analyzed the damage of Bolu twin tunnels, which were under construction when the earthquake struck. The location of the tunnels and the rupture zone of the earthquake

is shown in Fig. 6.1 on the preceding page. As the tunnels are oriented perpendicular to the rupture zone, the dominant earthquake motion affecting the tunnels is expected to be due to the East-West component; as shown by the arrow on the map, the general direction is perpendicular to the tunnels under study. Furthermore, the southward direction of tunneling is also shown by an arrow on the map.

The design procedure followed for worst ground conditions (see Fig. 6.2) was such that two bench pilot tunnels (BPTs) were first excavated at bench level and then backfilled with reinforced concrete. These reinforced pilot tunnels, which are 5 m diameter tunnels constructed by full-face excavation, provide stiff abutments using which further constructions can be carried out. The earthquake damaged about 30-m stretch on both bench pilot tunnels (BPTs) in poor fault gouge clay. In one case, the BPTs were not backfilled when the earthquake struck and was merely supported by 30 cm thick shotcrete and HEB 100 steel ribs with 1.1 m longitudinal spacing. Re-excavation of this section after the earthquake revealed the characteristics of earthquake induced damage on tunnels, which can be compared with back-analysis results through numerical modeling.

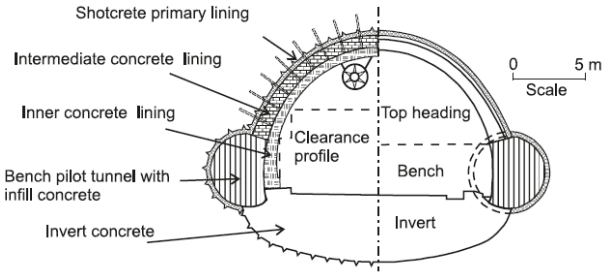

FIGURE 6.2: Design solution for thick zones of fault gouge clay. After Menkiti et al.,2001, cited in Kontoe et al. (2008)

The authors investigated a section, comprising of fault gouge clay, in the 5 m diameter left bench pilot tunnel (LPBT), where the tunnel lining was partially damaged. The observed damage was then compared with results from numerical modeling using 2D non-linear dynamic analysis and deformation-based quasi-static seismic loading. In addition, a photo of the damaged section of the tunnel (see Fig. 6.6) is also present in the same paper. Thus, this gives an opportunity to compare the inertia-based pseudo-static seismic loading with other numerical modeling methods and observed damage.

Their 2D model, consisting of two 5 m diameter tunnels at a depth of about 160 m, is replicated in Phase^2 as shown in Fig. 6.3. The material surrounding the tunnel is poor quality fault gouge clay. Elastic-perfectly-plastic model is chosen and properties of the fault gouge clay and shotcrete liner are shown in Table 6.1 on the facing page. The modeling procedures described in Chapter 5 are followed to model the two pilot tunnels.

The general orientation of Bolu twin tunnels is in North-South direction, and the direction of tunnel construction is southward. Thus, the 2D plane model is also considered to be south facing. Since the rupture zone of the earthquake is located to the West of the tunnel, the expected direction of seismic waves is from West to East. The East-West component of the ground motion, which is responsible for shear deformation of the transverse cross section of the tunnel, was employed for dynamic analysis conducted by Kontoe et al. (2008). The peak ground acceleration obtained from the same accelerogram is 0.57g and, using a reduction factor of 0.7, the

Fault gouge clay properties			Liner Properties	
Peak internal friction angle (°)	20		Young's Modulus (GPa)	5
Peak cohesion (MPa)	0.1		Thickness (cm)	30
Young's Modulus (MPa)	2000		Poisson's ratio	0.2
Unit weight(MN/m3)	0.027		Type	Elastic

TABLE 6.1: Properties of fault gouge clay and shotcrete liner used to model the damage of LBPT tunnel. (Kontoe et al., 2008). The properties of one-day old shotcrete is used as the tunnel was damaged by earthquake right after construction. Kontoe et al. (2008) reported the shear modulus of fault gouge clay and the Young's modulus was calculated using $E = 2G(1 + \nu)$ under Poisson's solid assumption (Stein and Wysession, 2003).

expected peak ground acceleration at tunnel depth is $0.57 \times 0.7 \approx 0.40$g. Thus, the horizontal seismic coefficient equal to -0.4 is added as to simulate earthquake loading. The negative sign here shows that the additional inertial force is acting from West to East, in the direction away from the rupture zone (see Fig. 6.1 on page 59 for probable direction of seismic waves).

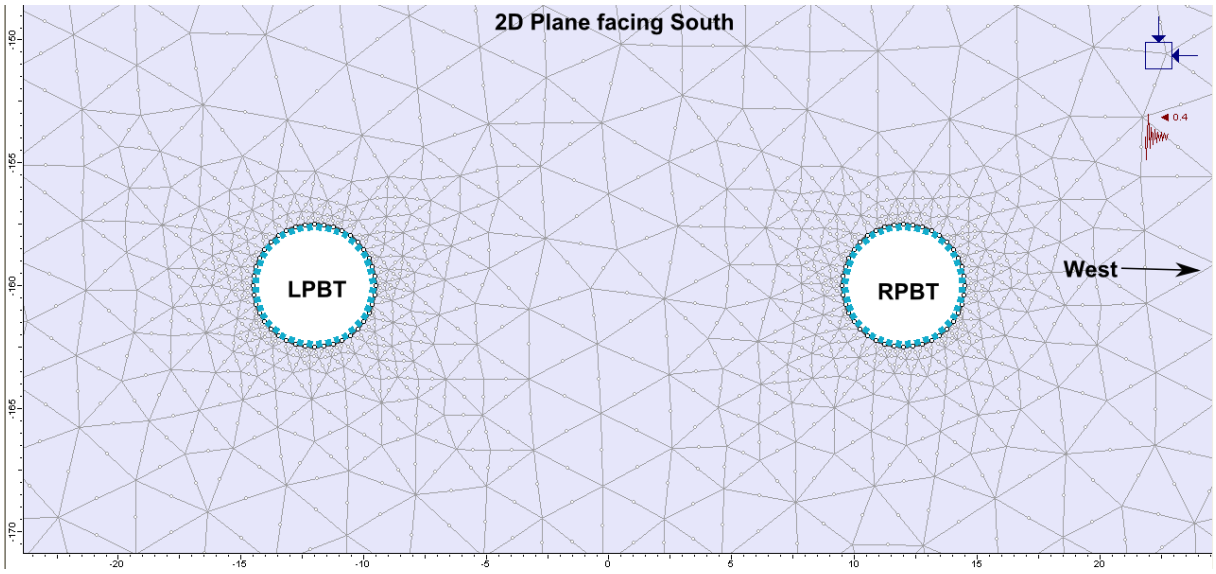

FIGURE 6.3: Model of two pilot bench tunnels. The rupture zone is located to the West of the tunnels.

The result of finite element modeling after pseudo-static seismic loading in Phase^2 is shown in Fig. 6.4 on the following page. The distribution of major principal stress σ_1 is shown in this figure. As noted in Kontoe et al. (2008), the "elliptical-deformed shape" is also observed around both tunnels. It has been discussed in Chapter 3 on page 19 that the alignment of this elliptical shape depends on the direction of the seismic coefficient. For both tunnels, the zone of higher stress is located at the shoulder and knee of the tunnel.

The variation of axial force around the LPBT tunnel, computed using Phase^2, is plotted together with results for dynamic analysis and deformation-based pseudo-static loading from Kontoe et al. (2008) in Fig. 6.5 on page 63. The results from Kontoe et al. (2008) include the axial force (referred to as thrust) around the lining calculated using finite element dynamic analysis and the displacement-based quasi-static loading. Thus, preliminary and qualitative comparisons were made between the results of the inertia-based pseudo-static seismic loading in Phase^2, and dynamic analysis and displacement-based quasi-static approach reported in Kontoe et al. (2008). The comparison is only qualitative and visual as there are several uncertainties

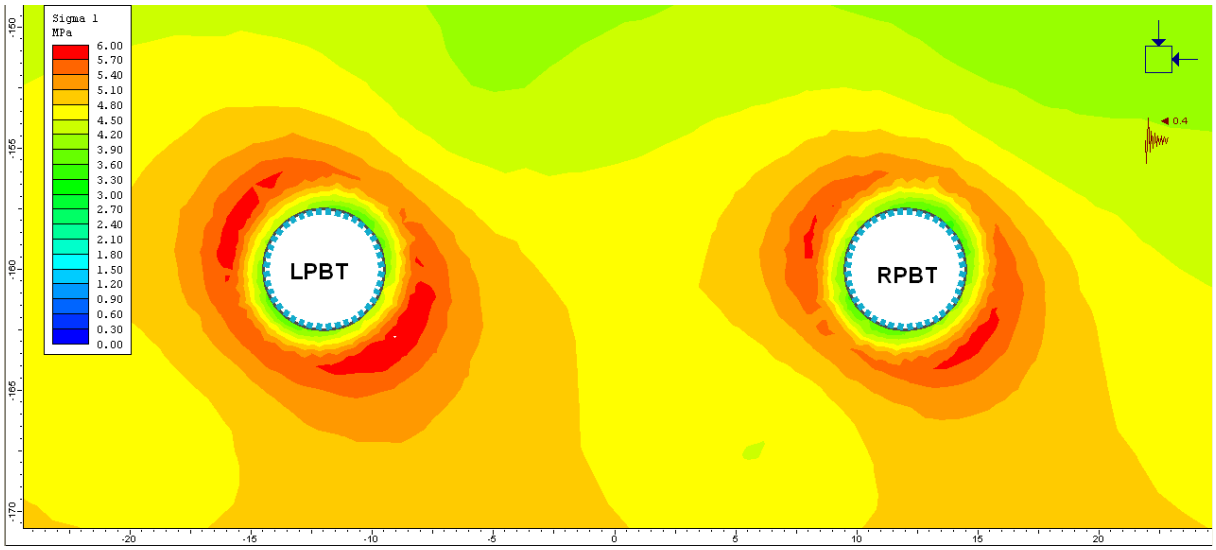

FIGURE 6.4: Distribution of major principal stress around the two tunnels. It may be inferred that the stresses are higher at the shoulder and the knee of the tunnels. Only the horizontal seismic coefficient is applied assuming that the seismic waves propagating in horizontal direction at the tunnel.

inherent in the process. Probably, depending on the way different Finite Element programs are formulated, even the unit for Thrust or axial force is different for Phase^2 and the Imperial College finite element program, used in Kontoe et al. (2008). The axial force for Phase^2 is in terms of "kN" and the thrust (axial force) is in terms of "kN/m". Therefore, *quantitative* comparison of absolute magnitude of the axial forces from the two programs seems infeasible.

Therefore, it was found that the magnitude of the axial force on the lining is different for all three approaches. This could be caused by difference in assumptions used during modeling. For instance, during implementation in Phase^2, the liner properties were not changed and only one type of material, fault gouge clay, was used for simplicity. In addition, a different material model, namely kinematic hardening model (M2-SKH), was used by Kontoe et al. (2008), whereas the simple elastic-perfectly-plastic model is implemented in Phase^2.

Nonetheless, the location of the two maxima of axial force around the lining coincides for all three approaches. For LPBT, the two maxima occurs at the shoulder (137°) and the knee (317°) of the tunnel for all three approaches. What is more interesting is that the location of the two maxima of axial force around the tunnel falls approximately at the same location as where the damage to shotcrete liner was observed at the LPBT. This is clearly shown in Fig. 6.6 on page 64. It can be inferred from this finding that, although it requires more such case studies to substantiate it, the pseudo-static seismic loading method presented herein has the ability to capture some essence of the complicated tunnel-earthquake interaction that has the potential to damage tunnels.

6.2 Influence of Rock mass quality Q

In order to investigate the effect of rock mass quality Q on the characteristics of the axial force, bending moment, and shear force on the lining during seismic loading, a 10-m diameter circular tunnel is placed at a depth of 60 m. A fixed seismic loading with seismic coefficients $K_h = 0.30$ and $K_v = -0.15$ is chosen to investigate the effect of seismic loading. While keeping the depth,

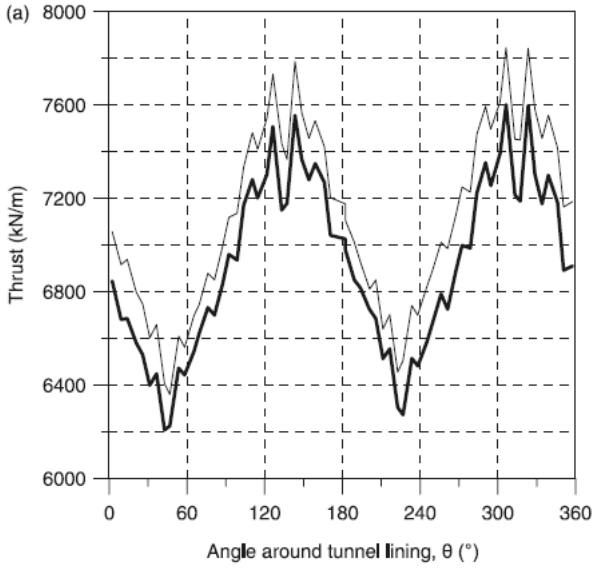

(a) Axial Force - Dynamic Analysis. After Kontoe et al. (2008)

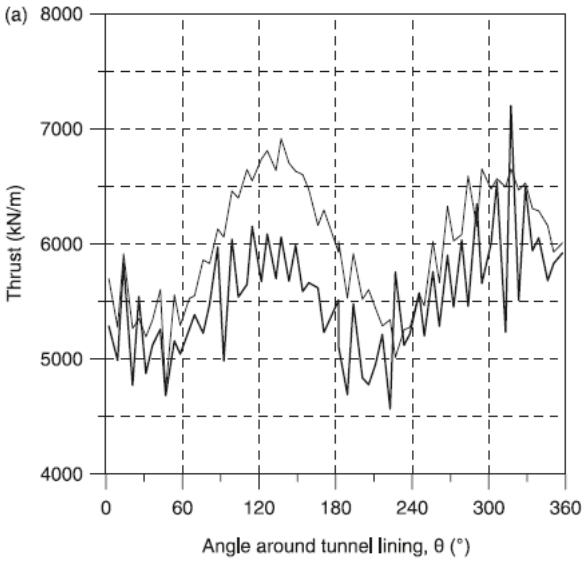

(b) Axial Force – Quasi-static (displacement-based) loading. After (Kontoe et al., 2008)

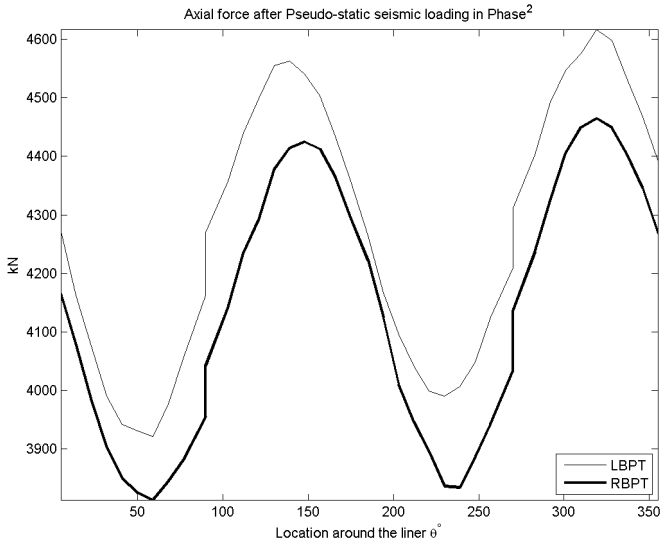

(c) Axial Force - Pseudo-static loading (Inertia based in Phase^2)

FIGURE 6.5: Comparison of axial force plots for three seismic loading approaches. The magnitude of the axial force is different for all three cases. However, the location – shoulder and knee of the tunnel – at which the two maxima of the axial force occurs approximately falls at the same location for all three cases. The legend of (a) and (b) are same as (c).

tunnel dimension and seismic loading constant, several tests were conducted by varying the rock mass quality of the surrounding rock mass around the tunnel. The four rock classes shown in Table 4.1 were simulated using the parameters described in Table 4.3. Both elastic and elastic-perfectly-plastic (EPP) models were analyzed for comparison.

Fig. 6.7 shows the distribution of major principal stress σ_1 around a 10-m tunnel excavated in rock masses with Q ranging from 1 to 40 for elastic-perfectly-plastic models. It may be noted that "yielded" points, shown by 'x' marks around the tunnels, occurs only for the tunnel in Q=1 as at 60 m depth. This occurs because the in-situ stress at this depth is just enough to surpass the

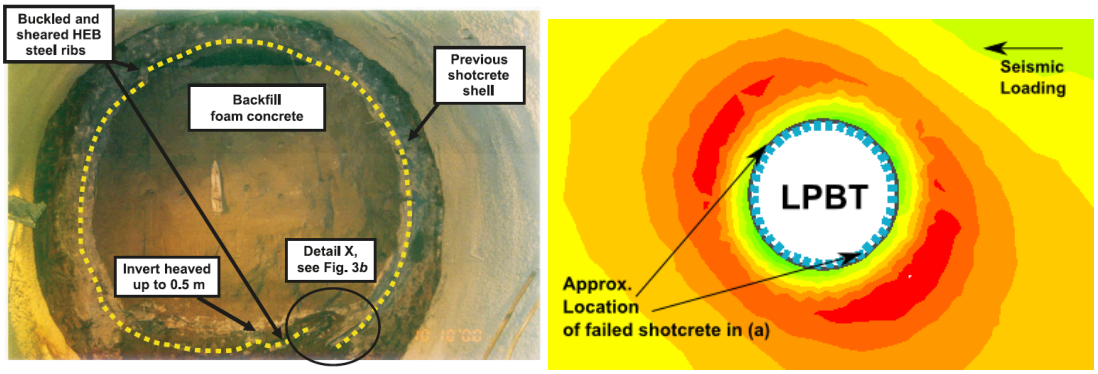

(a) View of damaged 5-m diameter tunnel. After Kontoe et al. (2008)

(b) Result of Phase^2 showing distribution of major principal stress σ_1. The color scale is same as Fig. 6.4

FIGURE 6.6: Comparison of actual damage (a) and result from Phase^2 (b) for Bolu tunnel. The location of the actual damaged section of the shotcrete lining coincides with the two zones of high stress in the result from Phase^2. Note: It is assumed here that the photo in (a) is taken facing southward, in the direction of tunnel advancement.

elastic limit of the rock mass with Q=1 and therefore other rock masses with $Q \geq 4$ behave like elastic materials. This elastic limit is determined by the peak strength parameters and in-situ stress as shown in Equation 6.1 (Oreste, 2009).

$$P_{cr} = P_0(1 - \sin\phi_p) - c_p \cos\phi_p \tag{6.1}$$

where P_{cr} is the critical pressure, P_0 is lithostatic in-situ stress, c_p is peak cohesive strength and ϕ_p is peak angle of internal friction. The elastic limit, or yield point, of the rock mass is reached when $P_{cr} = 0$ and the rock mass behaves as plastic material when $P_{cr} > 0$. Using Eqn. 6.1, the depth at which the four rock classes with Q = 1 -40 starts to behave as elastic-plastic materials can be determined. For given ϕ_p and c_p, depending on the rock class, the value of P_0 above which P_r remains positive is:

$$P_0 = \frac{c_p \cos\phi_p}{1 - \sin\phi_p} \tag{6.2}$$

Using this equation, the *critical* depths beyond which rock masses with Q from 1 to 40 behave as elastic-plastic materials, calculated using ϕ_p and c_p for different rock classes shown in Table 4.3 and assuming $\gamma = 0.027MN/m^3$, are shown in Table 6.2.

Rock mass class	Q value	P_0 (MPa)	*Critical* Depth (m)
Very poor	1	1.3	48
Poor	4	3.1	116
Good	10	5.8	213
Very Good	40	9.7	358

TABLE 6.2: The depth beyond which the four rock classes behave as elastic-plastic materials calculated using Eqn. 6.2 and parameters from Table 4.3, and assuming $\gamma = 0.027MN/m^3$

It is apparent that the yielded zone around the tunnel in rock mass with Q=1 has lowered (released) the stress in the surrounding rock mass and thus the stress accumulation around the tunnel is higher to rock masses with $Q \geq 4$ than for the rock mass with Q=1. For the static

condition, the high stress zone lies around the invert of the tunnel ($\sim 270°$). On application of seismic loading, with seismic coefficients $K_h = 0.30; K_v = -0.15$, the region of higher stress shifts toward the knee (225°) of the tunnel and another high stress zone develops on the opposite side at the shoulder of the tunnel (45°), resulting two 'ear-like' ellipsoid high stress zones around the tunnel.

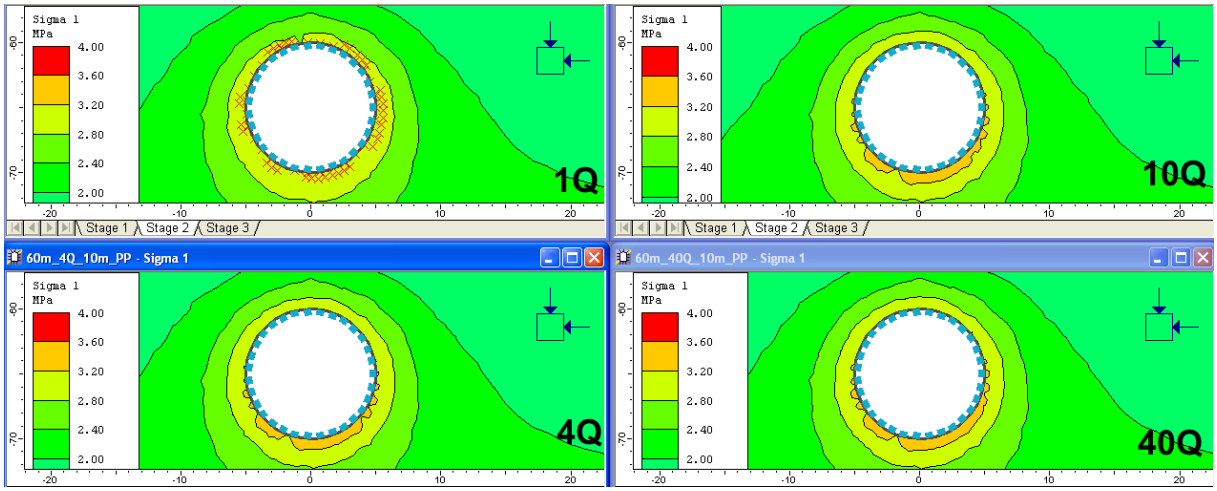

(a) Stage 2 - Static loading

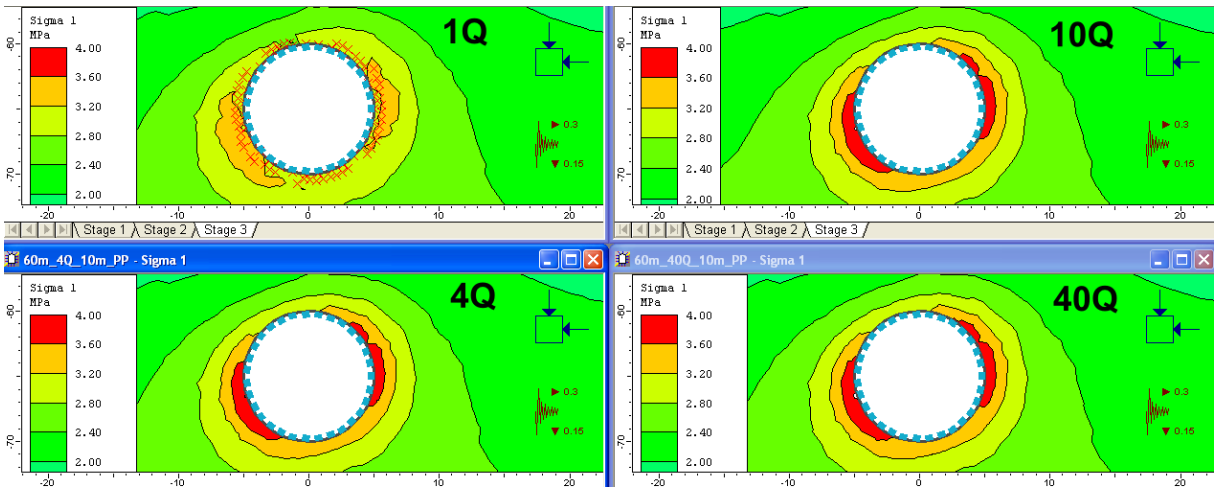

(b) Stage 3 - Static + Seismic ($K_h = 0.30; K_v = 0.15$) loading

FIGURE 6.7: Contour plot of major principal stress σ_1 around a 10-m diameter tunnel excavated in rock masses with Q ranging from 1 to 40. At this 60m depth, only rock mass with Q=1 have surpassed its elastic limit and therefore yielded points, shown by 'x' marks around the tunnel, occurs only around the tunnel in rock mass with Q=1.

The variation of the axial force, bending moment, and shear force on the lining for both static and seismic conditions are described as follows:

6.2.1 Axial Force

The axial force vs. location in degrees around the tunnel for the four rock classes for elastic and elastic-perfectly-plastic models are shown in Fig. 6.8. For both models, the axial force on the lining increases with seismic loading. The variation of the axial force around the tunnel has

some periodicity. For static loading, there is one maxima, indicating compression, around the invert of the tunnel and one minima, indicating tension, near the roof of the tunnel. For seismic loading, however, the trend of the axial force around the tunnel has two peaks and two troughs. The location of the peaks and troughs around the tunnel for seismic loading depends on the direction of the seismic load.

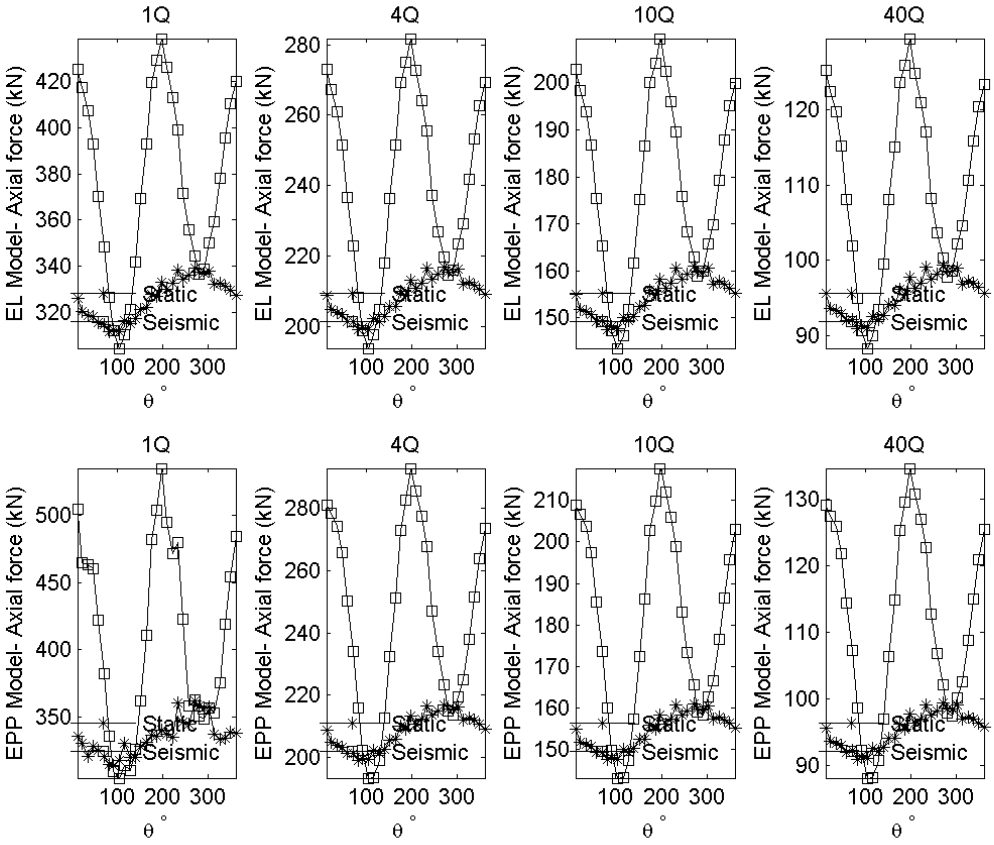

FIGURE 6.8: Axial force on the lining as function of location the tunnel in degrees for both seismic and static loading. The top row shows axial force for different Q using elastic model and the bottom row shows the same for elastic-perfectly-plastic model.

In general, the magnitude of the axial force is greater for elastic-perfectly-plastic model than for elastic models. In addition, with increasing Q value, the axial force on the lining decreases. This phenomenon is demonstrated using the mean value of the axial force for static and seismic loading for both elastic and EPP models (see Fig. 6.9).

For a particular depth, it is observed that the axial force on lining, for both static and seismic loading, for elastic and elastic-perfectly-plastic models overlap for good quality rocks ($Q \geq 4$ for 60 m depth). Conversely, for rocks with lower Q (i.e. Q = 1), the magnitude of axial force on the liner deviate for the two models. This is because, within their elastic limit, the rock mass behaves like elastic materials irrespective of the choice of the post-failure characteristics. For 60 m depth, corresponding to 1.62 MPa, the elastic limit for rock masses with Q = 1 is reached whereas rock masses with $Q \geq 4$ are still within their elastic limit (see Table 6.2) and tend to behave elastically. This is evident in Fig. 6.9 where the mean axial force for elastic and elastic-perfectly-plastic models for both seismic and static loading overlap for $Q \geq 4$.

Furthermore, it may be noted that the increase in the mean axial force due to seismic loading is also significantly larger for Q = 1, where the elastic limit has been surpassed resulting in a development of a failed plastic zone around the tunnel. So this observation corroborates previous findings that the "zone that suffers deformation during seismic loading is more or less the zone that has failed during excavation" (Barton, 1984).

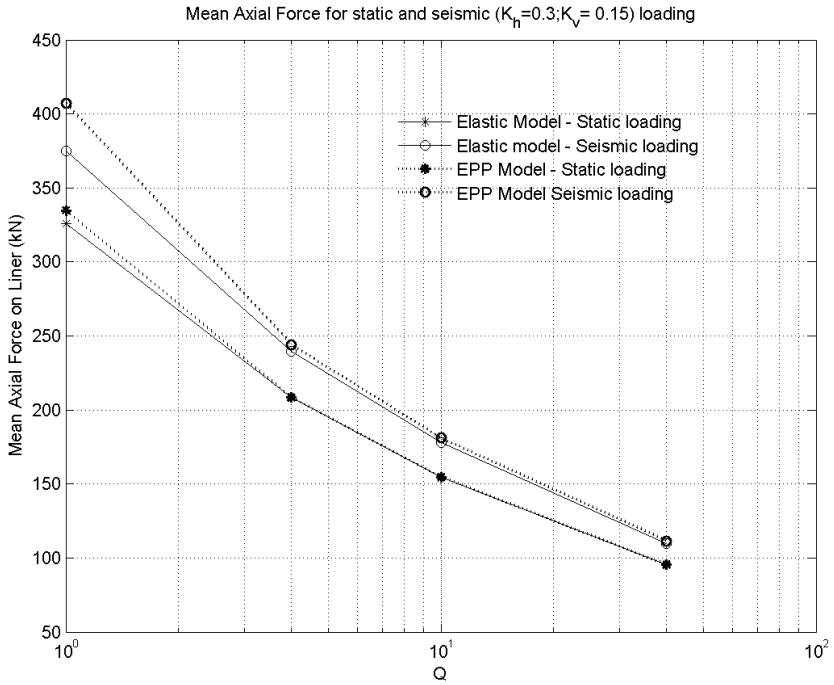

FIGURE 6.9: Mean of the axial force around the tunnel periphery for different rock mass quality. The magnitude of the axial force on the lining (for both seismic ($K_h = 0.30; K_v = -0.15$) and static loading) increases as the rock mass quality Q decreases.

The net increase in axial force, referred to as *seismic axial force*, for every shotcrete liner element around the tunnel is calculated using the procedure shown in Chapter 5 and the result is shown in Subfigs. 1 and 4 in Fig. 6.10. The seismic axial force for both elastic and EPP models have similar trend in variation around the tunnel, except that, for rock mass with Q = 1, the magnitude for elastic-perfectly-plastic model is much larger than for elastic model. The subfigures 2 and 3 in Fig. 6.10 show the maximum positive (compression) seismic axial force, which is the largest increase in axial force around the tunnel. Similarly, the maximum negative seismic axial force for both elastic and elastic-perfectly-plastic models are shown in subfigures 5 and 6 in Fig. 6.10. The % increase with respect to the static axial force at the same point are shown as labels in subfigure 2 and 5. The location, in degrees, of the point on the liner with maximum increase in axial force are also shown as labels in subfigures 3 and 6.

The compressional increase in seismic force (32% for elastic and 37 - 57% for EPP models) is larger than tensional increase ($\leq 5\%$ for both elastic and EPP model). For this seismic loading ($K_h = 0.30; K_v = -0.15$), the maximum compression occurs at the knee of the tunnel at 197° and the maximum tensional increase takes place at the shoulder of the tunnel at 104° - 116°. The data corresponding to Fig. 6.10 are shown in Tables 6.3 and 6.4.

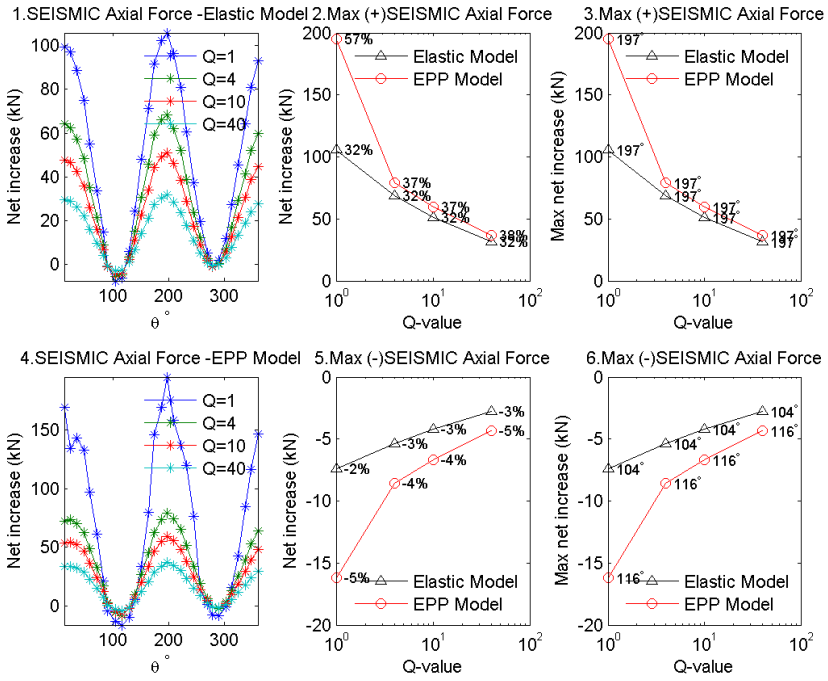

FIGURE 6.10: *Seismic* axial force on the lining as function of location the tunnel in degrees. The seismic coefficients used here are $K_h = 0.30$ and $K_v = -0.15$. The two plots to the right show the maximum seismic axial force on the lining. The (+) plot shows the maximum positive seismic axial force (compression) and the (-) plot shows the maximum negative seismic axial force (tension). The labels on the two plots to the right indicate the % increase in axial force due to seismic loading and location of the maximum value around the tunnel, respectively.

	Q=1	**4**	**10**	**40**
Max.(+)	106	68.4	51.1	31.7
%	32	32	32	32
$\theta_+(^\circ)$	197	197	197	197
Max.(-)	-7.39	-5.39	-4.23	-2.77
%	-2	-3	-3	-3
$\theta_-(^\circ)$	104	104	104	104

TABLE 6.3: Maximum seismic axial force (kN) on the lining for elastic model.

	Q=1	**4**	**10**	**40**
Max.(+)	195	79.5	59.3	36.8
%	57	37	37	38
$\theta_+(^\circ)$	197	197	197	197
Max.(-)	-16.2	-8.54	-6.67	-4.34
%	-5	-4	-4	-5
$\theta_-(^\circ)$	116	116	116	116

TABLE 6.4: Maximum seismic axial force (kN) on the lining for elastic-perfectly-plastic model.

6.2.2 Bending Moment

The variation of the bending moment on the liner for elastic and elastic-perfectly-plastic (EPP) models for rock masses with Q ranging from 1 to 40 are shown in Fig. 6.11. The nature of the variation around the tunnel is similar to the variation of the axial force on the lining, with a distinct increase in either positive or negative direction due to seismic loading ($K_h =$

$0.30; K_v = -0.15$). As a function of Q, the bending moment on the lining under seismic loading decreases with increasing rock mass quality. For elastic models, the bending moment increases from around 0.02 kNm for Q=1 to ca. 6×10^{-3} kNm for Q=40.

For rock masses with $Q \geq 4$, the plots for elastic and elastic-perfectly-plastic models are almost equivalent. This happens as, at a depth of 60-m, the rock masses with $Q \geq 4$ are still within their elastic limit, as described in the subsection 6.2.1. On the other hand, rock mass with Q = 1 has crossed its elastic limit and a yielded zone has formed around the tunnel periphery. Thus, an slight increase in magnitude of the maximum bending moment occurs for elastic-perfectly-plastic model (ca. 0.06 kNm) as compared to the elastic model (ca. 0.02 kNm).

The net increase in bending moment due to seismic loading, or referred to as *Seismic Bending Moment*, was calculated using the methodology described in Chapter 5 and the resulting plots are shown in Fig. 6.12. Subfig. 1 shows the net increase in bending moment around the tunnel for different rock masses using the elastic model, and Subplot 4 shows the seismic bending moment for elastic-perfectly-plastic models. It may be noted that the net increase in bending moment for elastic and EPP models are within the same range. For rock mass with Q = 1 using EPP model, the variation of the seismic bending moment around the tunnel periphery is in near random, with significant jumps even between adjacent elements of the liner.

Subfigs. 2 and 3 in Fig. 6.12 show the maximum net increase in positive direction for both elastic and EPP model for the four rock masses. The maximum positive occurs near the shoulder of the tunnel (104° and 116° for elastic and EPP model, respectively). Subfigs. 5 and 6 in Fig. 6.12 show the maximum increase in negative direction. The maximum increase in negative direction occurs around the knee of the tunnel (197°, except for Q=1, which occurs at 35°).

In subfigs 2 and 5, the labels on the plots show the % increase in bending moment during seismic loading with respect to the static bending moment. The % increase shown here is very high and therefore is not meaningful. This unbelievably high values must be due to the very low bending moment under static conditions. The locations of the liner element at which the maximum increase in bending moment occurs are shown as labels in subfigs. 3 and 6. The maximum increase in bending moment during seismic loading occurs around the shoulder or the knee of the tunnel. The data corresponding to these plots are shown in Tables 6.5 and 6.6.

6.2.3 Shear Force

The trend of the shear force on the lining for the same experiments, described in the preceding subsections, are shown in Fig. 6.13. The magnitude of the shear force is about 3 - 4 orders of magnitude smaller than the axial force. For all rock masses, using elastic or elastic-perfectly-plastic models, the difference between shear force for seismic and static conditions are negligible and there is no discernible trend due to either seismic loading, or change in rock mass quality. The extremely small values of shear force (and thus the variation due to seismic loading) is possibly due to the fashion in which the model has been setup – the shotcrete liner was attached to the liner, with no space in between them.

The net increase in shear force on the lining is shown in Fig. 6.14. As was the case with bending moment, the net increase in larger for elastic-perfectly-plastic model with Q = 1, but the trend is near "random" with values fluctuating almost for every adjacent liner elements. Thus,

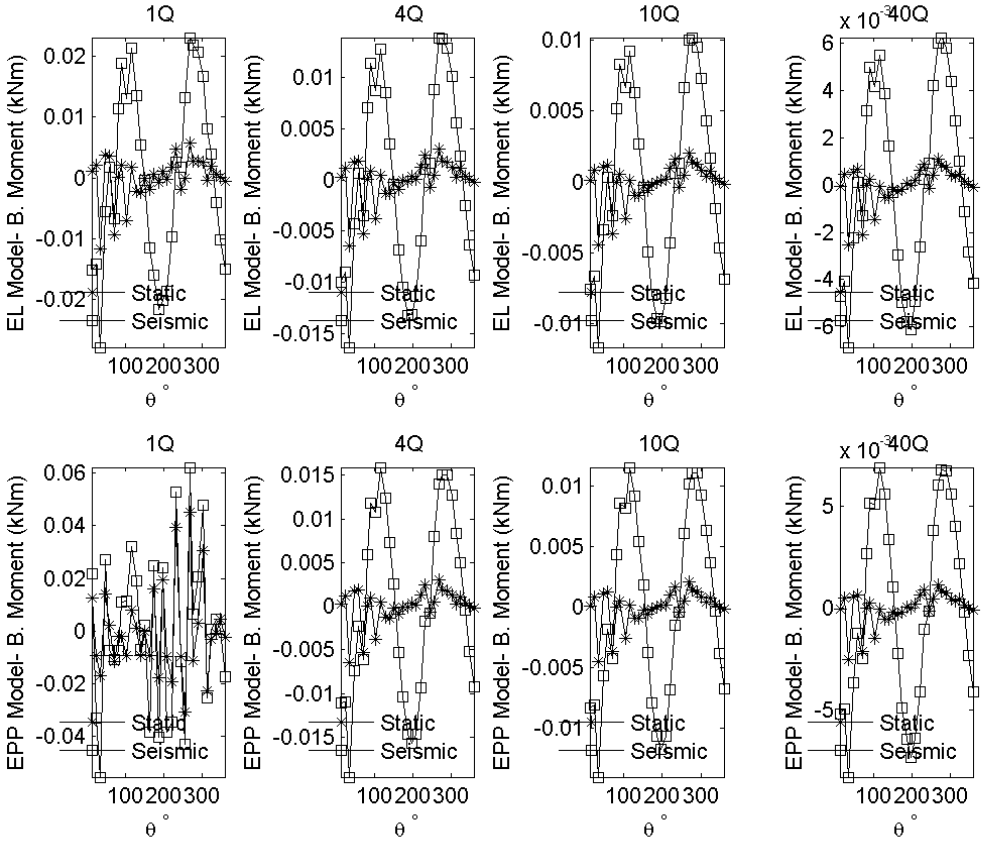

FIGURE 6.11: Bending moment as function of location, in degrees, around the tunnel. The graphs for elastic and elastic perfectly plastic models for rock mass quality ranging from 1 to 40, under static and seismic conditions are shown here. The seismic coefficients used for the seismic loading are $K_h = 0.3$ and $K_v = -0.15$.

	Q=1	**4**	**10**	**40**
Max.(+)	0.02	0.0126	0.00923	0.00564
%	286	330	354	385
$\theta_+(^\circ)$	104	104	104	104
Max.(-)	-0.0212	-0.0135	-0.00994	-0.0061
%	-1.86e+003	-3.88e+003	-7.94e+003	-4.51e+004
$\theta_-(^\circ)$	197	197	197	197

TABLE 6.5: Maximum seismic Bending Moment (kNm) on the lining for elastic model, with maximum net increase, % increase and location on the tunnel.

	Q=1	**4**	**10**	**40**
Max.(+)	0.0239	0.0154	0.0114	0.00694
%	299	3.28e+003	7.73e+003	1.55e+004
$\theta_+(^\circ)$	116	116	116	116
Max.(-)	-0.0387	-0.0161	-0.0119	-0.00729
%	-231	-4.64e+003	-9.5e+003	-5.4e+004
$\theta_-(^\circ)$	35	197	197	197

TABLE 6.6: Maximum seismic Bending Moment (kNm) on the lining for elastic-perfectly-plastic model, with maximum net increase, % increase and location on the tunnel.

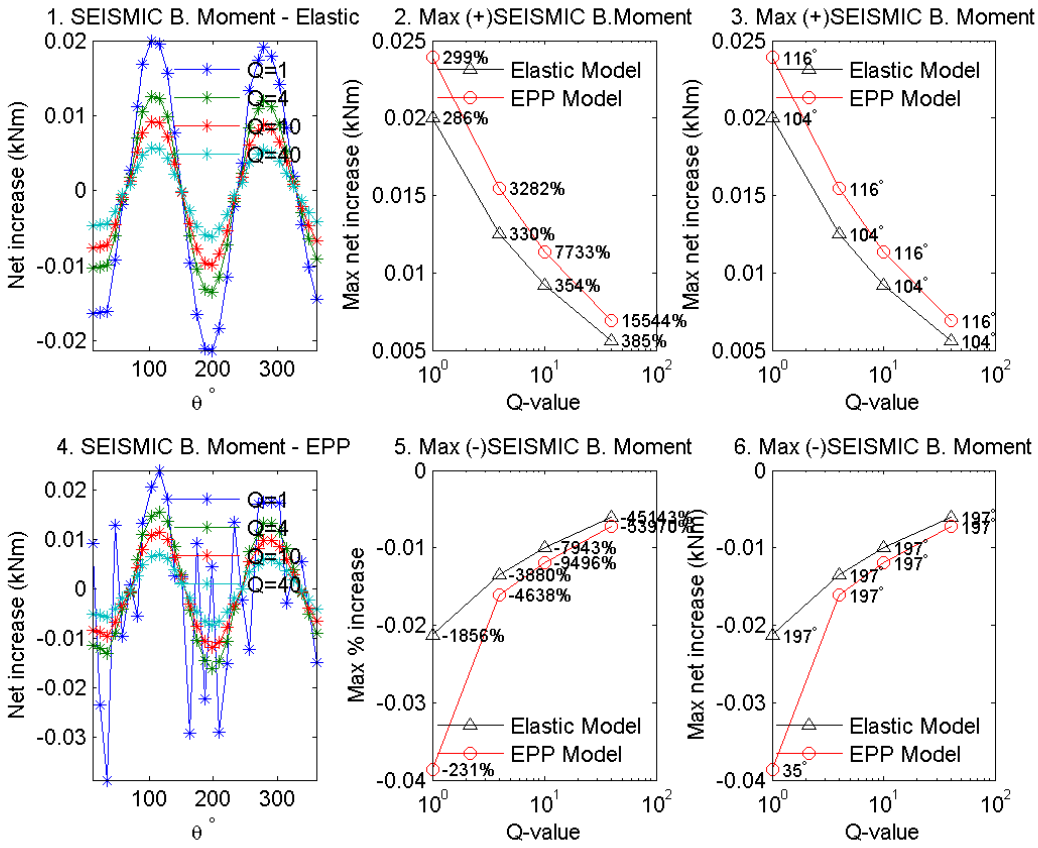

FIGURE 6.12: The seismic bending moment, which is the net increase in bending moment due to seismic loading, in both positive and negative direction, for both elastic and elastic-perfectly-models are shown. The % increase and the location of the maximum increase on the tunnel for all rock masses using elastic and elastic-perfectly-plastic models are also shown.

it appears that the shear force data cannot be used to investigate the effect of seismic loading on the liner. The data used for these plots are shown in Tables 6.7 and 6.8.

6.3 *Proxy* for Support Pressure

The support pressure is an important parameter in designing the support system of a tunnel and empirical relationships, such as Barton et al. (1974) and Bhasin and Grimstad (1996), exists between the rock mass quality Q and the corresponding support pressure for static conditions. During tunnel construction, pressure transducers are installed inside the tunnel liner and the support pressure exerted on the tunnel liner by the surrounding rock mass are thus measured in order to monitor the performance of the installed support system.

During numerical modeling, however, at least using Phase^2, the support pressure cannot be obtained directly as an output of the numerical analysis. The readily available liner-related output parameters are axial force, bending moment, and shear force on the lining. Thus, it is attempted to use one of these parameters, or any form of their combination, as a *proxy* for the support pressure for both static and seismic conditions. In an attempt to select the most appropriate proxy for support pressure, the following procedures, using data from 10-m diameter tunnel

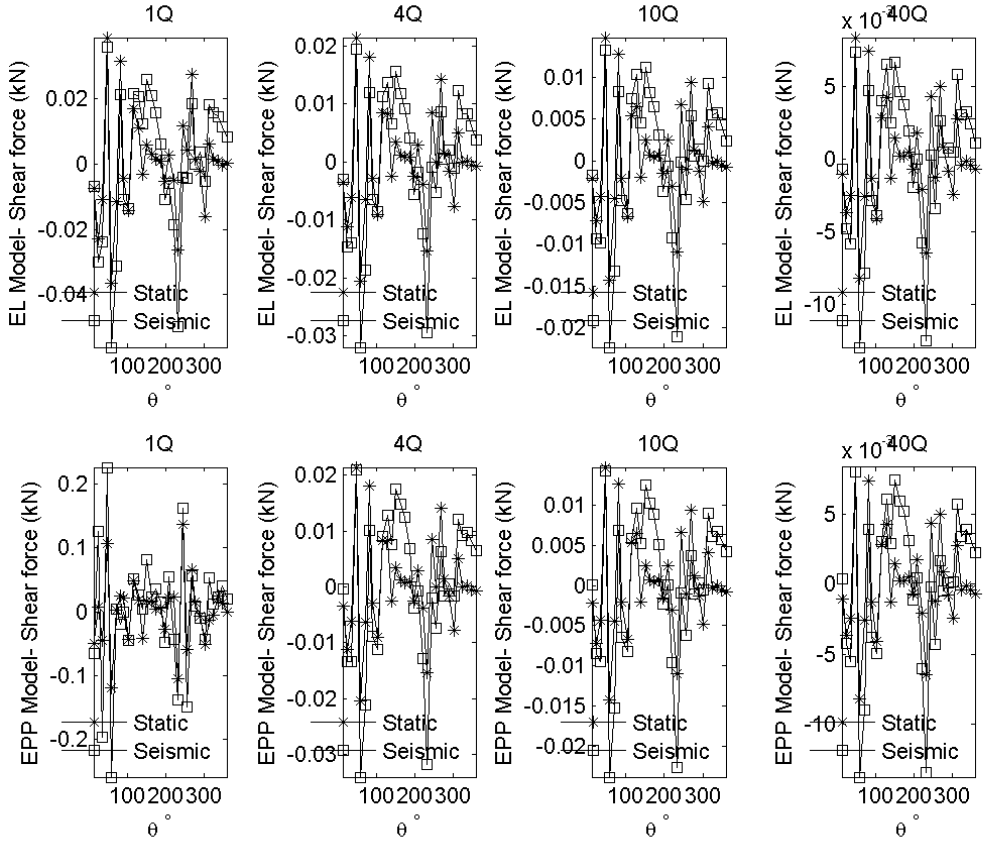

FIGURE 6.13: Shear Force as function of location, in degrees, around the tunnel. The graphs for elastic and elastic perfectly plastic models for rock mass quality ranging from 1 to 40, under static and seismic conditions are shown here. The seismic coefficients used for the seismic loading are $K_h = 0.3$ and $K_v = -0.15$.

	Q=1	**4**	**10**	**40**
Max.(+)	0.0202	0.0121	0.00869	0.00516
%	355	353	353	352
$\theta_+(^\circ)$	151	151	151	151
Max.(-)	-0.0233	-0.014	-0.0101	-0.00601
%	-88	-91	-92	-93
$\theta_-(^\circ)$	232	232	232	232

TABLE 6.7: Maximum seismic shear force (kN) on the lining for elastic model.

	Q=1	**4**	**10**	**40**
Max.(+)	0.119	0.014	0.0101	0.00599
%	1.8e+003	410	409	408
$\theta_+(^\circ)$	23	151	151	151
Max.(-)	-0.152	-0.0163	-0.0118	-0.00701
%	-341	-106	-107	-109
$\theta_-(^\circ)$	35	232	232	232

TABLE 6.8: Maximum seismic shear force (kN) on the lining for EPP model.

in rock masses with Q ranging from 1 to 40, under seismic loading ($K_h = 0.30; K_v = -0.15$), were followed:

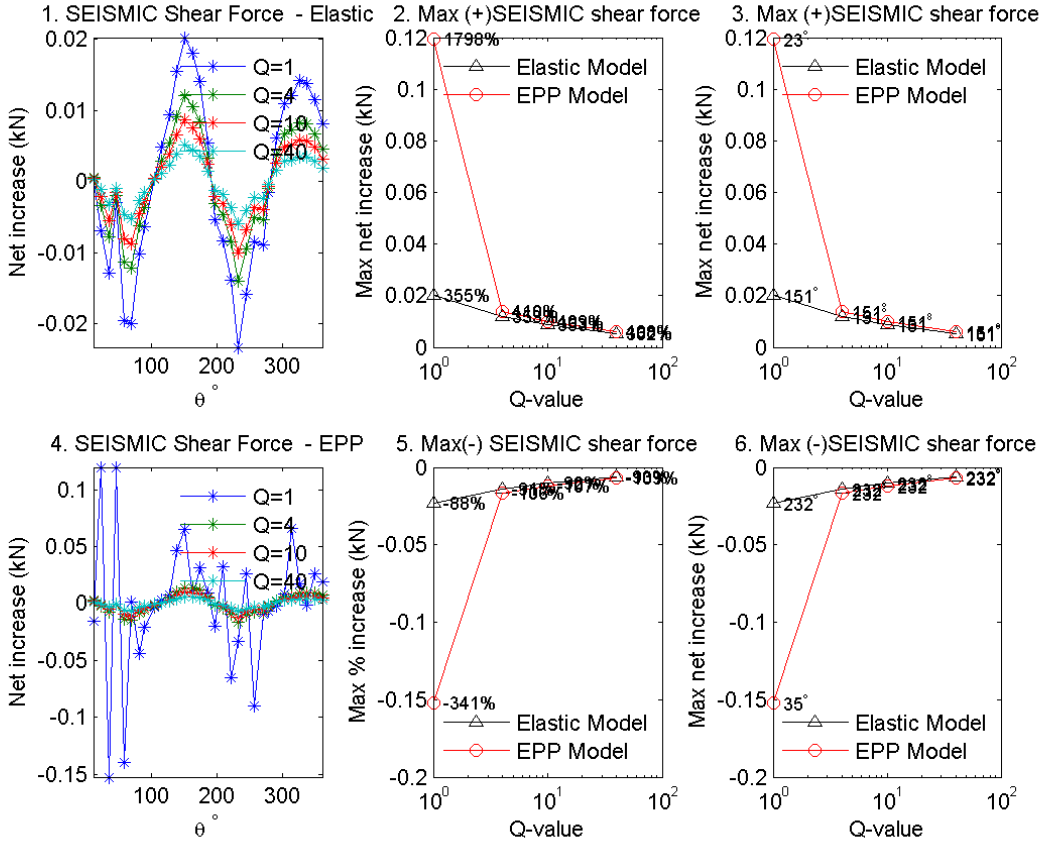

FIGURE 6.14: The seismic shear force, which is the net increase in shear force due to seismic loading, in both positive and negative direction, for both elastic and elastic-perfectly-models are shown. The % increase and the location of the maximum increase on the tunnel for all rock masses using elastic and elastic-perfectly-plastic models are also presented.

- The variation of axial force, bending moment, and shear force along the tunnel periphery for elastic-perfectly-plastic (EPP) models are plotted as a function of the location in degrees as shown in Figs. 6.8, 6.11 and 6.13. The data for elastic models are not included in this comparative analysis between axial force, bending moment, and shear force to serve as a proxy for support pressure. All three parameters have a periodic trend, with two peaks and two troughs. It can be observed that the magnitude of the axial force is at least three orders of magnitude larger than the shear force. The magnitude of the bending moment is also small. The static condition data are plotted as "stars" and the data corresponding to quasi-static seismic loading at the same point are shown by "squares". While comparing the seismic and static loading data, the axial force and bending moment show significant difference between the static and seismic loading scenarios. On the other hand, the shear force does not have any significant variation between static and seismic loading. It appears that the shear force on the lining is relatively insensitive to seismic loading under the conditions simulated in these experiments.

  As a function of the Q values, the magnitude of all three parameters tend to decrease as the rock mass quality increases from 1 to 40. This is in line with the physical expectation as the better quality rocks are expected to exert lower load on the support liner than poor

rock masses.

- The net increase in axial force, bending moment, and shear force at every liner element were calculated using the steps described in Chapter 5. The net increase, shown in Fig. 6.15, is the difference between the axial force, bending moment, or shear force on the lining for static and seismic conditions. As was the case with the magnitude of the parameters, the net increase also has a periodic nature along the periphery of the tunnel. The location of the maximum net increase is dependent on the direction of the seismic inertial force applied, determined by the signs of the seismic coefficients. It can be observed for all three cases that the net increase for rock mass with Q = 1 is the largest. However, the trend around the tunnel is more uniform for the axial force (Fig. 6.15(a)), and the net increase in bending moment and the shear force show a rather haphazard behavior, where drastic changes occur in the data points at two adjacent liner elements (see Figs. 6.15(b) and 6.15(c)). Owing to the "noisy" trend and the relatively small magnitude, it is apparent that using these two parameters to represent the support pressure could have higher uncertainties than using the axial force.

- The axial force, bending moment, and shear force on the liner were plotted against the predicted support pressure as shown in Fig. 6.16. Only the plot using the support pressure from Barton et al. (1974) is shown here, but the exact trend is observed for support pressure using Bhasin and Grimstad (1996), or even just $Q^{-1/3}$. The predicted support pressure has a higher correlation with the axial force on the liner than with either bending moment or shear force on the lining. At the roof of the tunnel, the correlation coefficient of support pressure with the three parameters are 0.99 for axial force, 0.86 for shear force, and 0.78 for bending moment.

  In addition to the higher correlation coefficient, the axial force on the liner has a larger range of variation ($\sim$ 200 kN) than bending moment ($\sim 2 \times 10^{-3}$ kNm) or shear force ($\sim 2 \times 10^{-3}$ kN) over the same range of support pressure or Q. Thus, using the axial force as the proxy, or even to determine the support pressure during seismic loading will result in a more reliable method than with using bending moment or shear force.

Thus, the axial force on the lining is used as a proxy to represent the support pressure and therefore is used to calculate the support pressure during seismic loading. The bending moment and shear force on the liner are not used for analysis from here. The reasons for choosing the axial force over either the bending moment or the shear force are summarized as follows:

- The axial force is more sensitive to seismic loading than shear force or bending moment and therefore it serves as a better option to use it to determine the increase in support pressure. The support pressure for seismic loading shall be determined by scaling the predicted static support pressure using the ratio of the axial force for seismic and static loading (see Chapter 7).

- The magnitude of the axial force is larger, by three orders of magnitude, than either bending moment or shear force. Since the following steps during interpretation involves taking the ratio of the chosen parameter for seismic and static loading, the near-zero values for

bending moment and shear force could result in large number, thereby jeopardizing the stability of the proposed methodology.

- There are more often reversal of sign of the bending moment and shear force along the tunnel periphery. Thus, using bending moment or shear force could complicate the methodology as the reversal of the polarity will also have to be considered during the analysis. On the other hand, the axial force, although shows decrease or increase in magnitude, is always found to be positive along the tunnel.

- The predicted static support pressure has a higher correlation linear relationship with axial force on the lining than either bending moment or shear force. Thus, the axial force on the liner is a better proxy for support pressure and therefore axial force during seismic loading can be used to determine the *seismic* support pressure.

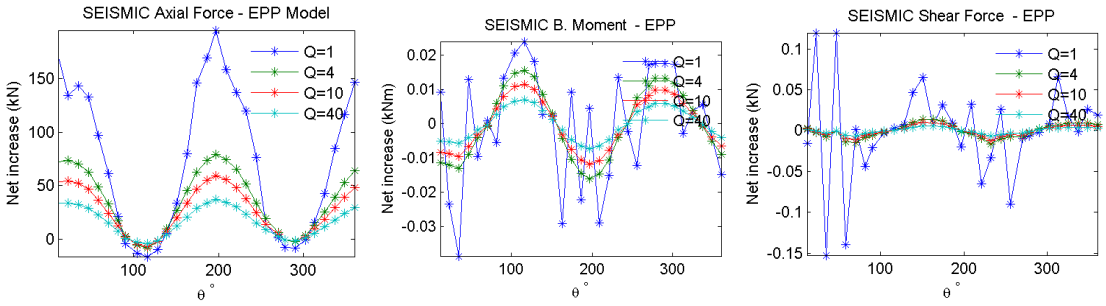

(a) Axial Force (b) Bending Moment (c) Shear Force

FIGURE 6.15: Net increase in axial force, bending moment, and shear force on the liner as function of location along the tunnel. 0° is the east wall and 90° is the roof of the tunnel.

6.4 Influence of Tunnel Dimension

In order to investigate the influence of tunnel dimension on the variation of axial force on the lining, a set of experiments, with tunnel diameter from 5 m to 20 m at 5 m interval, was conducted. The depth of the roof of the tunnel, irrespective of the diameter of the tunnel, is fixed at 60 m. The rock mass quality Q in which the tunnels are excavated is chosen as 1 and 40. Using these two Q-values to represent poor rock mass and good rock mass enables us to study the effect of rock mass quality, in conjunction with the tunnel dimension. A fixed seismic loading of $K_h = 0.30; K_v = -0.15$ was chosen for this experiment. For all experiments, the external boundary was kept unchanged, where the external boundary was placed at 10 times the largest dimension of 20 m (i.e. at 200 m from the tunnel periphery).

The variation of axial force around the tunnel periphery for tunnel diameter ranging from 5 - 20 m at a depth of 60 m in a rock mass with Q=1 is shown in Fig. 6.17. It can be inferred that the magnitude of the axial force for both static and seismic loading increases with tunnel dimension for tunnels in poorer quality rock masses with Q=1. The axial force on the lining for tunnels in good quality rock mass with Q=40 (see Fig. 6.18) also bears the same trend around the tunnel periphery, but the increase in axial force with increasing tunnel dimension is

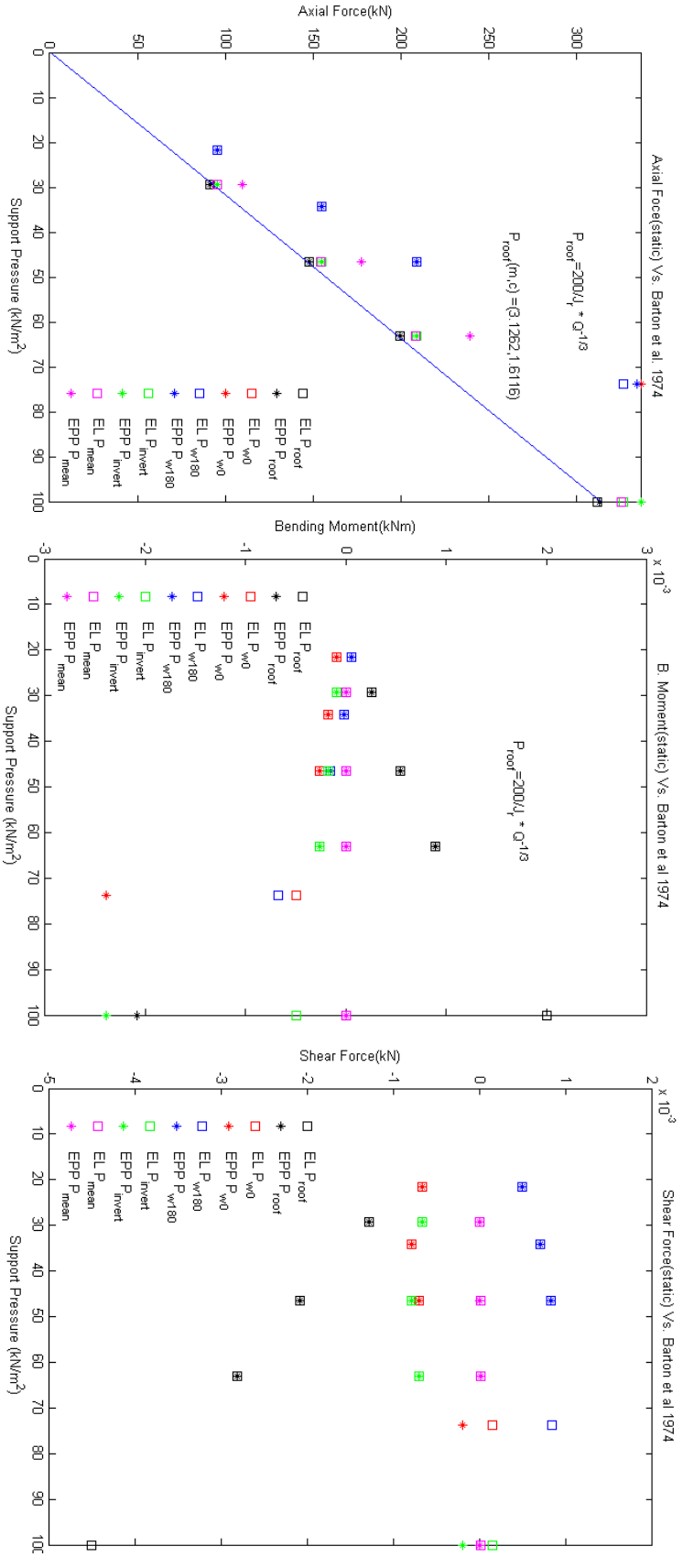

(a) Axial Force (b) Bending Moment (c) Shear Force

FIGURE 6.16: Correlation between predicted support pressure and the axial force, bending moment, and shear force on the liner. The predicted support pressure has a better linear correlation with axial force than with bending moment or shear force on the liner.

insignificant compared to tunnels in poorer rock mass with Q=1. For tunnel dimension from 5 to 20 m, the average axial force on the lining increases by 10 kN for good quality rocks, whereas for poorer quality rock mass the increase is around 100-200 kN.

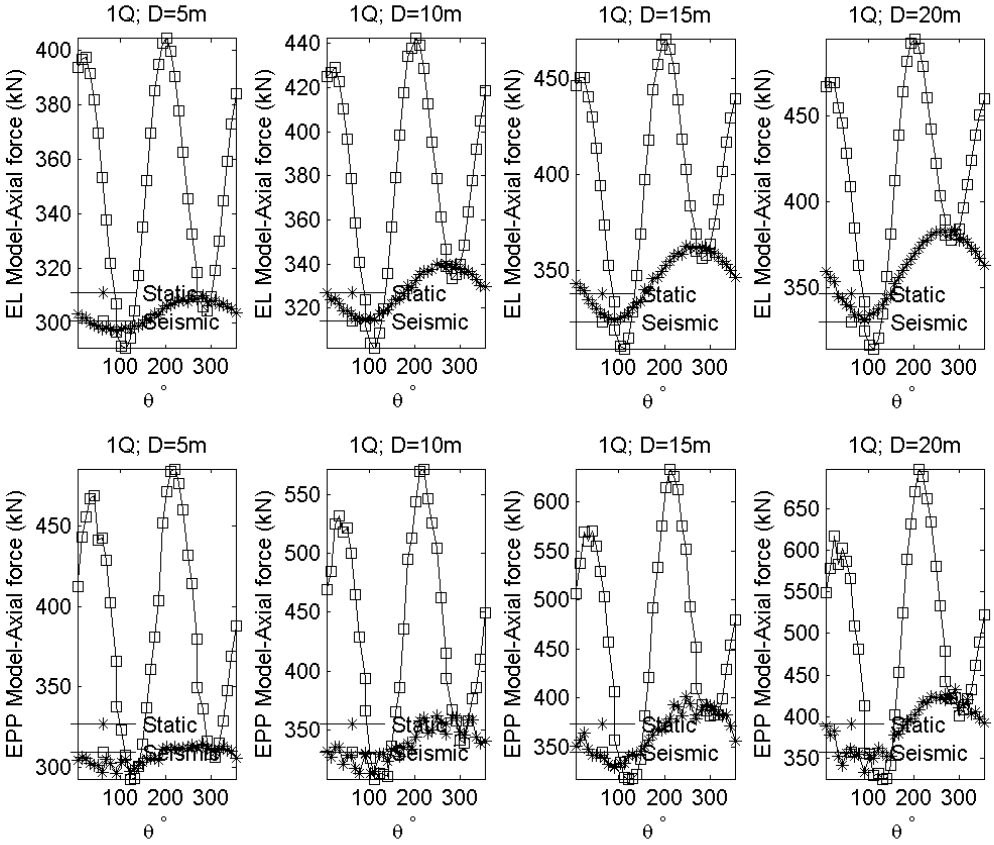

FIGURE 6.17: The variation of axial force around the tunnel periphery for tunnels with diameter ranging from 5-20 m in poor rock mass with Q=1. The average axial force for both static and seismic loading increases with increasing tunnel dimension.

This increase in axial force on the lining for poor rock mass with Q=1 and relatively insignificant increase for good rock mass with Q=40 is depicted clearly by taking the average axial force around the tunnel liner and plotting it on the same scale (see Fig. 6.19). For tunnels in good quality rock mass with Q=40, the mean axial force for both static and seismic loading for both elastic and elastic-perfectly-plastic models appear "flat" as the increase in axial force with respect to tunnel dimension is meager compared to the increase in axial force for the same conditions for the tunnels in poorer rock mass with Q=1.

At the depth of 60 m, in-situ stress is still under the elastic limit for good rock mass with Q=40 (as demonstrated in Table 6.2) and thus behaves elastically. On the other hand, for poorer rock mass with Q=1, the elastic limit has been surpassed at this depth and the "yielded" plastic zone has formed around the tunnel periphery and thus exhibits elastic-plastic behavior. The characteristics of the development of the plastic zone and distribution of major principal stress σ_1 around the tunnels with diameter ranging from 5 to 20 m in rock mass with Q=1 are shown in Figs. 6.20. For both static and seismic loading, the zone of high stress accumulation around the tunnel increases with increasing tunnel dimension, which is the possible cause of increase

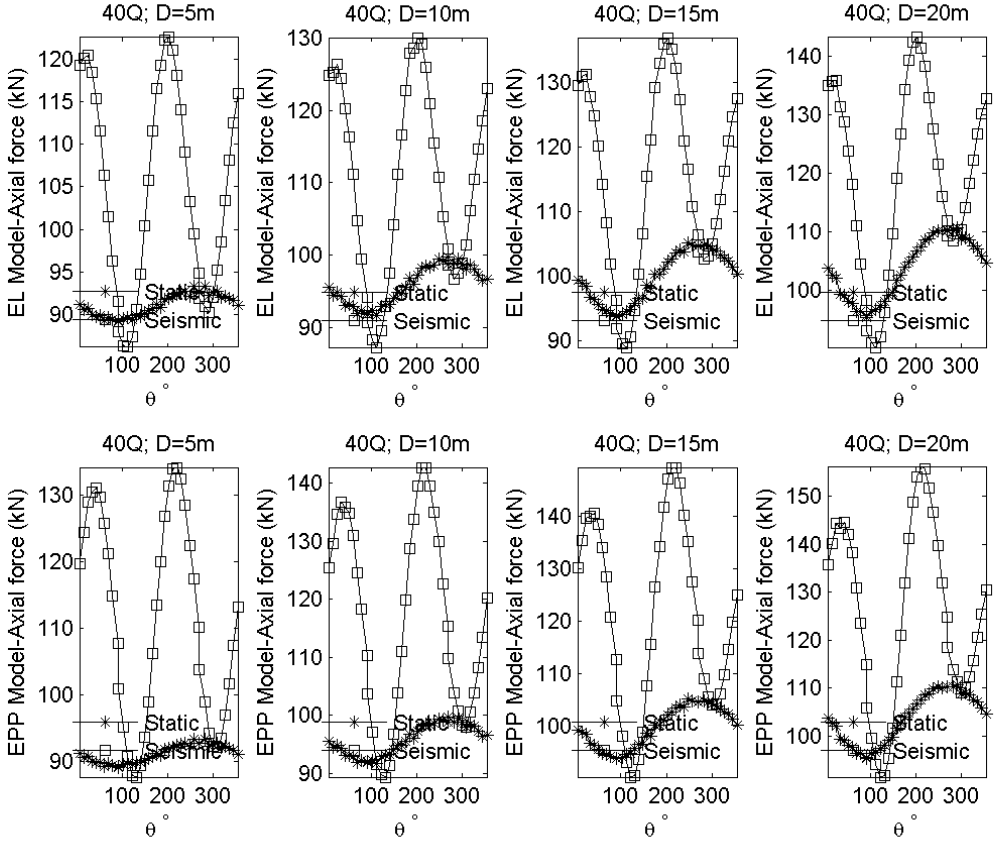

FIGURE 6.18: The variation of axial force around the tunnel periphery for tunnels with diameter ranging from 5-20 m in good quality rock mass with Q=40. The increase in axial force on lining with increasing tunnel dimension is insignificant compared with Q = 1.

in axial force on the lining with tunnel dimension for tunnels in poorer rock mass. During static condition, the zone of highest stress is around the invert (270°), but it shifts toward the knee ($\sim 225°$) of the tunnel when the seismic loading with seismic coefficients $K_h = 0.30; K_v = 0.15$ is applied.

From the result of numerical modeling in Phase^2 thus far, it can be concluded that: (1) the axial force on the lining, represented by the mean in this case, is independent of tunnel dimension for good rock masses (i.e. Q=40) and (2) the axial force on the lining increases with increasing tunnel diameter for poorer quality rock mass (i.e. Q=1). As it has already been demonstrated that the axial force is a reasonable proxy for the predicted support pressure, this result from numerical modeling corroborates previous findings by Barton et al. (1974), Bhasin and Grimstad (1996), Goel et al. (1996), and Bhasin et al. (2006), among others who have studied the predicted support pressure under the purview of different rock mass classification systems.

The next step is to analyze how the increase in axial force due to seismic loading, referred to as *seismic axial force*, depends on tunnel dimension. In other words, this is an attempt to see if the effect of earthquakes, due to ground shaking, is more important for larger tunnels than it is for smaller tunnels. The seismic axial force is calculated as the difference between the axial force for seismic loading (i.e. Stage 3 in Fig 5.7) and the axial force at the same location on

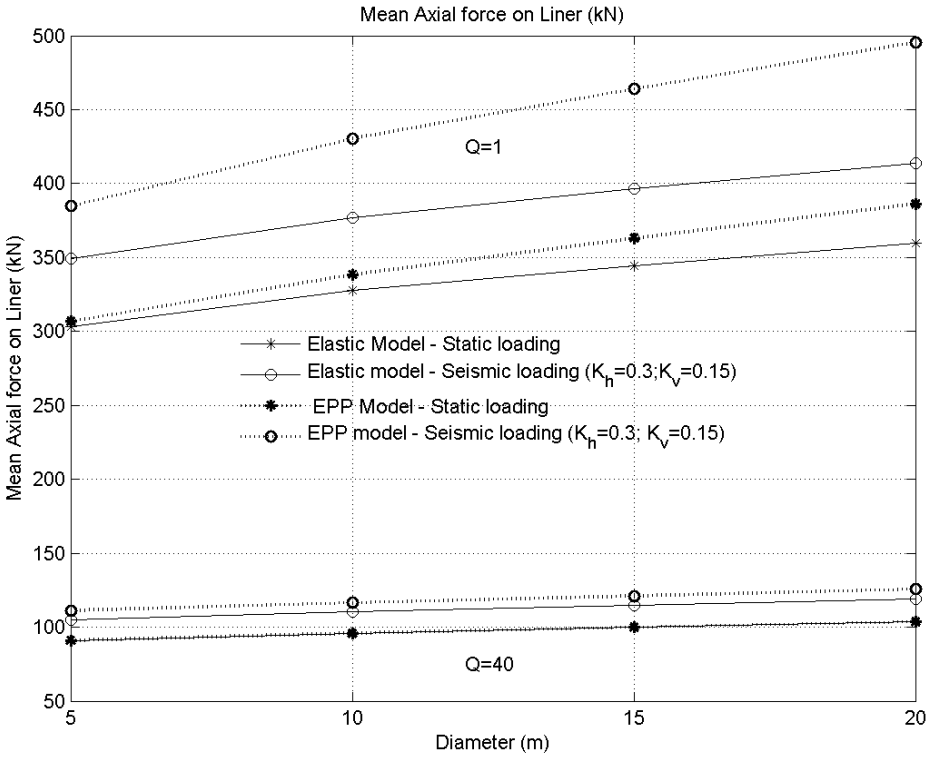

FIGURE 6.19: The mean axial force on the lining for elastic and elastic-perfectly-plastic models of tunnels in both good quality (Q=40) and poor rock mass (Q=1) is shown here. Taking the mean of all the values around the tunnel gives a representative number as all the axial forces on the liner were positive. The seismic loading corresponds to quasi-static loading with $K_h = 0.30; K_v = -0.15$.

the liner for static loading (i.e. Stage 2 in Fig. 5.7). For different experiments, the maximum seismic axial force experienced for that particular experiment setup is used as a parameter of comparison with other experiments. The steps to calculate the seismic axial force are described in Section 5.4.

The seismic axial force along the tunnel circumference for good rock mass with Q = 40 and for poorer rock mass with Q = 1 are shown in Figs. 6.21(a) and 6.21(b), respectively. For the good rock mass, the seismic axial force plots for elastic and elastic-perfectly-plastic models are within the same range (> 50 kN) indicating that the good rock mass, although modeled as elastic-perfectly-plastic rock masses, tend to show elastic behavior at 60 m depth. Besides, the variation in the seismic axial force as the tunnel diameter is increased from 5 to 20 m is also insignificant for both elastic and elastic-perfectly-plastic models. As shown in Fig. 6.21(a) (subplot 3), the maximum positive seismic axial force for all tunnel dimensions are within the same range of 40-50 kN. The same data are presented in Tables 6.9 and 6.10.

On the other hand, for the tunnels in poorer rock masses, by comparing the Subplots 1 and 3 in Fig. 6.21(b), it can be construed that the seismic axial force for elastic-perfectly-plastic is nearly double of the seismic axial force for elastic models. Similarly, there is a significant variation in the magnitude of the seismic axial force as the tunnel diameter is increased from 5 to 20 m. The maximum seismic axial force for tunnels with different diameters are plotted in Fig. 6.21(b) (subplots 2 and 4). The magnitude of the maximum positive seismic axial force is much larger than the maximum negative seismic axial force showing that the effect of earthquakes

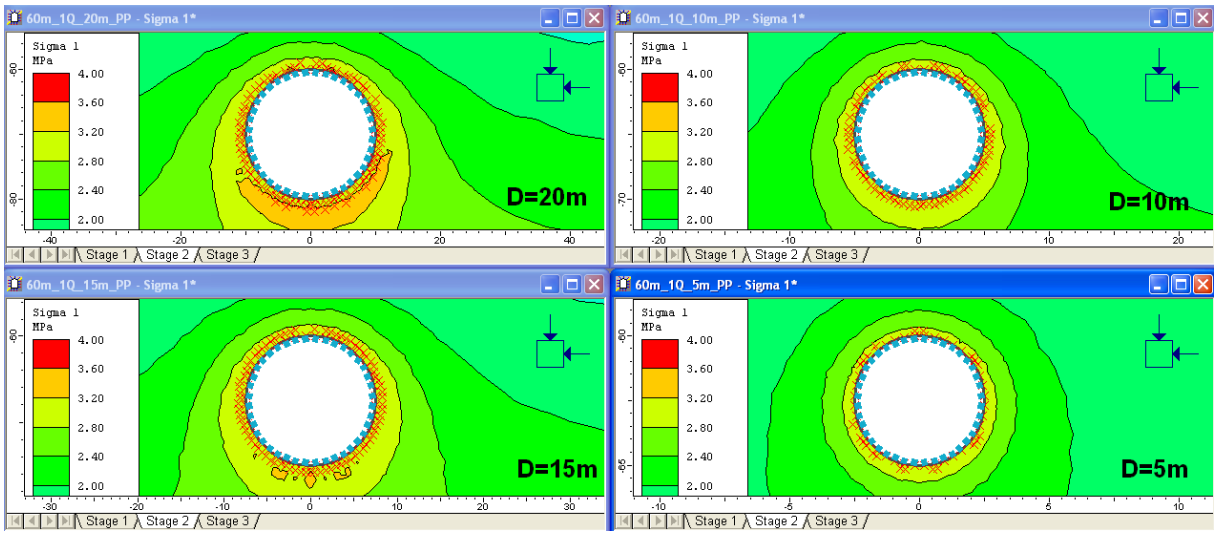

(a) Stage 2 - Static loading

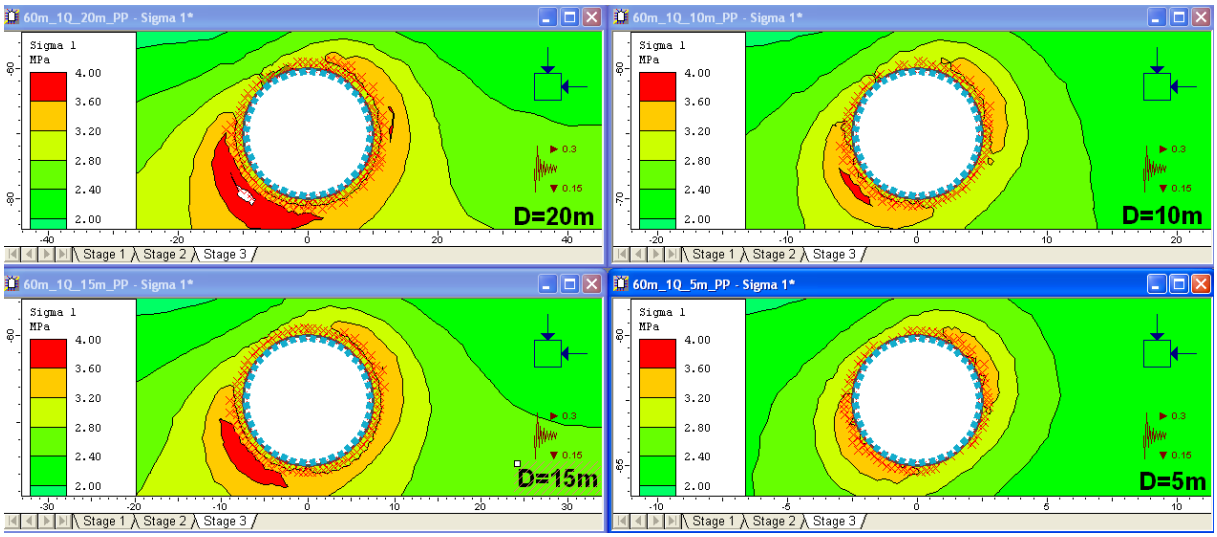

(b) Stage 3 - Static + Seismic loading ($K_h = 0.30; K_v = -0.15$)

FIGURE 6.20: The distribution of major principal stress σ_1 around the tunnels with diameter ranging from 5 to 20 m in poor rock mass with Q=1. It can be seen that the zone of high stress increases with increasing tunnel diameter. Subfig.(a) is for static condition and (b) shows seismic loading ($K_h = 0.30; K_v = -0.15$). The 'x' marks around the tunnels show yielded elements.

under the conditions simulated in this study (circular tunnel, hydrostatic stress, and quasi-static seismic loading with $K_h = 0.30; K_v = -0.15$) is dominated by the axial compression of the liner rather than tension. The maximum seismic axial force increases linearly from 56% of the static axial force for 5 m diameter tunnel to about 71% of the static axial force for the 20-m diameter tunnel in poorer rock mass. The details including the location on the tunnel at which the maximum seismic force occurs are presented in Tables 6.11 and 6.12

This confirms that, for tunnels in poorer rock masses (i.e. Q=1), not only does the absolute axial force on the lining, for both static and seismic loading, increase with increasing tunnel diameter, but the net increase or the seismic axial force, calculated by taking the difference of the axial force for seismic and static loading, also increases linearly with increasing tunnel dimension. On the contrary, for good rock mass (Q=40), the absolute axial force for seismic

and static loading, and the seismic axial force appears to the relatively independent of tunnel dimension.

	D=5m	**D=10m**	**D=15m**	**D=20m**
Max.(+)	30.6	32.8	34.8	36.6
%	33	34	34	35
$\theta_+(^\circ)$	203	203	203	194
Max.(-)	-3.47	-4.46	-5.57	-6.39
%	-4	-5	-6	-7
$\theta_-(^\circ)$	112	112	112	112

TABLE 6.9: Maximum seismic axial force (kN) on the lining for elastic model for Q=40.

	D=5m	**D=10m**	**D=15m**	**D=20m**
Max.(+)	41.8	44.6	46.7	48.7
%	45	45	45	45
$\theta_+(^\circ)$	221	212	212	212
Max.(-)	-2.21	-3.81	-5.18	-6.37
%	-2	-4	-5	-6
$\theta_-(^\circ)$	130	130	130	130

TABLE 6.10: Maximum seismic axial force (kN) on the lining for elastic-perfectly-plastic model for Q=40.

	D=5m	**D=10m**	**D=15m**	**D=20m**
Max.(+)	98.1	110	118	125
%	32	33	33	34
$\theta_+(^\circ)$	203	203	203	194
Max.(-)	-7.65	-13	-17.3	-20.7
%	-3	-4	-5	-6
$\theta_-(^\circ)$	112	112	112	112

TABLE 6.11: Maximum seismic axial force (kN) on the lining for elastic model for Q=1.

	D=5m	**D=10m**	**D=15m**	**D=20m**
Max.(+)	173	212	255	289
%	56	59	68	71
$\theta_+(^\circ)$	212	212	212	212
Max.(-)	-6.18	-17.8	-24.5	-31.8
%	-2	-5	-7	-9
$\theta_-(^\circ)$	130	130	130	130

TABLE 6.12: Maximum seismic axial force (kN) on the lining for EPP model for Q=1.

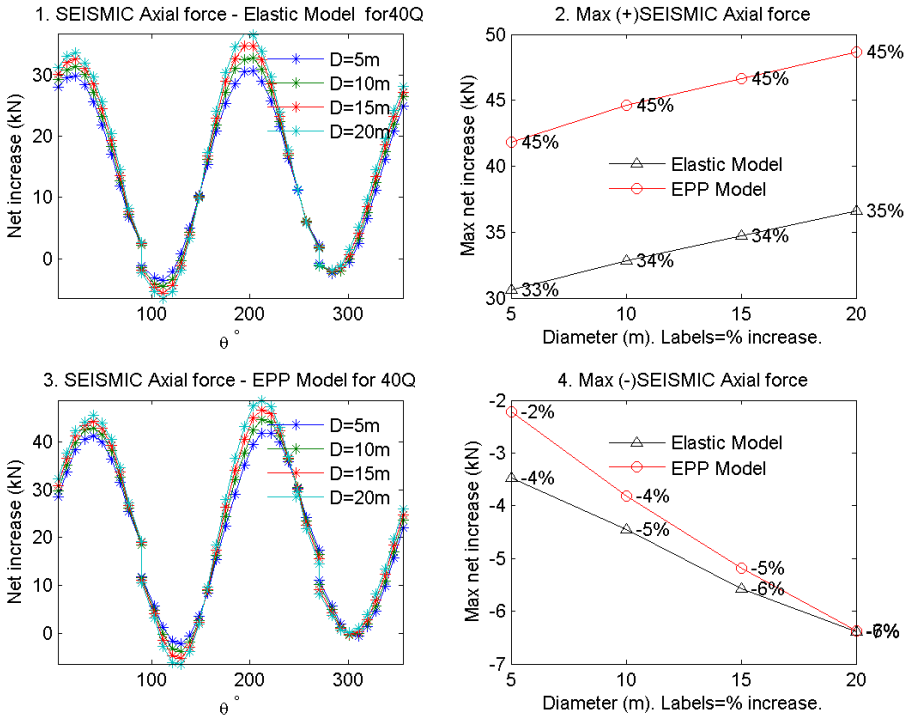

(a) Seismic axial force for Q=40

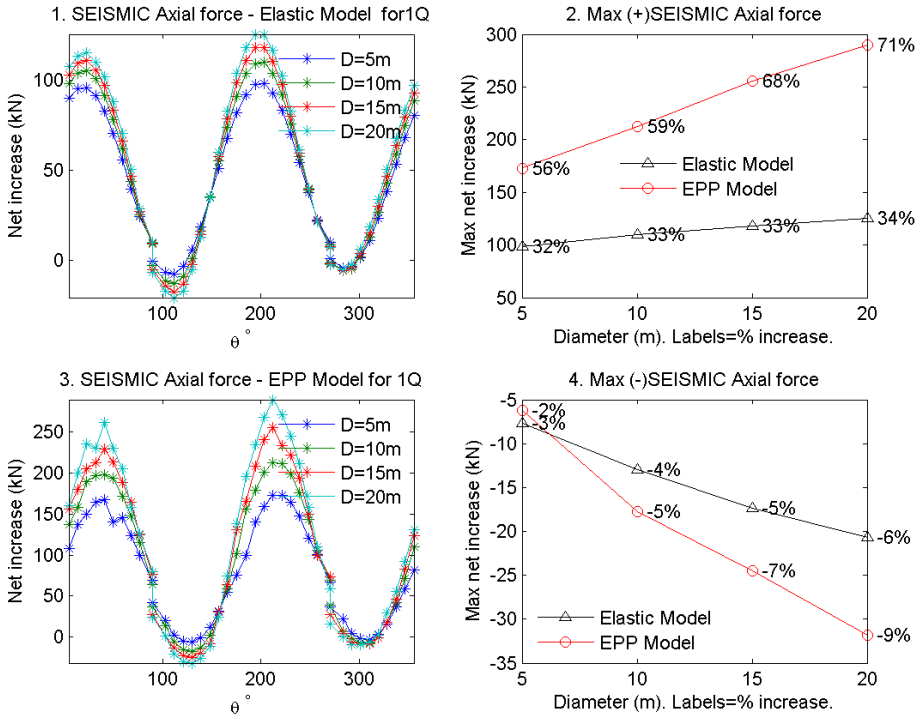

(b) Seismic axial force for Q=1

FIGURE 6.21: Seismic axial force for tunnels with different diameter placed in rock mass with Q=40 and Q=1. The subfigures are:(1) seismic axial force for elastic model; (3) seismic axial force for elastic-perfectly-plastic model; (2) maximum positive seismic force (compression); (4) maximum negative seismic force (tension). The labels on these subfigs. 2 and 4 show the % increase w.r.t to the static seismic axial force at the same location on the liner.

Chapter 7

Seismic Rock Mass Quality $Q_{seismic}$

For a given rock mass with quality index Q surrounding a tunnel, a hypothetical Q, referred to as $Q_{seismic}$, can be assigned in order to represent the effect of seismicity on the tunnel during earthquakes. In other words, during seismic loading, the increase in load, or rock support pressure, due to ground shaking exerted by the surrounding rock mass on the tunnel liner can be visualized as the effect of reducing the rock mass quality from Q_{static} to $Q_{seismic}$. The Q_{static} used here is same as the *normal* Q that is calculated from the six parameters, the ratings of which are obtained through field work or tunnel mapping as per rating charts shown in Section 2.1.

Determining $Q_{seismic}$, which is $\leq Q_{static}$, to account for the impact of earthquakes has great practical importance. Using the new Q-value as $Q_{seismic}$, the new support system to compensate for the expected earthquake at the tunnel location can be directly obtained from the existing Q-system design chart (Fig. 2.3).

The concept of $Q_{seismic}$ was first introduced by Barton (1984) where it was recommended to reduce the Q value as an effect of increasing the SRF (Stress Reduction Factor) to compensate for earthquake loading. As a rule-of-thumb for poorer rocks, it was recommended that the Q value be reduced by a factor of 0.5 in order to achieve a 25% increase in support pressure. Thus, as a "crude approximation for poorer qualities of rock mass", Eq. 7.1 was proposed by Barton (1984) to relate $Q_{seismic}$ to Q_{static}.

$$Q_{seismic} = 0.5\, Q_{static} \tag{7.1}$$

Using this equation, the 25% increase in predicted support pressure due to reduction of Q to compensate for seismic loading can be demonstrated using the empirical relationship between Q and predicted support pressure (see Eqs. 2.3 and 2.4), which shows that $P_{roof} = C \times Q_{static}^{-1/3}$. C is a constant that depends on the Joint Roughness Number J_r for good quality rocks (Barton et al., 1974) and is dependent on J_r and tunnel diameter D for poor quality rocks (Bhasin and Grimstad, 1996). By replacing Q_{static} with $Q_{seismic}$, the predicted support pressure for seismic conditions can be calculated as follows:

$$\begin{aligned} P_{seismic} &= C \times Q_{seismic}^{-1/3} \\ &= C \times (0.5 Q_{static})^{-1/3} \\ &= 0.5^{-1/3} \times C \times Q_{static}^{-1/3} \\ &\approx 1.25\, P_{static} \end{aligned} \tag{7.2}$$

It is however felt that reducing the Q by 0.5 to account for *possibly* all levels of earthquake loading is "too generic" and there appears to be some room for refinement. Thus, it is postulated that the $Q_{seismic}$ is related to Q_{static} through a coefficient α_k as shown in Eq. 7.3. Depending on the expected level of earthquake loading, usually inferred from existing seismic hazard maps in terms of peak ground acceleration, α_k can be either greater or smaller than 0.5. It is also expected that for certain range of seismic coefficients used as an input for quasi-static loading and which represents the intensity of seismicity, α_k will be equal to 0.5 as recommended by Barton (1984).

$$Q_{seismic} = \alpha_k\, Q_{static} \tag{7.3}$$

The term α_k, which is always less than unity, will predominantly be dependent on the seismic coefficient K, which in turn is linked to peak ground acceleration (PGA) or other ground motion parameters that are used to represent seismic hazard. Using this equation, in order to obtain $Q_{seismic}$ to compensate for the expected earthquake loading on the tunnel, the Q_{static} shall be reduced by different proportions (i.e. α_k) for different seismic hazard zones, which are commonly expressed in terms of peak ground acceleration. It can be inferred that α_k could depend on other factors such as the properties and thickness of the liner, and dimension of the tunnel, and even the rock mass quality Q of the surrounding rock mass, among others.

Using the same analogy as the steps followed to derive Eqn. 7.2, the predicted support pressure under seismic loading $P_{seismic}$ and the predicted support pressure under static conditions P_{static} can be related using α_k as shown in Eqn. 7.4.

$$P_{seismic} = {\alpha_k}^{-1/3}\, P_{static} \tag{7.4}$$

Although the seismic support pressure can also be calculated using α_k and static support pressure P_{static}, other than merely using it to investigate the increase in support pressure due to seismic loading, it merits more to work in terms of $Q_{seismic}$. As discussed earlier, using $Q_{seismic}$, the new support system to account for the additional seismic load can directly be obtained from the existing Q-system tunnel design chart for static conditions. There are, however, some *caveats* that have to be noted while using this approach as discussed below.

It may be noted here that as the Q-value is reduced to compensate for seismic loading, the general trend recommended to increase the support pressure using Q-system chart is to *decrease* the bolt spacing and *increase* the thickness of fiber-reinforced shotcrete (Sfr) liner. It is however mentioned in Barton (1984) and verified through numerical modeling using Phase^2 (see Fig. 7.1) that the forces on the liner increase as the thickness of the liner increases. Barton (1984) stated that the forces on the lining increases as its rigidity with relative to the surrounding rock mass increases and suggested that increasing the modulus of the surrounding incompetent rock

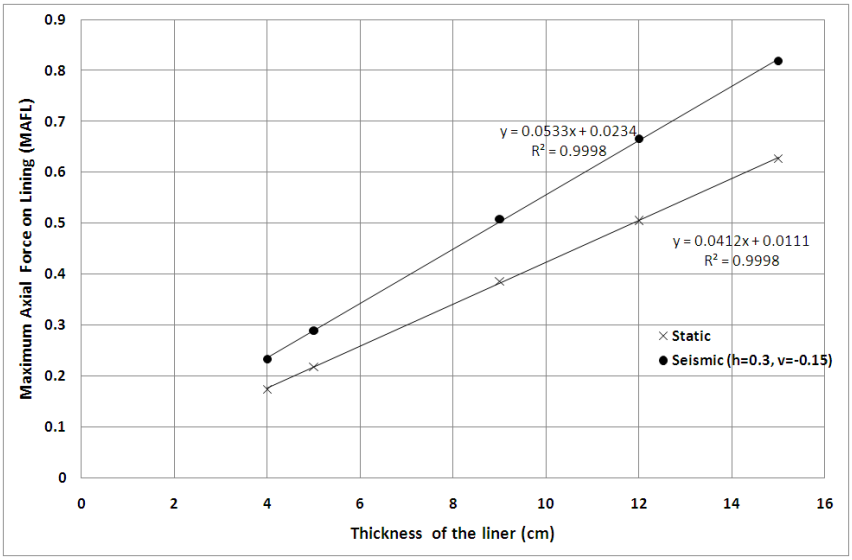

FIGURE 7.1: Plot of Maximum Axial Force on the Lining (MAFL) as a function of thickness of the shotcrete liner for a 20-m diameter tunnel in rock mass with Q = 1. It can be observed that the MAFL, which is representative of the support pressure, is linearly proportional to thickness of the shotcrete liner. With all other parameters remaining constant, the thickness of the liner is representative of the relative rigidity of the liner-rock mass system as per Eq. 7.5.

mass "by grout injection and bolting will therefore be very useful". He also suggested the use of "thin flexible liners of fiber-or mesh-reinforced shotcrete and systematic bolting to increase the modulus of the surrounding rock."

Many investigators (for e.g. St John and Zahrah (1987) and Hashash et al. (2001)) reported the effect of the flexibility ratio, the inverse of rigidity ratio, on the tunnel response for both static and dynamic loads. The flexibility ratio F is dependent on the Young's modulus E and Poisson's ratio ν of the rock mass, and Young's modulus E_l, Poisson's ratio ν_l, radius R, and thickness t of the liner. Eq. 7.5 from St John and Zahrah (1987) shows the relationship for the flexibility ratio F of a circular liner.

The flexibility ratio is a measure of how flexible the liner is with relative to the surrounding rock mass. Higher flexibility ratio indicates "flexible" liners, which has the ability to move together with the rock mass experiencing displacement and thus are less susceptible to damage during earthquakes. The flexibility ratio is directly proportional to the modulus of the surrounding rock mass, indicating that, assuming the liner properties remain unchanged, the flexibility ratio is larger for good quality rock mass than poor rock masses. The Young's modulus of the liner has an inverse relationship with flexibility ratio, which shows that less stiff (low E modulus) liners have higher flexibility ratio. Similarly, the thickness of the liner and the radius of the liner, or rather the cube of their ratio, also affect the flexibility ratio.

$$F = \frac{2E(1-\nu_l^2)\,R^3}{E_l(1+\nu)\,t^3} \tag{7.5}$$

From Eq. 7.5, it can be inferred that thin liners with large tunnel radii will result in higher flexibility ratio. A liner is considered perfectly flexible (or to have low rigidity) if the flexibility ratio exceeds 20, in which case the liner "conforms" to the deformation imposed by the surrounding rock mass (St John and Zahrah, 1987). For the 10-m diameter tunnel in rock mass

with Q = 1, the flexibility ratio for the liner used in this study (see Table 5.2) is on the order of 10^5 and therefore can be considered a flexible liner.

This suggests that as the Q-value is reduced, the increase in support pressure achieved through the increase in thickness of fiber-reinforced shotcrete (Sfr) should be compensated either by more rock bolts or by grouting the failed rock mass surrounding the tunnel as increasing the thickness of the liner would have an adverse effect – opposite of what is attempted to achieve. The flexibility ratio shown in Eq. 7.5, which shows the dependence of the flexibility ratio on the geometry of the tunnel, and liner and rock mass properties, could serve as a guideline for choosing optimum support. The right combination of shotcrete thickness, grouting, and bolting should be chosen such that the required support pressure as suggested by $Q_{seismic}$ is achieved while at the same time the flexibility of the installed liner is kept high (i.e. low rigidity liner). Power et al. (1998) also recommended preferable measures as those that would increase the strength and ductility while the stiffness of the support system is kept as low as possible.

The steps involved to derive the expression for α_k, in terms of seismic and static axial force on the lining, the output parameters of numerical modeling in Phase^2, are presented in the following sections. Once the coefficient α_k has been determined, the $Q_{seismic}$ is calculated as the product of α_k and Q_{static}. As $Q_{seismic}$ will always be less than Q_{static}, the new support system after considering the increase in support pressure is achieved through the left-ward shift in Q value along the Q-axis in the Q-system support chart shown in Fig. 2.3.

7.1 Support Pressure Vs. Rock Mass Quality Q

From the empirical relationships shown in Eqns. 2.3 and 2.4, it can be stated that the predicted support pressure P_{static}, for static conditions, is inversely proportional to Q (or $Q^{-1/3}$ to be exact) as follows:

$$P_{static} = C_{static}\, Q_{static}^{-1/3} \tag{7.6}$$

where P_{static} is the predicted support pressure under static conditions, Q_{static} is the normal Q obtained from the six Q parameter ratings obtained through field or tunnel mapping, and C_{static} is a proportionality constant that depends on the Joint Roughness Number J_r for good quality rock masses (Barton et al., 1974) and on the tunnel diameter D and J_r for poorer quality rock masses (Bhasin and Grimstad, 1996).

Using the same analogy as in Eq. 7.6, the relationship between predicted support pressure under seismic loading $P_{seismic}$ and the *inferred* rock mass quality under seismic loading $Q_{seismic}$ can be expressed as:

$$P_{seismic} = C_{seismic}\, Q_{seismic}^{-1/3} \tag{7.7}$$

Taking the ratio of Equation 7.7 to Equation 7.6, the following relationship can be obtained.

$$\frac{P_{seismic}}{P_{static}} = \frac{C_{seismic}}{C_{static}} \times \left(\frac{Q_{seismic}}{Q_{static}}\right)^{-1/3} \tag{7.8}$$

Assuming that the change in diameter of the tunnel and the J_r of the surrounding rock mass

is insignificant during seismic loading with reference to static loading, the proportionality constant C can be assumed to remain unchanged (i.e. $C_{seismic} = C_{static}$). The change in diameter due to convergence of the tunnel during seismic loading is on the order of less than 1% of the radius of the tunnel. The constant J_r assumption is also reasonable as the "no significant strength loss" is inherent to the pseudo-static seismic loading and thus this method is not recommended for problems involving liquefaction, soil exhibiting significant strength loss during earthquake loading and large earthquakes (Baker et al., 2006). Since the J_r plays a significant role in the strength of the rock mass, the "less strength loss" assumption inherent in pseudo-static loading could be interpreted as constant J_r during seismic loading. Thus, Equation 7.8 can be expressed as follows:

$$\frac{P_{seismic}}{P_{static}} = \left(\frac{Q_{seismic}}{Q_{static}} \right)^{-1/3} \tag{7.9}$$

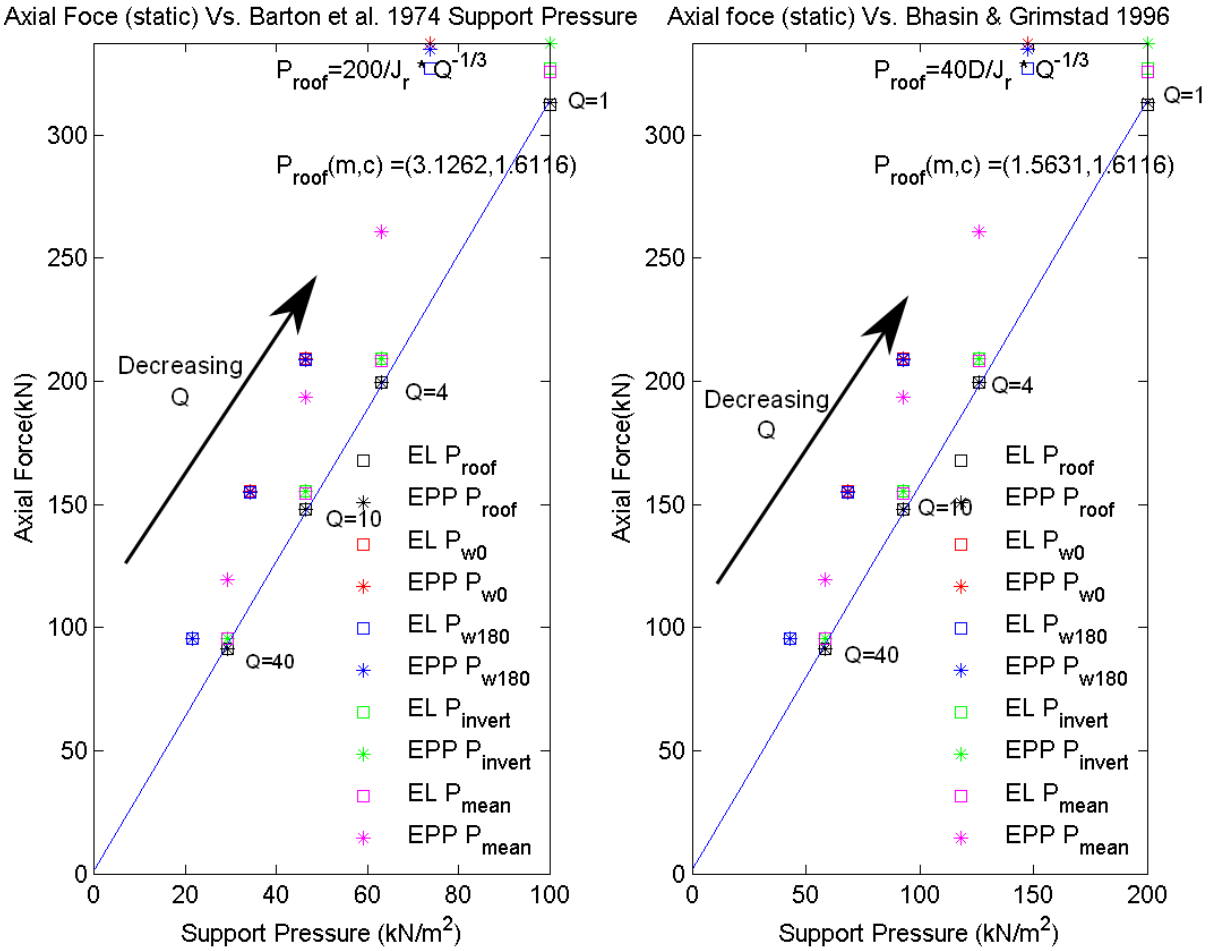

FIGURE 7.2: The static axial force Vs. predicted support pressure showing good correlation between the two quantities. Two plots shown here are for axial force Vs. support pressure predicted using the relationships in Barton et al. (1974) and Bhasin and Grimstad (1996). Axial forces from several locations on the tunnel are plotted. The linear fit is for the axial force on the roof of the tunnel, where m refers to the slope and c is the y-intercept. It may be noted that $c \ll T$ (Axial Force)

7.2 Axial Force Vs. Support Pressure

It has been found that the measured axial force on the lining under static conditions has good correlation with the static support pressure predicted using the equations from Barton et al. (1974) and Bhasin and Grimstad (1996). $J_r = 2$ assumption is made here as this is the typical value of J_r (Barton, 2002). A static axial force Vs. static support pressure for rock masses with Q ranging from 1 to 40 is shown in Fig. 7.2; axial force on the lining from four locations around the tunnel – the roof at 90°, invert at 270°, and two walls at 0° and 180° – are shown in this plot. The best-fit line to the axial force on the lining at the roof of the tunnel and the predicted support pressure, and its slope m and y-intercept c are overlain on Fig. 7.2. Based on the linear relationship and very small y-intercept c (less than 2% of the average axial force), the relationship between static axial force T_{static} and the static predicted support pressure P_{static} can be established as:

$$T_{static} = m_{static} \times P_{static} \tag{7.10}$$

where m_{static} is the slope of the best-fit line of the static axial force on the lining to the predicted support pressure. It can be inferred that the slope of this line is also mainly dependent on the liner properties and geometric factors of the tunnels.

Using similar analogy, an equivalent relationship between seismic axial force $T_{seismic}$ and seismic support pressure $P_{seismic}$ may be obtained as:

$$T_{seismic} = m_{seismic} \times P_{seismic} \tag{7.11}$$

It can be assumed that the slope of the axial force on the lining Vs. predicted support pressure remains unchanged during seismic loading (i.e. $m_{seismic} = m_{static}$). In other words, the predicted support pressure for seismic loading also bears a linear relationship with the seismic axial force on the liner. For the same tunnel geometry in same rock mass, the slope for the seismic loading is same as slope of the axial force vs. support pressure for static condition. Thus, following this assumption, the relationship between T and P for both seismic and static conditions, obtained by taking dividing Equation 7.11 by Equation 7.10, can be written as:

$$\frac{P_{seismic}}{P_{static}} = \frac{T_{seismic}}{T_{static}} \tag{7.12}$$

Thus by combining, Equations 7.9 and 7.12, the rock mass quality Q for both seismic and static conditions can be linked with the corresponding measured axial force on the lining as follows:

$$\frac{P_{seismic}}{P_{static}} = \frac{T_{seismic}}{T_{static}} = \left(\frac{Q_{seismic}}{Q_{static}}\right)^{-1/3} \tag{7.13}$$

$$\alpha_k = \frac{Q_{seismic}}{Q_{static}} = \left(\frac{T_{seismic}}{T_{static}}\right)^{-3} = \left(\frac{T_{static}}{T_{seismic}}\right)^{3} \tag{7.14}$$

Similarly, from Eq. 7.13, the parameter α_k (defined in Eq. 7.3), which is the ratio of $Q_{seismic}$ to Q_{static}, can be obtained from the measured seismic and static axial force on the

lining as shown in Eq. 7.14. Since $T_{seismic}$ depends on the magnitude and direction of the seismic loading, specified by the seismic coefficient K, a range of α_k values can be obtained for different seismic coefficients for a given tunnel geometry in a particular rock mass.

However as discussed in Chapter 3, only the horizontal component K_h of the seismic coefficient needs to be specified and a vertical seismic coefficient $K_v = -0.5\ K_h$ is always automatically applied for every specified horizontal seismic coefficient K_h. Thus, for different rock masses, a range of α_k shall be obtained for the specified range of K_h. Although α_k at any location along the tunnel can be computed, the point of maximum seismic axial force, or maximum increase in axial force due to seismic loading, is used to compute the α_k as this point of maximum increase is most susceptible to damages due to earthquake loading.

7.3 The α_k vs. K_h plot

The derivation shown above is demonstrated graphically using Fig. 7.3 as described in the following sections.

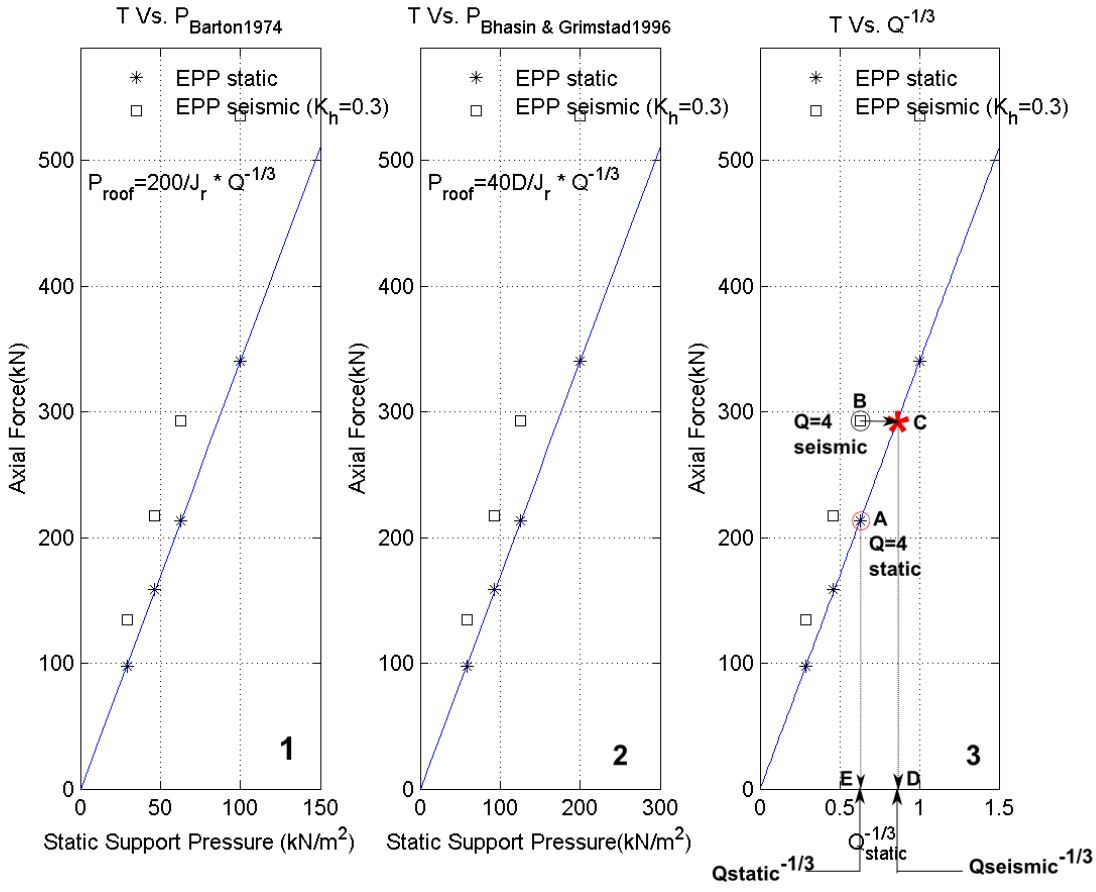

FIGURE 7.3: Graphical representation of determination of α_k from axial force Vs. $Q^{-1/3}$ plot. The axial force at the point on the tunnel where the maximum increase in axial force occurs is plotted here. The first two plots from the left are axial force Vs. support pressure determined from Barton (1984) and Bhasin and Grimstad (1996), respectively. The third plot is used to determine the α_k for that particular seismic loading. The arrows connecting points A - E show the steps followed to determine α_k for Q = 4 under this seismic loading, used here as an example.

- First the static axial force on the lining at the point on the tunnel where maximum seismic axial force occurs is plotted versus $Q_{static}^{-1/3}$, which is proportional to the predicted support pressure under static conditions using the equations from Barton et al. (1974) and Bhasin and Grimstad (1996). This is shown by the "asterisks" in the third plot in Fig. 7.3 and the line of best-fit is also shown. The axial force at the location of the point of maximum positive seismic force (see for e.g. Fig. 6.10) on the tunnel are used for this investigation.

- Then, the seismic axial force on the lining (shown by squares) vs. $Q_{static}^{-1/3}$ at the same location are plotted for all rock masses. It may be noted that the location of maximum seismic axial force on the tunnel may be different for different rock masses, although it *usually* occurs at the shoulder or the knee of the tunnel. Q with no subscript is equivalent to the static Q or Q_{static}. The data points for the seismic axial force lie above the best-fit of static axial force as the seismic axial force at this point is larger than the static axial force.

- By assuming that the slope of $T_{seismic}$ vs. ${Q_{seismic}}^{-1/3}$ is same as the slope of T_{static} vs. ${Q_{static}}^{-1/3}$, the value of $Q_{seismic}$ can be determined from the ${Q_{static}}^{-1/3}$ axis. The data points of a 10-m diameter tunnel in rock mass with Q = 4 under seismic loading with $K_h = 0.30$ and $K_v = -0.15$ are shown subfigure 3 in Figure 7.3. The y-coordinate of point A , the data point with red circle, shows the axial force for static loading and its projection onto the x-axis shown by E. The x-coordinate of point E corresponds to $Q_{static}^{-1/3} \approx 0.6$, confirming that the $Q_{static} = 4$.

  The y-coordinate of point B (data point with black circle) shows the seismic axial force at the same point , which is the point of maximum seismic axial force. This point is first projected onto the best-fit line of static axial force T_{static} Vs. $Q_{static}^{-1/3}$. The point of intersection C, shown by a red "asterisk" on the best-fit line, is further projected onto the x-axis, shown by point D. The x-coordinate of point D is equal to $Q_{seismic}^{-1/3}$ and from this point, the value of $Q_{seismic}$ and therefore the α_k for this particular seismic loading can be determined. In this case,

$$Q_{seismic}^{-1/3} \approx 0.9$$

$$Q_{seismic} = 0.9^{-3} = 1.37$$

$$\alpha_k = \frac{1.37}{4} = 0.34$$

- For a particular tunnel geometry, different scenarios of seismic loading can be tested to obtain α_k as a function of the seismic coefficient K_h. When the seismic loading is changed, the line of best-fit for static condition in Figure 7.3 remains unchanged, but the data points for seismic load gets shifted depending on the magnitude and direction of the seismic coefficient. This shift in data points for seismic loading results in different $Q_{seismic}$ and therefore α_k for different seismic loading.

As an example, the determination of α_k is demonstrated graphically using a 10-m diameter tunnel at 60 m in rock mass with Q=1 for three seismic loading scenarios as shown in Figs. 7.4, 7.6 and 7.7. To represent varying degree of seismic hazard, the horizontal seismic coefficient K_h is increased from 0.05 to 0.7. As described in Chapter 3, this range of horizontal seismic

coefficients correspond to horizontal peak ground acceleration (PGA) of 0.05g - 0.7g at the tunnel location. Again, assuming the reduction factor in Table 3.1, the corresponding the peak ground acceleration at the surface for the specified range of K_h can be estimated to range from 0.07g - 1g. This in turn simulates an earthquake intensity of ∼VII - X on Mercalli Scale (as per Fig. 3.5) experienced at the ground surface.

As justified earlier in Chapter 3, the vertical seismic coefficient K_v equal to half of the horizontal seismic coefficient, in downward direction, is always coupled with the specified horizontal seismic coefficient. Thus, when the K_h is specified as, for example, 0.3, it implicitly means that $K_v = -0.15$ is also included during the quasi-static seismic loading.

As previously mentioned, a value of α_k is obtained for a particular seismic loading, or seismic coefficient, and therefore a series of α_k can be obtained for the range of seismic coefficients as specified above. The resulting α_k vs. K_h for a 10-m diameter tunnel at 60 m depth in a rock mass with Q=1 is shown in Fig. 7.8. Three data points, with $\alpha_K > 0.5$, $\alpha_K \approx 0.5$, and $\alpha_K < 0.5$, labeled sequentially as (1), (2) and (3) are used to demonstrate how the α_k is calculated using the axial force for static condition T_{static}, axial force for seismic condition $T_{seismic}$, and Q_{static}.

As shown in Fig. 7.3, the steps followed to calculate α_k are shown by arrows connecting points labeled A - E and the coordinates of these points are used to determine α_k. Three cases with horizontal seismic coefficient = 0.05, 0.15 and 0.55 are demonstrated in the following sections.

7.3.1 Point 1: $K_h = 0.05; K_v = -0.025$ and α_k = 0.81

The horizontal seismic coefficient K_h chosen for Point 1 is 0.05. The $T_{seismic}$ and T_{static} vs. $Q_{static}^{-1/3}$ plot (similar to Fig. 7.3 for Q = 4) is shown for Q = 1 in Fig. 7.4. Using the coordinates of points A - E from this figure, the following steps can be followed to calculate $Q_{seismic}$ and then α_k.

$$\begin{aligned} K_h &= 0.05 \\ Q_{static} &= 1 \\ T_{static}(kN) &= 340.14 \\ T_{seismic}(kN) &= 364.37 \\ Q_{seismic}^{-1/3} &= 1.07 \\ Q_{seismic} &= 1.07^{-3} = 0.816 \\ \alpha_k &= \frac{Q_{seismic}}{Q_{static}} = \frac{0.816}{1} \approx 0.81 \end{aligned} \tag{7.15}$$

Thus, when a 10-m diameter lined tunnel at 60-m depth, surrounded by rock mass with Q=1, is under seismic loading with seismic coefficients $K_h = 0.05; K_v = -0.025$, the effect of earthquake loading, simulated by reduction of the rock mass quality Q, is such that the $Q_{seismic}$ is $0.81Q_{static}$. The steps followed to determine $Q_{seismic}$ from the coordinates of points A - E are shown in Eq. 7.15. This demonstrates that for some rock masses, especially under

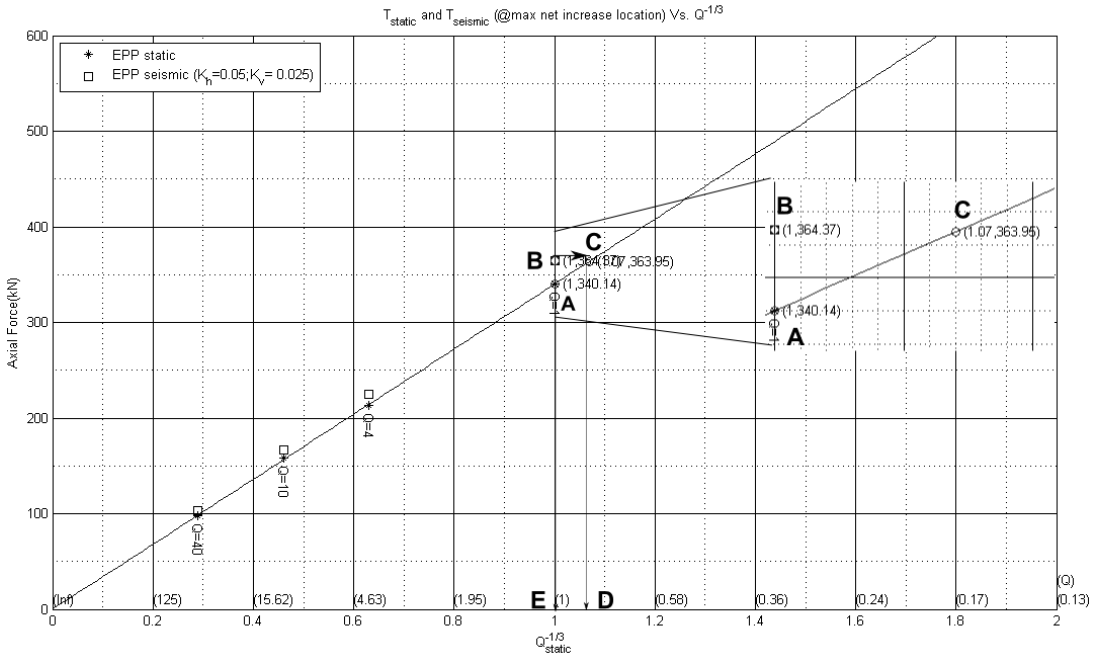

FIGURE 7.4: The axial force on the liner vs. $Q_{static}^{-1/3}$ plot for seismic coefficients $K_h = 0.05; K_v = -0.025$. The corresponding values of Q are shown in brackets along the x-axis. The significance of the coordinates of points A - E are described in the text.

low seismic intensity seismic loading, the $Q_{seismic}$ could be larger than 0.5 Q_{static}. Therefore, the relationship shown in Eq. 7.1 appears to be overly conservative for low seismic loading, representing regions where the expected seismic intensity is low. Assuming that the horizontal seismic coefficient is equal to the peak ground acceleration (PGA) at the depth of the tunnel (as discussed in Chapter 3), the $K_h = 0.05$ used here corresponds to $PGA = 0.05$g at tunnel depth and $PGA = 0.05/0.7 \approx 0.07$g at the surface; in absence of a site-specific attenuation ratio, a constant reduction factor of 0.70 for depths > 30 m, shown in Table 3.1, as suggested by Hashash et al. (2001) and Kontoe et al. (2008) is used here.

Using Eq. 7.4, it can be shown that the 20% reduction in Q value to account for seismic loading results in a mere 7% increase in predicted support pressure. This increase in support pressure due to the specified seismic loading at Point 1 appears insignificant. Even with reference to the tunnel support design chart shown in Fig. 2.3, assuming Excavation Support Ratio (ESR) = 1, both $Q_{static} = 1.0$ and $Q_{seismic} = 0.8$ fall in the same reinforcement category No. 5 (requiring 9 cm fiber-reinforced shotcrete + bolting with 1.7 m spacing (Sfr+B) and therefore does not behoove any increase in support system to account for this seismic loading ($K_h = 0.05; K_v = -0.025$). The new $Q_{seismic}$ along with $Q_{static} = 1$ are plotted on the Q-system design chart, assuming ESR = 1, as shown in Fig. 7.5. This result is in concordance with previous empirical findings by Dowding and Rozen (1978), Sharma and Judd (1991), and Power et al. (1998), where "very little damage" to tunnels were reported when the peak ground acceleration at the ground surface above the tunnels was equal to or less than 0.2g.

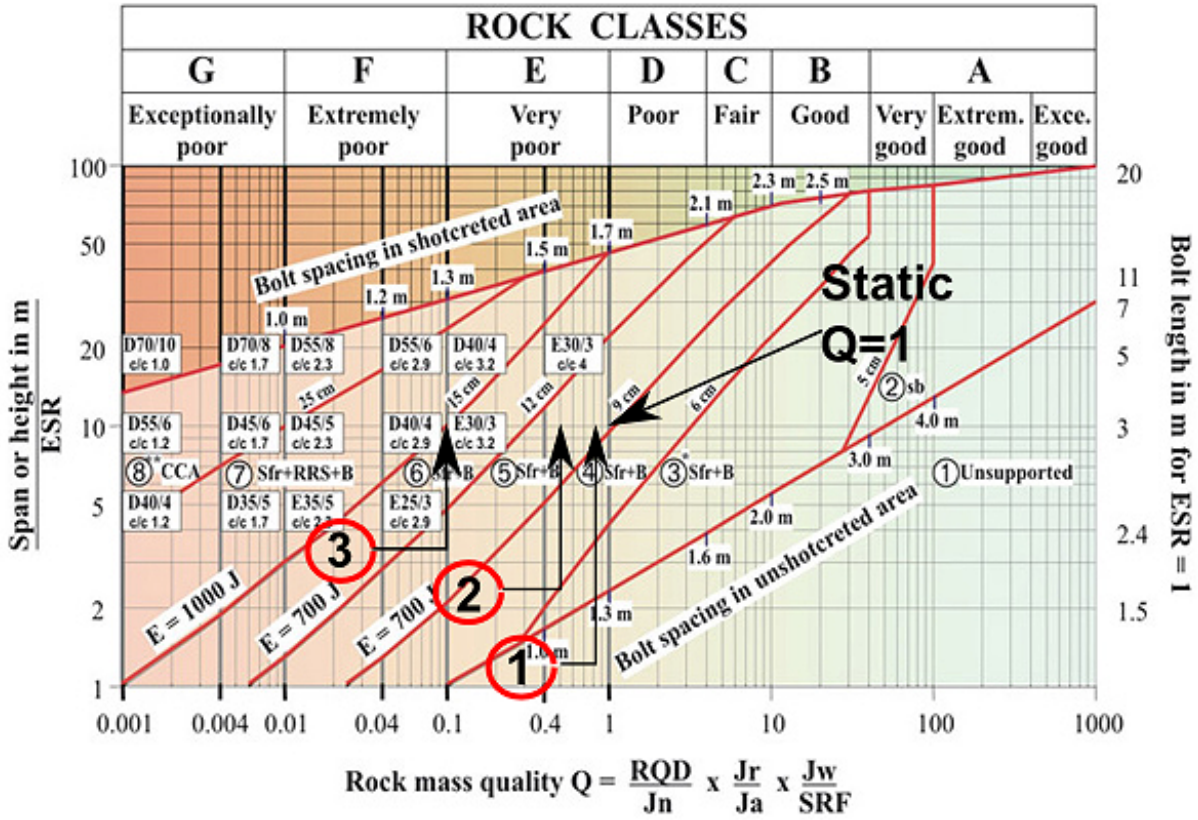

FIGURE 7.5: The location of the Points 1 to 3on the Q-system support design chart shows the new recommended support for th three cases. The static condition of a 10-m diameter tunnel in rock mass with Q=1 and assuming ESR = 1 is also shown for reference. Note that $Q_{seismic} < Q_{static}$. Points 1 and 2 are still within the same support category No. 5 as the static condition, but Point 3 jumps to the next support category (between 6 and 7) and therefore calls for a need to increase the support for this seismic loading.

7.3.2 Point 2: $K_h = 0.15; K_v = -0.075$ and α_k = 0.52

The Point no. 2, shown in Fig. 7.8, represents the α_k for a 10-m diameter circular tunnel in rock mass with Q = 1 at a depth of 60 m for seismic coefficients $K_h = 0.15; K_v = -0.075$. Using 0.7 as the reduction factor between ground motion at surface and ground motion at depth of 60 m, the surface peak ground acceleration corresponding to this seismic coefficients is $\approx 0.15/0.7 = 0.21$g.

$$\begin{aligned} K_h &= 0.15 \\ Q_{static} &= 1 \\ T_{static}(kN) &= 340.14 \\ T_{seismic}(kN) &= 424 \\ Q_{seismic}^{-1/3} &= 1.25 \\ Q_{seismic} &= 1.25^{-3} = 0.5244 \\ \alpha_k &= \frac{Q_{seismic}}{Q_{static}} = \frac{0.5244}{1} \approx 0.52 \end{aligned} \tag{7.16}$$

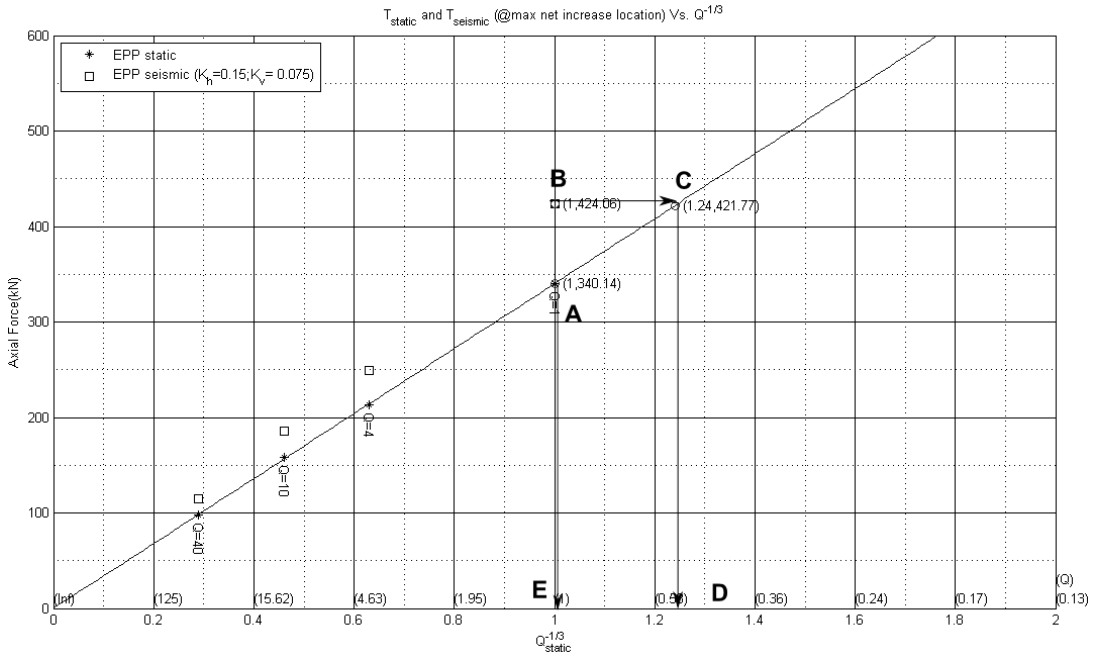

FIGURE 7.6: The axial force on the liner vs. $Q_{static}^{-1/3}$ plot for seismic coefficients $K_h = 0.15; K_v = -0.225$. The corresponding Q-values are shown in brackets along the x-axis. The significance of the coordinates of points A - E are described in the text.

The axial force vs. $Q_{static}^{-1/3}$ plot for this seismic loading is shown in Fig. 7.6. The coordinates for points A -E are same as those described for Point No. 1, where the data used in the following calculations (see Eq. 7.16) are obtained from the coordinates of these points. The $Q_{seismic}$ for these seismic loading is equal to $0.52Q_{static}$. Thus, the resulting α_k of 0.52 is very close the 0.5 coefficient adopted by Barton (1984) as shown in Eq. 7.1. This indicates that the reduction of Q by half to obtain $Q_{seismic}$ is valid for poor quality rock mass with Q=1 under seismic loading with horizontal seismic coefficient of 0.15 at tunnel depth, which is equivalent to about 0.21g PGA at the surface. The 0.21g surface PGA is roughly equal to an earthquake intensity of VIII - IX on Mercalli Scale.

Using the support pressure Eqn. 7.4, the support pressure for seismic condition for this case be expressed as:

$$P_{seismic} = 0.52^{-1/3} P_{static} = 1.24 P_{static}$$

This shows that the increase in predicted support pressure due to seismic loading is about 24%, which is almost equal to the 25% increase as recommended using Eqn. 7.2.

The seismic Q value of 0.5 for this case is plotted on the tunnel design support and labeled as Point 2 in Fig. 7.5. All both points 1 and 2 are within the same support Category No. 5, when compared with Point No. 1, Point No. 2 has shifted significantly leftward – very close to bolt spacing = 1.5 m. In order to be on the conservative side, for Point No. 2, the recommended increase in support pressure is to *decrease* the bolt spacing from 1.7 m to 1.5 m and Sfr thickness from 9 cm to $>$ 9 cm to compensate for seismic loading. However, as clearly described in previous sections, increasing the thickness of the liner negatively affects the shotcrete liner's performance during seismic shaking and therefore this equivalent increase in support pressure should be achieved through bolting, or grouting while remembering to maintain high flexibility

ratio of the liner-rock mass system.

Interestingly, the 0.21g surface PGA corresponding to the seismic coefficients ($K_h = 0.15; K_v = 0.075$) used here is just above the threshold of 0.20g set through empirical relationship between damage from shaking and surface PGA (Dowding and Rozen, 1978; Sharma and Judd, 1991; Power et al., 1998). It can be inferred that since the surface PGA used for this case is slightly higher than the empirically determined threshold between "No Damage" and "Slight Damage" (see Fig. 1.3), the need for increase in support pressure for surface PGA > 0.20 as observed here is justifiable. It should however be noted that there are inherent uncertainties in assuming a constant reduction factor of 0.7 to relate the PGA experienced at depth and surface PGA.

7.3.3 Point 3: $K_h = 0.55; K_v = -0.275$ and α_k = 0.10

As with Points 1 and 2, Point No. 3 shown in Fig. 7.8, represents the α_k for horizontal seismic coefficient equal to 0.55 at tunnel depth of 60 m. The axial force Vs. $Q_{static}^{-1/3}$ plot used to calculate the α_k from the coordinates of points A -E is shown in Fig. 7.6. Using a surface to depth reduction factor of 0.7, the horizontal seismic coefficient of 0.55 at 60 m is equivalent to ≈ 0.8g surface PGA. This is a very high intensity and is equivalent to Intensity X on Mercalli Scale and Intensity VII on Japanese Meteorological Agency (JMA) scale (see Fig. 3.5).

Using the coordinates of these points A - E, the value of $Q_{seismic} = 0.1$ for this seismic loading. The steps followed to obtain $Q_{seismic}$ are shown as the steps followed to derive Eq. 7.17.

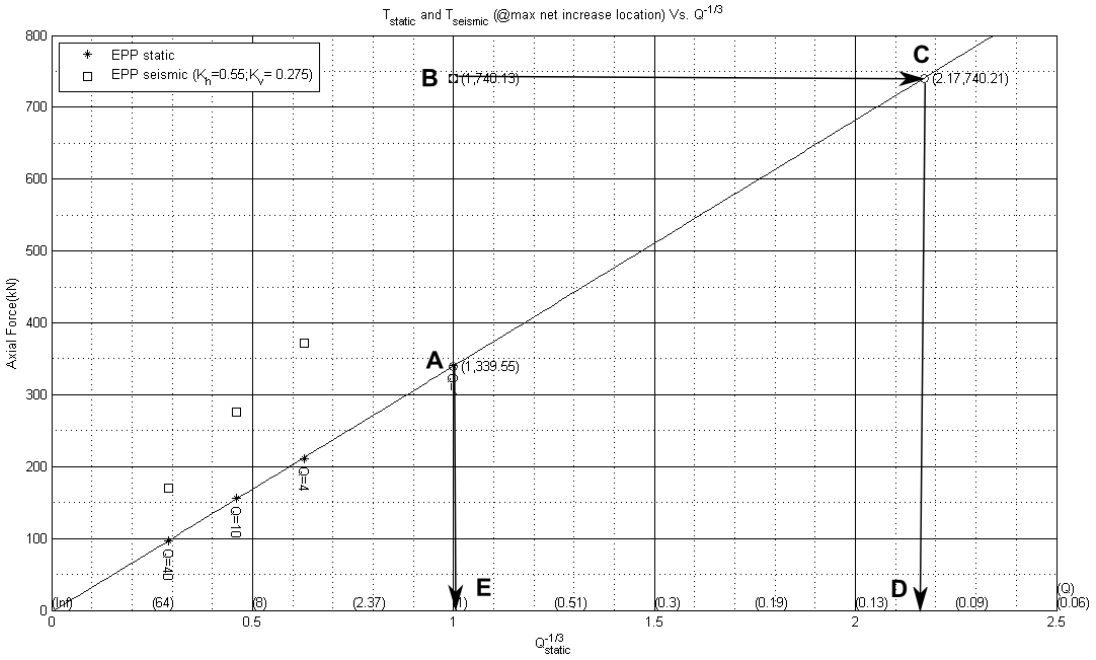

FIGURE 7.7: The axial force on the liner vs. $Q_{static}^{-1/3}$ plot for seismic coefficients $K_h = 0.55; K_v = -0.275$. The corresponding Q values are shown in brackets along the x-axis. The significance of the coordinates of points A - E are described in the text.

$$\begin{aligned} K_h &= 0.55 \\ Q_{static} &= 1 \\ T_{static}(kN) &= 339.55 \\ T_{seismic}(kN) &= 740.13 \\ Q_{seismic}^{-1/3} &= 2.17 \\ Q_{seismic} &= 2.17^{-3} = 0.0978 \\ \alpha_k &= \frac{Q_{seismic}}{Q_{static}} = \frac{0.0978}{1} \approx 0.1 \end{aligned} \tag{7.17}$$

Using the support pressure Eqn. 7.4, the seismic support pressure for Point No. 3 can be calculated as:

$$P_{seismic} = 0.1^{-1/3} P_{static} = 2.15 P_{static}$$

This shows that for seismic loading equivalent to 0.8g PGA at surface, the predicted seismic support pressure for a 10 m diameter tunnel at 60 m depth in rock mass with Q = 1 increases by about 2.15 $times$ predicted static support pressure, a 115% increase. In order to visualize this enormous increase in support pressure due to seismic loading, Point No. 3, representing $Q_{seismic} = 0.1$, is also plotted on Fig. 7.5. As expected there is a drastic increase in predicted support when compared with static condition. In order to compensate for this seismic loading on a tunnel in poor quality rock mass, it can be deduced from observations thus far that the bolt spacing should be decreased from 1.7 m to 1.3 m and the thickness of Sfr should be increased from 9 cm to 12 cm. As just as was the case for Points 1 and 2, since increasing the thickness of the Sfr results in decreasing the flexibility ratio, which is detrimental to the shotcrete liner's performance during seismic loading, the equivalent support pressure corresponding to the required increase in Sfr should be compensated through other measures, such as more bolting or grouting of the surrounding weak rock mass.

Similar computations were done for K_h from 0.05 to 0.75 and the resulting values of α_k are plotted against K_h as shown in Fig. 7.8. It can be inferred that an exponential relationship exists between α_k and K_h.

Furthermore, the influence of rock mass quality Q was investigated by calculating α_k for the different rock masses with Q = 1 - 40. The tunnel dimension and depth were kept constant. The resulting α_k for elastic and elastic-perfectly-plastic models for the four rock classes are shown in Table 7.1. It may be noted that α_k values for rock masses with $Q \geq 4$ at 60-m depth overlap as these rock masses are still within their elastic limit, they tend to behave similarly.

For poor rock mass with Q = 1, α_k decreases from 0.81 to 0.06 as K_h is increased from 0.05 to 0.70. From the second column in Table 7.1, it can be inferred that the relationship $\alpha_k = 0.5$, as recommended by Barton (1984), is valid when $K_h = 0.15$; beyond this, α_k decreases as the intensity of the earthquake loading increases.

The plots of α_k values for three models – elastic, EPP with $Q \geq 4$ and EPP with Q = 1 for the specified range of K_h are shown in Fig. 7.9. It can be inferred that this relationship

$$\alpha_k = e^{-\beta K_h}$$

exists, where β is equal to 4.3 for poor quality rock mass represented by Q = 1 (with plastic zone developed around the tunnel periphery), 3.1 for good quality rocks with Q = 4 - 40 (with no plastic zone around the tunnel), and 2.5 for elastic models.

It must be noted here that various limitations and uncertainties are inherent in this relationship obtained through numerical modeling. The viability of this equation could not be tested through numerical modeling and therefore it is recommended to verify or validate this relationship through empirical data from cases studies related to earthquake damage of tunnels. Despite these shortcomings, the approach presented here provides an alternative to seismic design of tunnels and this exponential relationship could be used as a starting point. The value of expected K_h can be obtained from the expected peak ground acceleration, which are available from seismic hazard maps.

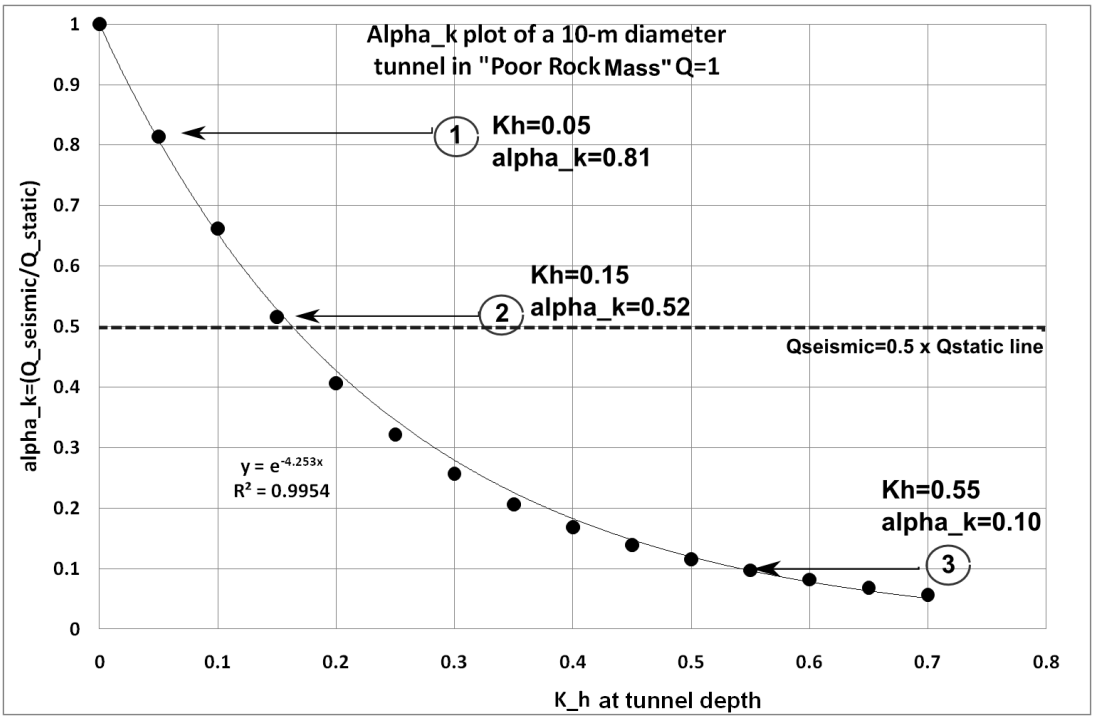

FIGURE 7.8: The α_k vs. K_h plot of a 10 m diameter tunnel at 60 m depth in rock mass with Q = 1. Although only K_h is shown here, there is an intrinsic assumption that the vertical seismic coefficient $K_v = -0.5K_h$ and therefore K_v is always applied during seismic loading. The points 1 - 3 are used in the following subsections to describe the methodology followed to obtain this curve for rock mass with Q = 1.

K_h	α_k **EPP Q=1**	α_k **EPP Q=4-40**	α_k **Elastic**
0.05	0.81	0.85	0.86
0.10	0.66	0.73	0.74
0.15	0.52	0.62	0.64
0.20	0.41	0.53	0.56
0.25	0.32	0.45	0.49
0.30	0.26	0.38	0.43
0.35	0.21	0.33	0.38
0.40	0.17	0.28	0.34
0.45	0.14	0.24	0.31
0.50	0.12	0.21	0.28
0.55	0.10	0.18	0.25
0.60	0.08	0.16	0.23
0.65	0.07	0.14	0.20
0.70	0.06	0.12	0.19

TABLE 7.1: Range of α_k for different rock mass qualities as a function of horizontal seismic coefficient K_h, shown in the first column. α_k for a 10 m diameter tunnel in rock mass with Q = 1 at 60 m depth is shown in the second column. The third column show α_k for rock masses with Q= 4 to 40 modeled as elastic-perfectly-plastic model, but that have not yielded at 60 m depth. The Fourth column show the average α_k for the elastic models for Q ranging from 1 to 40; the α_k for all the elastic models tend to overlap one another.

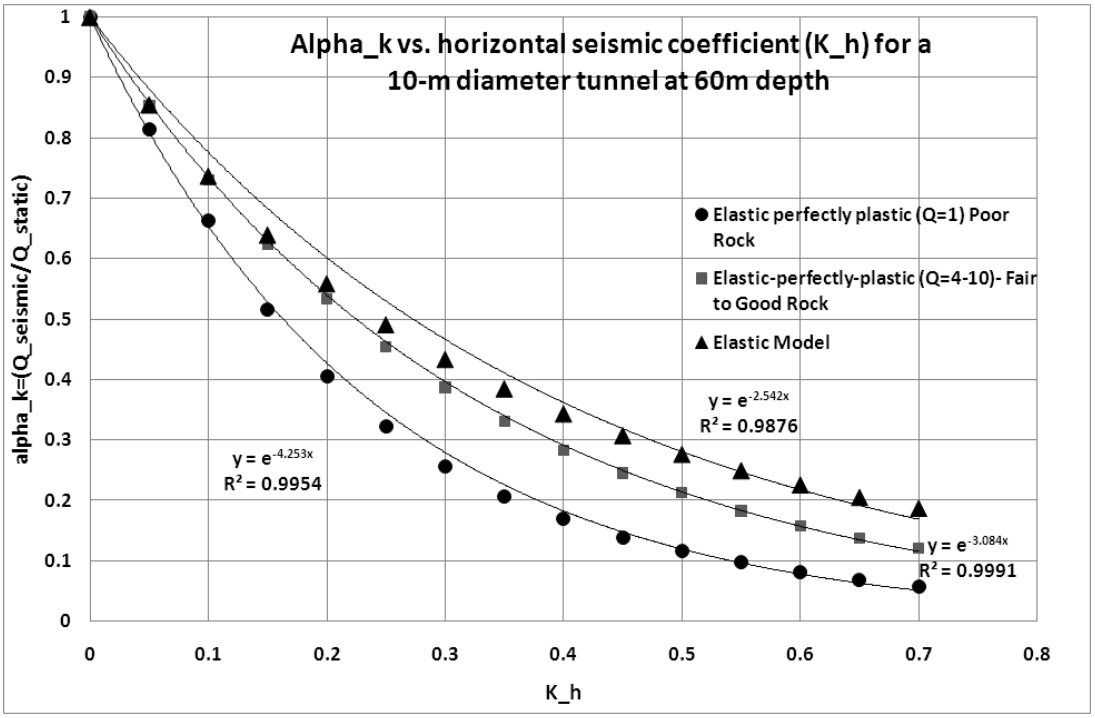

FIGURE 7.9: Plot of α_k for K_h ranging from 0.05 - 0.70 for a 10 m diameter tunnel at 60 m depth. The data used to generate this plot are shown in Table 7.1. It appears that relationship $\alpha_k = e^{-\beta K_h}$ exists where β = 4.3 for poor quality rock mass represented by Q = 1; β = 3.1 for good quality rocks with Q = 4 - 40; and β = 2.5 for elastic models. The plots were forced through the point (0,1) as $\alpha_k 01$ when $K_h = 0$, meaning that the $Q_{seismic} = Q_{static}$ when the seismic loading does not exist.

Chapter 8

Conclusions

The following are the findings from the literature review and numerical experiments conducted for this thesis:

- Although underground structures are less susceptible to damage due to earthquakes than surface structures, there have been several cases where damage due to earthquakes have been reported in tunnels (Wang et al., 2001; Kontoe et al., 2008; Li, 2011). It has been documented in previous studies (Dowding and Rozen, 1978; Power et al., 1998; Hashash et al., 2001) that the factors influencing the impact of earthquakes on tunnels are: Magnitude of earthquake, distance to epicenter, peak ground acceleration (PGA), geologic conditions including rock mass quality, overburden thickness, depth of the tunnel, age of the tunnel, and the angle of incidence of the seismic waves on the tunnel.

  The most important findings from these empirical studies are: (1) the damage due to earthquakes decreases with depth. Most of the damages reported were at < 50 m and with no serious damage beyond 300 m depth (Sharma and Judd, 1991); however, in weak rocks in Longxi tunnel, Li (2011) reported collapse of secondary concrete lining at 500 m depth. This shows that the influence of rock mass quality makes the effect of depth on earthquake damage more complicated; (2) The damage due to earthquakes can be correlated with surface peak ground acceleration, where no damage was observed when PGA is ≤ 0.2g (Dowding and Rozen, 1978; Sharma and Judd, 1991; Power et al., 1998); the upper limit beyond which severe damages were observed range from 0.5g - 0.6g; (3) Tunnels are more liable to damage during large earthquakes > 6 on Richter scale (Sharma and Judd, 1991).

- To investigate the effect of earthquakes on tunnels through numerical modeling, the quasi-static approach in Phase^2 is employed. Four rock mass classes with rock mass quality Q ranging from 1 to 40 were investigated. Owing to the high wavelength to dimension ratio (~ 20) in rock masses, the use of quasi-static seismic loading is justified as, at this scale, the dynamic interaction between the tunnel and the passing seismic waves is minimal (Dowding, 1984). Similarly, the seismic coefficient is assumed to be equal to the ratio of peak ground acceleration and acceleration due to gravity g.

  The impact of earthquakes on tunnels is simulated through three stages: (1) to simulate consolidation of the rock mass before excavation of the tunnel, (2) Static loading due

to redistribution of stresses after excavation, and (3) application of quasi-static seismic loading to Stage 2.

- Two sets of experiments were conducted using rock masses with Q ranging from 1 to 40. First the influence of rock mass quality on the required support pressure, for both static and seismic loading, was investigated using a 10-m diameter tunnel placed at 60 m depth. For both sets of experiments, the seismic loading was fixed as $K_h = 0.30; K_v = -0.15$. The rock mass quality of the surrounding rock mass was changed from Q = 1 to 40. It may however be noted that at 60-m depth, only rock mass with Q=1 has surpassed its elastic limit and therefore behaves as elastic-plastic materials. The four rock mass classes were assumed to behave as elastic-perfectly-plastic materials after failure. Therefore, both elastic-perfectly-plastic and elastic models were investigated.

  As a function of rock mass quality, the maximum seismic axial force, which is the difference between axial force for seismic loading and static loading, increases with decreasing rock mass quality. For 10-m diameter tunnel at 60 m depth, the % increase in seismic axial force at the point of maximum increase (usually either the shoulder or the knee of the tunnel) is about 37% for rock mass with $Q \geq 4$ (and 57% for rock mass with Q = 1 using elastic-perfectly-plastic model. For elastic model, the increase is 32% for all rock classes.

- The second set of experiment was designed to study the influence tunnel diameter on the required support pressure was conducted where the diameter of the tunnel was increased from 5 to 20 m with 5 m interval. Two rock masses with Q = 1 and Q = 40 were analyzed for all tunnel dimensions to simulate poor and good rock qualities, respectively.

  For poor quality rocks, represented by Q = 1 using elastic-perfectly-model, the axial force on the lining (both absolute magnitude and increase due to seismic loading) increases with increasing tunnel dimension. The maximum positive increase in axial force due to seismic loading with seismic coefficients is 56% (157 kN) for 5 m diameter tunnel and 71% (289 kN) for 20 m diameter tunnel. On the other hand, for good quality rocks, represented by Q = 40 using elastic-perfectly-plastic models, the increase in axial force as function of tunnel dimension is relatively insignificant, i.e. 33% (30.6 kN) for 5 m diameter and 35% (37 kN) for 20 m diameter tunnel.

- Using information derived from the parametric studies as discussed above, it is attempted to determine the predicted seismic support pressure for different rock mass quality Q. The approach presented here is based on the concept of $Q_{seismic}$, which was introduced by Barton (1984). During earthquake loading, it can physically be inferred that the predicted rock support pressure should be larger than for static conditions. The increase in support pressure during seismic loading can be envisaged as the effect of the reduction in rock mass quality from Q_{static} to $Q_{seismic}$. The new support system can be obtained from the existing Q-system tunnel design chart (see Fig. 2.3 on page 17) using $Q_{seismic}$ instead of Q_{static}. As a rule of thumb, Barton (1984) recommended reducing the Q value by half such that

$$Q_{seismic} = 0.5 Q_{static}$$

It is however proposed here that

$$Q_{seismic} = \alpha_k Q_{static}$$

where α_k is a coefficient that is dominantly dependent on the horizontal seismic coefficient and rock mass quality Q. Nonetheless, it can be postulated that α_k also depends on other properties of the rock mass, dimension of the tunnel, and properties of the shotcrete liner.

It was demonstrated in this thesis that α_k can be computed by ratio of the axial force on the lining for static condition T_{static} to the axial force for seismic condition $T_{seismic}$. For a particular seismic loading on a given model,

$$\alpha_k = \frac{Q_{seismic}}{Q_{static}} = \left(\frac{T_{static}}{T_{seismic}} \right)^3$$

For rock mass with Q = 1, α_k decreases from 0.81 to 0.06 as K_h increases from 0.05 to 0.70 (see Table 7.1 on page 98). As a function of horizontal seismic coefficient K_h and rock mass quality, α_k for a 10-m diameter tunnel at 60-m depth in different rock masses can be expressed as

$$\alpha_k = e^{-\beta K_h}$$

where β = 4.3 for poor quality rock mass represented by Q = 1 (with plastic zone developed around the tunnel periphery), β = 3.1 for good quality rocks with Q = 4 - 40 (with no plastic zone around the tunnel), and β = 2.5 for elastic models. It may be noted that K_h used here is equal to the PGA at tunnel depth for tunnels in rock masses. The relationship between K_h and PGA could be different for tunnels in materials other than the rock mass classes studied in this thesis. This mainly depends on the possibility of any dynamic interaction between the tunnel and the passing seismic waves.

- It must be noted that there are limitations and uncertainties inherent in obtaining the α_k (see Table 7.1) through numerical modeling. Mainly for the sake of simplicity during modeling, several assumptions underlie the method presented here. These assumptions are:(1) quasi-static seismic loading assumption, (2) the assumption that rock masses behave as elastic-perfectly-plastic materials after failure, (3) hydrostatic stress condition with $\gamma = 0.027$ MN/m3, (4) continuum rock mass around the tunnel, (5) elastic liner, among others. In addition, the viability of the α_k values presented here has not been tested and validated, even through numerical modeling. Despite these limitations, the α_k values for different K_h either in table form or as equation can be used as a starting point for seismic design of tunnels. Although, the depth of the tunnel was kept constant at 60 m, this can be a representative depth as the effect of earthquakes are higher at shallower depth and as most of the tunnels are located at an average depth of around 100 m.

  The recommendations for future research in this field, after considering the limitations and uncertainties encountered in this approach, are presented in the next chapter.

Chapter 9

Recommendations

The following are the lessons learned and recommendations for future research this field.

- **Direct correlation between Strength parameters and Q:** The Mohr-Coulomb parameters used to simulate different rock mass quality Q in this thesis were first obtained for Rock Mass Rating (Bieniawski, 1979). Then, based on rock mass classes, different Q values were assigned by Waltham (2009). It could be more accurate if direct relationship between Q and Mohr-Coulomb parameters are established through analysis of case studies where in-situ strength tests and Q values are available.

- **Post-failure characteristics:** As shown in Fig. 4.5, an approximate conversion between rock mass quality Q and Geological Strength Index (GSI) implies that all four rock classes studied in this thesis could exhibit *strain-softening* post-failure characteristics. However, as strain-softening model requires at least an additional parameter, all four rock classes were assumed to behave as elastic-perfectly-plastic, which is usually reasonable for very poor rocks (Hoek and Brown, 1997). It might be more realistic to model the rock masses studied here as strain-softening materials.

- **Discontinuum Vs. Continuum Model:** Here, the rock masses are treated as "continuum" with average properties relating to different rock mass quality Q. However, as suggested by Dowding (1979), rock masses can vary substantially on tunnel-scale and must be modeled as "discontinuum". Soil masses, on the contrary, can be treated as continuum on tunnel scale. Therefore, it is recommended to compare the results obtained here assuming continuum rock masses with outcome from other numerical modeling programs that model the rock mass as a discontinuum.

  Furthermore, the effect of introduction of joints or discontinuities into the model could also be investigated. It has been founded that in jointed rocks, the joints or discontinuities tend to "accentuate" the impact of seismic waves, thereby directing the failure at the intersection of the liner and the joints (Abokhalil, 2007; Bhasin et al., 2006,0).

- **Shotcrete liner properties:** It was assumed in this study that the shotcrete liner is elastic with constant properties. However, in reality, the properties of the shotcrete change, for instance, due to hardening of the shotcrete with aging. The liner properties for such studies could be staged such that the properties of the shotcrete liner in Stage 3 is different

(stronger) from Stage 2. The influence of liner properties on numerical modeling results is discussed in detail in Hammah et al. (2006).

- **Installation of Shotcrete Liner:** It was assumed that the shotcrete liner is installed *immediately* after excavation of the tunnel. Due to practical limitations during construction, there is always some delay between excavation and installation of shotcrete liner. This delay (if not waited until the tunnel collapses) has some positive effect, as some stress will have released through relaxation before the support is installed. This effect is discussed in detail in analytical methods, such as in Carranza-Torres and Fairhurst (2000) and AFTES (2001), and should be considered during future studies. Options in Phase2 are to use "load-splitting" or "material-softening" methods described in the Phase^2 tutorials from www.rocscience.com.

  In addition, it was assumed here that the liner is perfectly attached to the rock mass. In reality, there could be some gap between the shotcrete liner and the rock mass. During numerical modeling in Phase^2, it seems possible to model gaps between the rock mass and the liner using, for e.g. "composite" liner. The influence of such gaps that exists between the shotcrete liner and rock mass should be investigated as the rock mass-liner interaction plays a vital role in determining the impact of earthquakes on tunnels.

- **Influence of dimension and depth of the tunnel:** The influence of depth on the impact of earthquakes on tunnels is expected to be complicated. For a particular rock mass, the plastic zone around the tunnel increases with increasing depth. The effect of earthquake on a tunnel depends on the extent of the failed zone around the tunnel (Barton, 1984). On the contrary, the intensity of the ground motion decreases with depth and therefore the impact at depth is generally lower than near surface (Barton, 1984; Sharma and Judd, 1991). Therefore, it will be interesting to investigate the influence of depth on the impact of earthquakes on tunnels and therefore α_k.

  For a fixed seismic loading, it was demonstrated that the impact of earthquake loading increases with increasing tunnel dimension. Thus, the influence of tunnel dimension on α_k must be investigated through numerical modeling.

  It might be interesting to explore the influence of the depth and dimension of the tunnel as a function of their ratio as discussed in Cilingir and Madabhushi (2011b).

- **Inertial Force Vs. Displacement based method:** In this study, inertial force based pseudo-static seismic loading was employed. The other method is displacement-based. In this method, the displacement at the tunnel depth is calculated, mainly through 1D dynamic analysis. The resulting strain, usually as function of depth, is imposed onto the tunnel, and the stresses and strains on liner are computed. It is recommended to investigate the impact of earthquakes on tunnels in rock masses using both methods to check the applicability of these two methods.

  A quantitative comparison of pseudo-static analysis, dynamic analysis, and observed damages could provide greater insights into this area of research.

References

Abokhalil, M. (2007). Insights into the response of rock tunnels to seismicity. Master's thesis, University of Oslo.

AFTES (2001). Recommendations on the convergence-confinement method, report no. GT7R6A1. *www.aftes.asso.fr*.

Alejano, L., Rodriguez-Dono, A., Alonso, E., and Fdez.-Manín, G. (2009). Ground reaction curves for tunnels excavated in different quality rock masses showing several types of post-failure behaviour. *Tunnelling and Underground Space Technology*, 24(6):689 – 705.

Aversa, S., Barla, G., Rampello, S., and Simonelli, A. (2009). Innovative procedures for design of retaining structures and evaluation of slope stability. In Manfredi, G.and Dolce, M., editor, *The state of Earthquake Engineering Research in Italy: the ReLUIS-DPC 2005-2008 Project*, pages 223–270.

Aydan, O., Ohta, Y., Genis, M., Tokashiki, N., and Ohkubo, K. (2010). Response and stability of underground structures in rock mass during earthquakes. *Rock Mechanics and Rock Engineering*, 43:857–875. 10.1007/s00603-010-0105-6.

Baker, R., Shukha, R., Operstein, V., and Frydman, S. (2006). Stability charts for pseudo-static slope stability analysis. *Soil Dynamics and Earthquake Engineering*, 26(9):813 – 823.

Barton, N. (1984). Effect of rock mass deformation on tunnel performance in seismic regions. *Advances in Tunnelling Technology and Subsurface Use*, 4(3):89–99.

Barton, N. (2002). Some new Q-value correlations to assist in site characterisation and tunnel design. *International Journal of Rock Mechanics and Mining Sciences*, 39(2):185 – 216.

Barton, N. (2004). Failure around tunnels and boreholes and other problems in rock mechanics. *ISRM News Journal*, 8(2):12–18.

Barton, N., Lien, R., and Lunde, J. (1974). Engineering classification of rock masses for the design of tunnel support. *Rock Mechanics*, 6(4):189–236.

Basarir, H., Genis, M., and Ozarslan, A. (2010). The analysis of radial displacements occurring near the face of a circular opening in weak rock mass. *International Journal of Rock Mechanics and Mining Sciences*, 47(5):771 – 783.

Bhasin, R. (2011). Personal communication.

Bhasin, R., Abokhalil, M., Kaynia, A., Høeg, K., Paul, D., and Pal, S. (2010). Numerical simulations of earthquake effect in underground structures. *14th Symposium on Earthquake Engineering, Indian Institute of Technology, Roorkee*, pages 1384–1394.

Bhasin, R. and Grimstad, E. (1996). The use of stress-strength relationships in the assessment of tunnel stability. *Tunnelling and Underground Space Technology*, 11(1):93–98.

Bhasin, R., Magnussen, A., and Grimstad, E. (2006). Effect of tunnel size on stability problems in rock masses. *Tunnelling and Underground Space Technology*, 21(3-4):405.

Bhatia, S., Kumar, M., and Gupta, H. (1999). A probabilistic seismic hazard map of india and adjoining regions. *Annali Di Geophysica*, 42(6):1153–1164.

Bieniawski, Z. (1974). Geomechanics classification of rock masses and its application in tunneling. In *Advances in Rock Mechanics - Reports of Current Research. Proccedings of the third congress of International Society of Rock Mechanics*, volume II, pages 7–34.

Bieniawski, Z. (1979). The geomechanics classification in rock engineering applications. In *ISRM Proceedings of the Fourth International Congress for Rock Mechanics, Montreux, Switzerland*, volume 2, pages 41–48. Balkema, Rotterdam.

Bilotta, E., Lanzano, G., Russo, G., Santucci de Magistris, F., Aiello, V., Conte, E., F., S., and Valentino, M. (2007). Pseudostatic and dynamic analyses of tunnels in transversal and longitudinal direction. In *4th International Conference on Earthquake Geotechnical Engineering, Thessaloniki, Greece 2007*.

Carranza-Torres, C. and Fairhurst, C. (2000). Application of the convergence-confinement method of tunnel design to rock masses that satisfy the Hoek-Brown failure criterion. *Tunnelling and Underground Space Technology*, 15(2):187–213.

Cilingir, U. and Madabhushi, S. G. (2011a). A model study on the effects of input motion on the seismic behaviour of tunnels. *Soil Dynamics and Earthquake Engineering*, 31(3):452 – 462.

Cilingir, U. and Madabhushi, S. P. G. (2011b). Effect of depth on seismic response of circular tunnels. *CANADIAN GEOTECHNICAL JOURNAL*, 48(1):117–127.

Corkum, B. (2011). Email communication.

Dowding, C. (1979). Earthquake stability of rock tunnels. *Tunnels and Tunnelling*, pages 15–20.

Dowding, C. (1984). Estimating earthquake damage from explosion testing of full-scale tunnels. *Advanced Tunnel Technology and Subsurface Use*, 4(3):113–117.

Dowding, C. and Rozen, A. (1978). Damage to rock tunnel from earthquake shaking. *Journal of Geotechnial Engineering ASCE*, 104:175–191.

Egger, P. (2000). Design and construction aspects of deep tunnels (with particular emphasis on strain softening rocks). *Tunnelling and Underground Space Technology*, 15(4):403 – 408.

FHWA (2009). *Technical Manual for Design and Construction of Road Tunnels - Civil Elements*. U.S. Department of Transportation Federal Highway Administration. Jeremy , C.H. and Monsees, J. and Munfah, N. and Wisniewski, J.

Goel, R., Jethwa, J., and Dhar, B. (1996). Effect of tunnel size on support pressure. *International Journal of Rock Mechanics and Mining Sciences & Geomechanics Abstracts*, 33(7):749–755.

Gokceoglu, C., Sonmez, H., and Kayabasi, A. (2003). Predicting the deformation moduli of rock masses. *International Journal of Rock Mechanics and Mining Sciences*, 40:701–710.

Grimstad, E., Bhasin, R., Hagen, A., Kaynia, A., and Kankes, K. (2003). Q-system advance for sprayed lining. *Tunnelling and Tunnelling International*.

Guan, Z., Jiang, Y., Tanabasi, Y., and Huang, H. (2007). Reinforcement mechanics of passive bolts in conventional tunnelling. *International Journal of Rock Mechanics and Mining Sciences*, 44(4):625 – 636.

Hammah, R., Yacoub, T., and Curran, J. (2006). The Influence of Youngs Modulus on Numerical Modelling Results, Report No. ARMA/USRMS 06-995. In *The 41st Symposium on Rock Mechanics (USRMS): "50 Years of Rock Mechanics – Landmarks and Future Challenges*.

Hashash, Y. M. A., Hook, J. J., Schmidt, B., and Yao, J. I.-C. (2001). Seismic design and analysis of underground structures. *Tunnelling and Underground Space Technology*, 16(4):247 – 293.

Hoek, E. and Brown, E. (1997). Practical estimates of rock mass strength. *International Journal of Rock Mechanics and Mining Sciences*, 34(8):1165–1186.

Hoek, E. and Diederichs, M. (2006). Empirical estimation of rock mass modulus. *International Journal of Rock Mechanics and Mining Sciences*, 43(2):203 – 215.

Hoek, E. and Marinos, P. (2007). A brief history of the development of the Hoek-Brown failure criterion. *Soils and Rocks*, (2):13.

Jiang, Y., Wang, C., and Zhao, X. (2010). Damage assessment of tunnels caused by the 2004 Mid Niigata Prefecture Earthquake using Hayashis quantification theory type II. *Natural Hazards*, 53:425–441. 10.1007/s11069-009-9441-9.

Kaynia, A. (2011). Personal communication.

Kontoe, S., Zdravkovic, L., Potts, D. M., and Menkiti, C. O. (2008). Case study on seismic tunnel response. *Canadian Geotechnical Journal*, 45(12):1743–1764.

Lanzano, G., Bilotta, E., and Russo, G. (2008). Tunnels under seismic loading: a review of damage case histories and protection methods. *Final conference - Earthquake engineering presentation of the book "Strategies for reduction of the seismic risk"*, PPT slides.

Li, T. (2011). Damage to mountain tunnels related to the wenchuan earthquake and some suggestions for aseismic tunnel construction. *Bulletin of Engineering Geology and the Environment*, pages 1–12. 10.1007/s10064-011-0367-6.

Luo, X., Murono, Y., and Nishimura, A. (2002). Verifying adequacy of the seismic deformation method by using real examples of earthquake damage. *Soil Dynamics and Earthquake Engineering*, 22:17–28.

Mohammadi, H. and Rahmannejad, R. (2010). The estimation of rock mass deformation modulus using regression and artificial neural networks analysis. *The Arabian Journal for Science and Engineering*, 35(1A):205–217.

Nedderman, R. M. (1992). *Statics and Kinematics of Granular Materials*. Cambridge University Press.

NGI (1997). ENGINEERING GEOLOGY – Practical application of the Q-method. Technical Report 592046-4, Norwegian Geotechnical Institute, Sognsveien 72, N-0806 Oslo.

Nye, T. and Kitson, M. (2009). Shallow cover tunnel under heritage listed brick buildings: Brisbane boggo road busway tunnel. Rocscience News. http://www.rocscience.com/about/news/article/49. Accessed February 2011.

Oreste, P. (2009). The convergence-confinement method: Roles and limits in modern geomechanical tunnel design. *American Journal of Applied Sciences*, 6(4):757–771.

Palmstrom, A. (2005). Measurement of and correlation between block size and rock quality designation (RQD). *Tunnelling and Underground Space Technology*, 20:362–377.

Palmstrom, A. and Singh, R. (2001). The deformation modulus of rock mass – comparisons between in situ tests and indirect estimates. *Tunnelling and Underground Space Technology*, 16(3):115 – 131.

Potts, D. and Zdravkovic, L. (1999). *Finite element analysis in geotechnical engineering - theory*. Thomas Telford.

Power, M., Rosidi, D., and Kaneshiro, J. (1998). Seismic vulnerability of tunnels and underground structures revisited. In Ozdemir, L, editor, *NORTH AMERICAN TUNNELING '98*, pages 243–250. North American Tunneling 98 Conference on New Horizons - Building our Future, NEWPORT BEACH, CA, FEB 21-25, 1998.

Rocscience Inc. (2001). *Phase2 Program reference Manual.*

Rocscience, Inc. (2002). Developer's tip: Pseudo-static loading. https:download.rocscience.com/library/rocnews/fall2002/DeveloperTip.pdf.

Rocscience, Inc. (2011). Phase2 - finite element analysis for excavations and slopes. http://www.rocscience.com.

Sharma, S. and Judd, W. R. (1991). Underground opening damage from earthquakes. *Engineering Geology*, 30(3-4):263 – 276.

Singh, B. and Goel, R. (2006). *Tunnelling in weak rocks*. Elsevier geo-engineering book series. Elsevier Ltd, United Kingdom, first edition.

Srbulov, M. (2008). *Geotechnical Earthquake Engineering - Simplified Analyses with Case Studies and Examples*, volume 9 of *Geotechnical, Geological and Earthquake Engineering*. Springer.

St John, C. and Zahrah, T. (1987). Aseismic design of underground structures. *Tunnelling and Underground Space Technology*, 2(2):165 – 197.

Stein, S. and Wysession, M. (2003). *An Introduction to Seismology, Earthquakes, and Earth Structure*. Blackwell Publishing, Oxford, UK.

Towhata, I. (2008). *Geotechnical Earthquake Engineering*. Springer-Verlag Berlin Heidelberg.

Waltham, T. (2009). *Foundations of Engineering Geology*. Taylor and Francis, third edition.

Wang, W. L., Wang, T. T., Su, J. J., Lin, C. H., Seng, C. R., and Huang, T. H. (2001). Assessment of damage in mountain tunnels due to the Taiwan Chi-Chi Earthquake. *Tunnelling and Underground Space Technology*, 16(3):133 – 150.

Wang, Z., Gao, B., Jiang, Y., and Yuan, S. (2009). Investigation and assessment on mountain tunnels and geotechnical damage after the wenchuan earthquake. *Science in China Series E: Technological Sciences*, 52:546–558. 10.1007/s11431-009-0054-z.

Appendix A

External Boundary of the Model

The Phase^2 program has three options to automatically generate the external boundary. The three options are Box, Circle, and Hull, which are generated using the specified expansion factor. Since this study is aimed toward studying the effect of other parameters, such as rock mass quality, depth, and seismic coefficient, the external boundary is always kept constant for numerical experiments designed to vary some other parameter. This is achieved by specifying the same "user-defined" external boundary for all the experiments in a particular set.

The distance of the external boundary from the tunnel and the boundary conditions imposed along the external boundary are crucial to constructing a geomechanical model that represents the problem, which is in our case a tunnel excavated at some specified depth surrounded by a rock mass with a particular rock mass quality Q. Owing to this importance, the selection of external boundaries – both in terms of extent and the boundary conditions imposed on it are discussed in detail in the following sections.

A.1 Boundary Conditions

It is a common practice in Phase^2 to specify a boundary condition using displacement restraints. Thus, four types of restraints are possible, namely vertical roller (X restrain, Y free), horizontal roller (Y restrain, X free), Pinned (X and Y restrain), and free (both X and Y are free).

The top boundary of the model, which represents the ground surface, is always modeled as a free surface, indicating a stress-free boundary. However, the following four cases (see Fig. A.1) are possible by assigning different restraints to the other three sides of the model. As shown in Case 1 in the figure, the four sides of the external boundary are marked 1 through 4 in clockwise direction.

- Case 1: All four boundaries have pinned restraints.
- Case 2: The ground surface (1), or the top boundary of the model, is free and the other three borders are pinned.
- Case 3: The ground surface (1) is free, the bottom (3) is pinned, and the two sides (2 and 4) have vertical rollers.

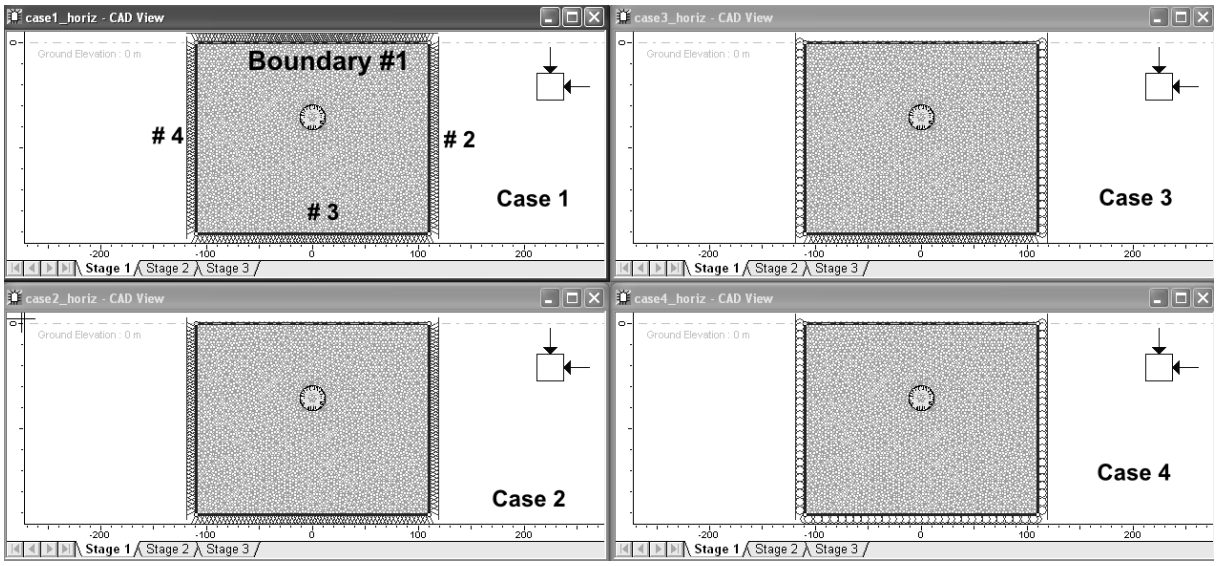

FIGURE A.1: Models of four cases of different displacement boundary conditions as described the list.

- Case 4: The ground surface (1) is free, the bottom (3) has horizontal rollers, and the two sides (2 and 4) have vertical rollers.

In order to compare the effect of different boundary conditions imposed on the model, the material properties and loading (both initial stress and seismic coefficient) were kept same for all the four cases. For all four cases, the model consists of a 20-m diameter tunnel in rock mass with Q=1 at 60-m depth. The gravity static loading, which applies a static load equal to the weight of the overburden at hydrostatic condition is chosen and the seismic coefficients chosen for the seismic loading are $K_h = 0.5; K_v = 0$. The result of static and seismic loading are shown in Figure A.2 and A.2, respectively.

It can be observed that the Maximum Axial Force on the Lining (MAFL) for all four cases are in the same range, in the first decimal place (i.e. around 0.4200 MN). Furthermore, the shape of the total displacement contours are also similar except for Case 1, where the fixed boundary condition on the ground surface forces the zero total displacement downward to the tunnel. Since the ground surface is always stress-free, pinned boundary condition cannot be used for this boundary and, therefore, *Case 1 is considered infeasible*. Similarly, Case 4 may not also be appropriate as having a roller along the bottom boundary would cause the whole model to move when seismic loading is applied.

The 'o' and 'x' marks in Fig. A.3 show yielded elements where 'o' shows tension and 'x' represents shear failure. A large zone of tension failure can be seen to the upper right hand corner of all the models. This can be attributed to the effect of boundary condition when a horizontal seismic loading is applied. At the boundary, the material, when pulled away by applied seismic force, creates a large tensile stress due to the applied boundary conditions and this effect can be minimized by increasing the extent of the external boundary, or by placing an elastic material away from the tunnel (Corkum, 2011). When the sign of the horizontal seismic coefficient is reversed, this tension zone appears on the opposite corner, and the tension zone disappears when *only* vertical seismic loading is applied, thereby confirming that this tension zone at the corners is an artifacts of the boundary conditions imposed on the model, especially for seismic loading(see Fig. A.4).

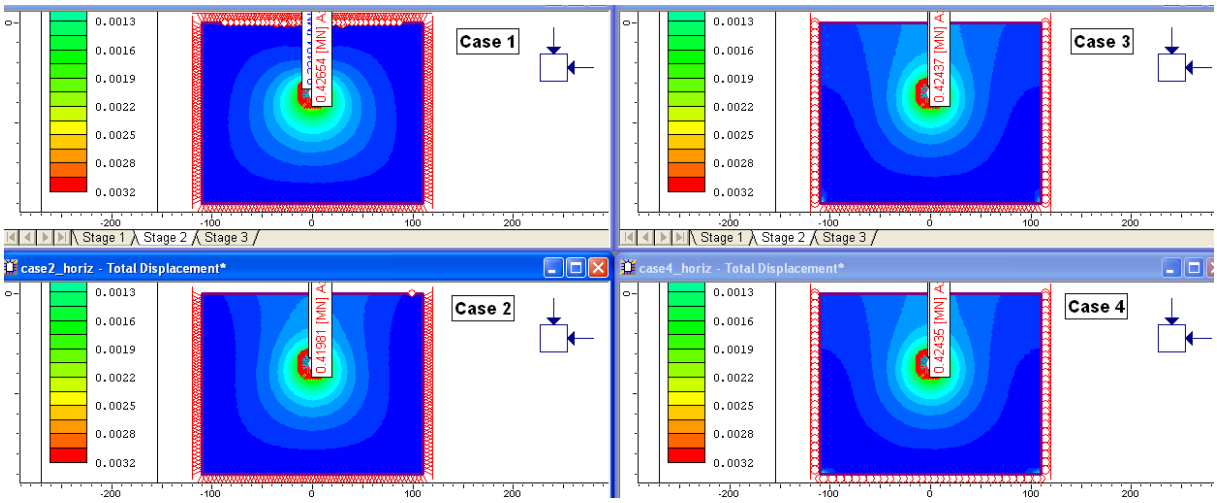

FIGURE A.2: Total displacement contour plots for the models with four boundary conditions after static loading.

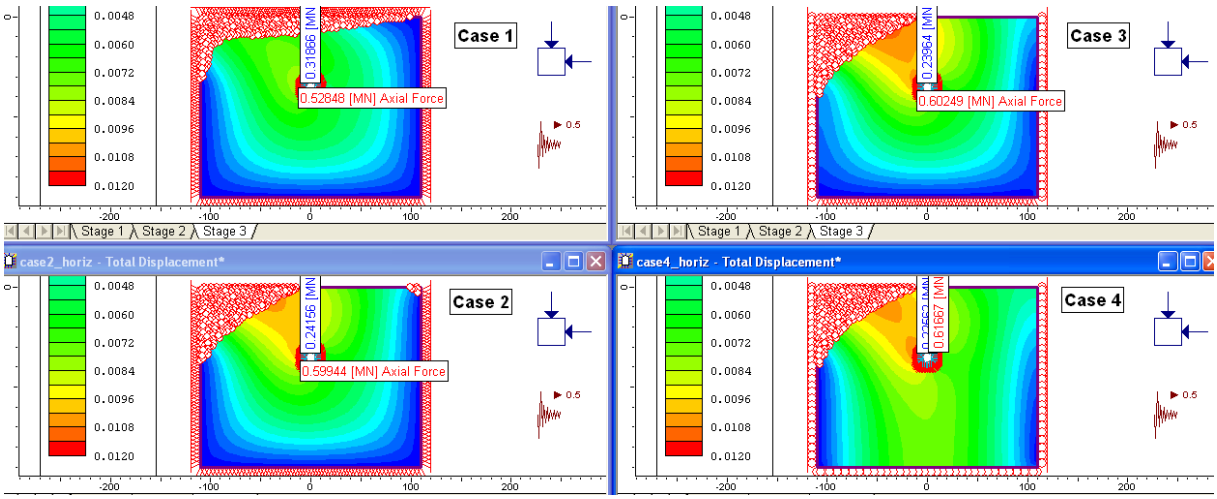

FIGURE A.3: Total displacement contour plots for the models with four boundary conditions after seismic loading.

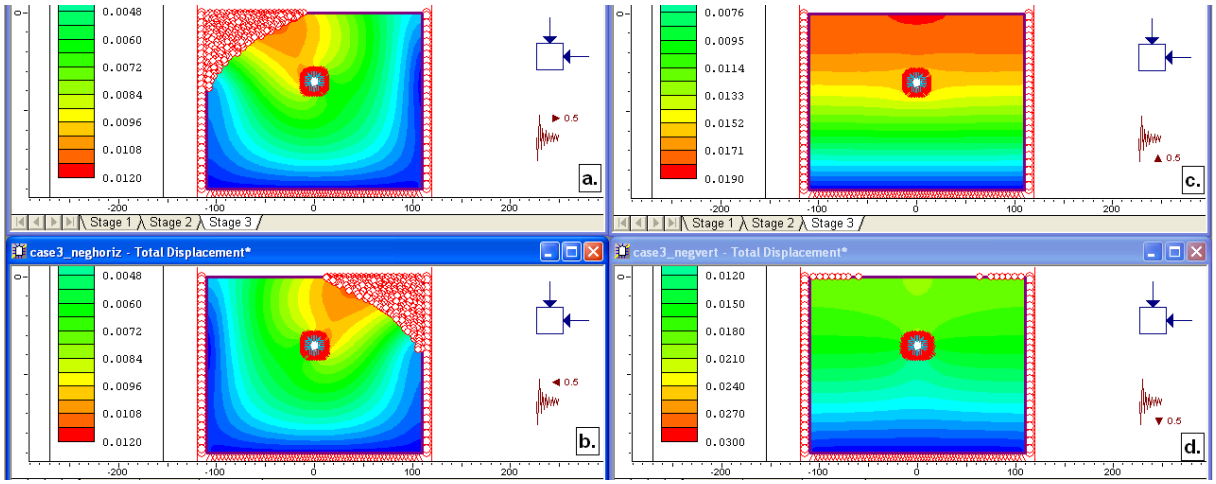

FIGURE A.4: Total displacement contour plots for Case 3 model with different seismic loading: a) h=0.5, v=0; b) h=-0.5, v=0; c) h=0, v=0.5; d) h=0, v=-0.5, where *h* is the horizontal seismic coefficient and *v* is the vertical seismic coefficient.

From Cases 2 and 3, the latter was chosen to be more appropriate as fixing the two side-boundaries would result in a rigid model. Besides, the MAFL for Case 3 is larger than Case 2, thereby producing a more conservative model in order to avoid overlooking the impact of seismic loading. On the other hand, in Case 3, the vertical side boundaries have rollers, which implies that there can be no shear force on this boundary and the nodes are therefore free to move in vertical direction. This conforms with the boundary conditions specified for a similar problem in Kontoe et al. (2008); Potts and Zdravkovic (1999), page 47; and several cases studies (for e.g. Nye and Kitson (2009)) reported by Rocscience Inc. Furthermore, the zone of tension failure at the corners, discussed above as an artifact of the external boundary condition imposed on the model, is also least for Case 3 than any other external boundary conditions specified above. Therefore, Case 3, with a stress-free surface on the top, pinned boundary at the bottom, and vertical rollers at the vertical sides of the model, is used as the boundary condition for all the numerical experiments for this study.

A.2 Dimension of the model

The dimension of the model, or the distance from the tunnel to the external boundary, should be chosen such that the constraints applied on the external boundaries do not affect the zone of interest, around the tunnel periphery in this case. The effect of the two boundary condition types – vertical rollers (fixed X) along the vertical sides of the model and fixed (X and Y) at the bottom boundary – will be investigated by increasing the distance from the tunnel to the external boundary from 3 to 10 times the tunnel diameter D. During this test, the depth and diameter of the tunnel, rock mass quality Q, and loading are kept constant, which is same as the ones used in Section A.1. Since 20-m diameter is the largest dimension that will be used in this study, this analysis to investigate the external boundary uses 20-m diameter tunnel as a representative model.

The total displacement contour plot for four models with their external boundary placed at a distance of 3 - 8 times the diameter of the tunnel is shown in Figure A.5. In addition, as the boundary conditions are specified in terms of displacement constraints, the variation of displacement from the tunnel to the external boundaries are investigated to see the effect of external boundaries on the zone of interest around the tunnel. Two lines are chosen as shown in Fig. A.5. The magnitude of the total displacement along Line 1 is plotted as a function of distance away from the tunnel until the external boundary (see Fig. A.6(a)). This is because "fixed" boundary condition with fixed X and fixed Y is specified at the bottom boundary condition and the total displacement should be zero at the bottom external boundary. The aim is to investigate at which distance from the tunnel the total displacement can be considered equal to zero and how it affects the measurement around the tunnel.

On the other hand, the same procedure is applied along Line 2, but the magnitude of horizontal displacement is used instead as the boundary condition specified at boundary no. 2 is Fixed X and Free Y and this the horizontal displacement should become zero at the vertical side boundaries No. 2 and 4. Nonetheless, only the effect along line 2, toward boundary no. 2, is studied (see Fig. A.6(b)) as the behavior is expected to be equivalent toward boundary no. 4.

The optimum extent of the external boundary should be chosen such that no further sig-

nificant change in displacement occurs when the external boundary is increased beyond that distance. By observing Figure A.6, it can be concluded that the model with 8D is the optimum model as the increase in displacement between 8D and 10D is insignificant. Thus, the extent of the external boundary is chosen as $\geq 8D$, which means that the distance of the external boundary from the tunnel should be at least 4 times the tunnel dimension. However, it should be noted that the distance between ground surface and the tunnel in this study is always equal to the specified depth, even when it is less than 8D.

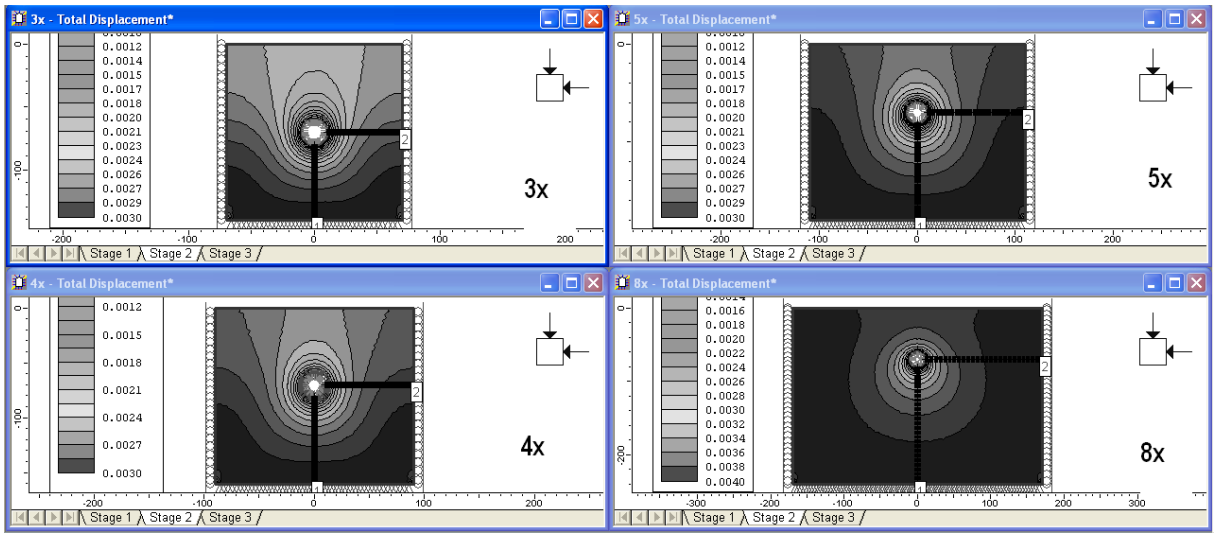

FIGURE A.5: Total displacement contour plot for models with different external boundary extent varying from 3 - 8 times the diameter of the tunnel. Lines of Query 1 and Query 2 described in the text are also shown here.

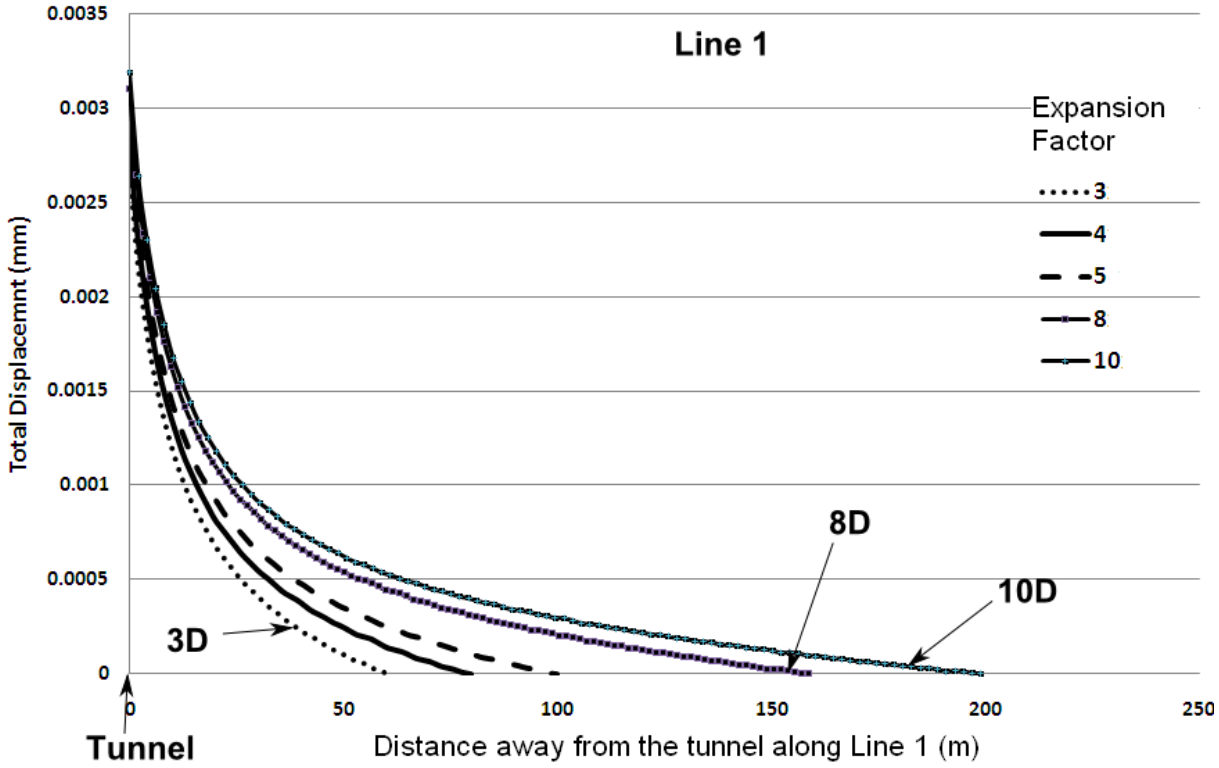

(a) Total displacement (mm) along Line 1

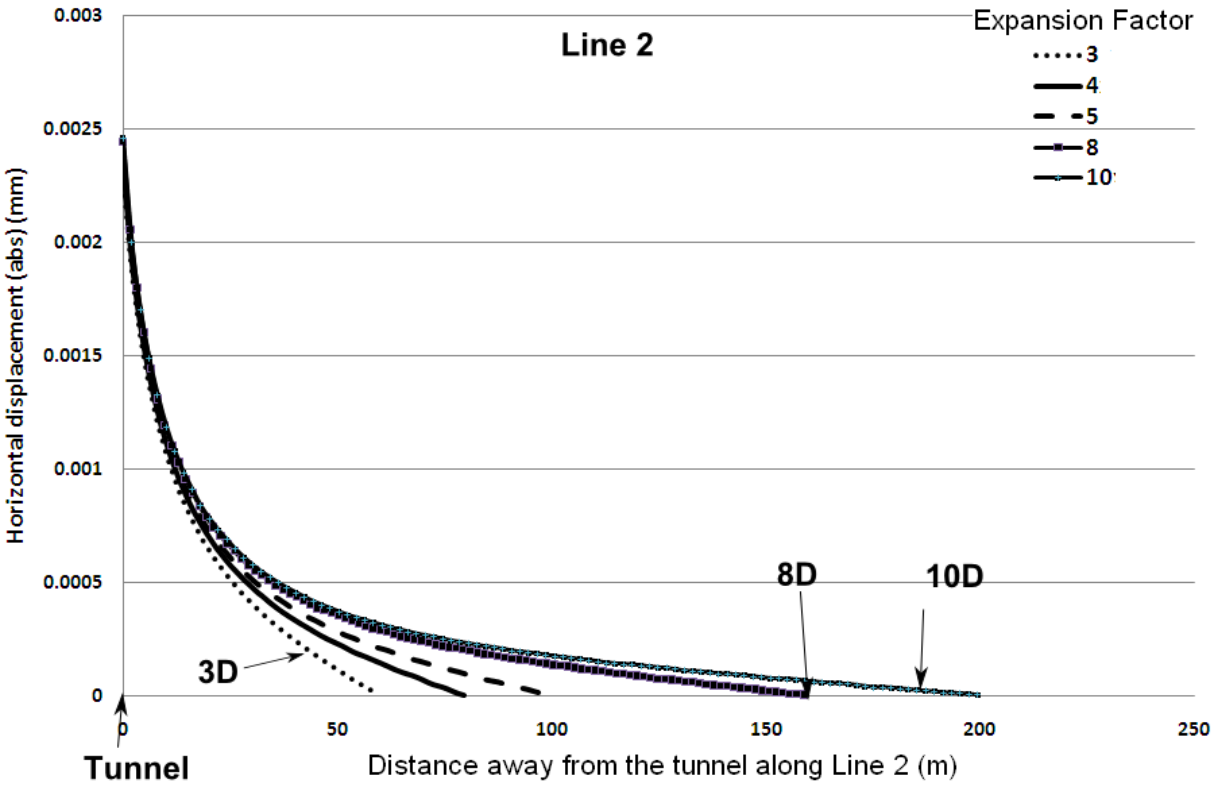

(b) Horizontal displacement (mm) along Line 2

FIGURE A.6: Displacement plot as function of distance away from the tunnel periphery for lines 1 and 2 as shown in Fig. A.5. The total displacement is plotted in Fig. A.6(a) and horizontal displacement is plotted in Fig. A.6(b). From these two figures, it can be inferred that model with external boundary at $\geq$ 8D is optimum as increasing the external boundary from 8D to 10D did not result in any significant change in the displacement field of interest.